Subleading Corrections to High Energy Jets for W Plus Jets Production

JAMES BLACK

How to cite:

BLACK, JAMES (2025) Subleading Corrections to High Energy Jets for W Plus Jets Production. Doctoral thesis, Durham University.

Subleading Corrections to High Energy Jets for W Plus Jets Production

James Airon Black

A Thesis presented for the degree of
Doctor of Philosophy

Institute for Particle Physics Phenomenology
Department of Physics
Durham University
United Kingdom

September 2025

Subleading Corrections to High Energy Jets for *W* Plus Jets Production

James Airon Black

Submitted for the degree of Doctor of Philosophy

September 2025

Abstract: We define the next-to-leading logarithmic corrections to the High Energy Jets (HEJ) formalism for W plus jets production. We provide in depth analytical derivation of these subleading corrections, as well as thorough verification of their validity. This is to improve traditional fixed-order calculations that struggle to provide reliable predictions in the high energy limit due to the emergence of these large logarithmic corrections.

Also contained within are various technical details of enhancements to HEJ that have enabled the transition from Version 1 to Version 2 and thus improvements to future predictions.

Through comparisons with experimental data from ATLAS at 7 TeV and 8 TeV collisions, we demonstrate significant improvements in our theoretical predictions, particularly in the cross-section at large transverse momenta, highlighting the enhanced predictive power of the improved HEJ framework. The refinements presented here not only strengthen our understanding of QCD in the high-energy limit but also provide a valuable tool for future experimental analyses at the LHC and beyond.

CONTENTS

Abstract **iii**

List of Figures **ix**

List of Tables **xix**

1 Introduction to Quantum Chromodynamics **1**

1.1 Context and Background 1

1.2 QCD Lagrangian 6

1.2.1 Quark Content 7

1.2.2 The Consequences of Gauged Actions 8

1.2.3 The Θ Term and the Strong CP Problem 12

1.3 From Feynman rules to Cross-Sections 13

1.3.1 Regularising UV Divergences in QFT 19

1.3.2 IR Divergences and Dimensional Regularisation 21

1.3.3 PDFs and Factorisation 23

1.4 Further Improvements 27

2 High Energy Jets **33**

2.1 Framing Discussions 34

2.2 The High Energy Limit 37

2.2.1 Regge Theory and the MRK Limit 40

2.3 HEJ Framework 41
2.3.1 Motivation for HEJ 42
2.3.2 HEJ Amplitudes 47
2.3.3 Real Emission Corrections 50
2.3.4 Matching 56
2.4 W+Jets in HEJ 58
2.5 Implementation within `HEJ2` 61

3 Monte Carlo Simulations 65
3.1 What is a Monte Carlo Generator 66
3.1.1 First Example 66
3.1.2 The Error of Our Ways 67
3.1.3 Random Number Generation 69
3.1.4 Sampling 71
3.2 Phase-Space Generation in HEJ 73
3.2.1 Changes needed for HEJ2 73
3.2.2 Generation of Resummation Phase-Space Points 76
3.2.3 Number of emissions 78
3.2.4 Treatment of gluons outside jets 79
3.2.5 Treatment of gluons inside jets 79

4 Subleading Channels 83
4.1 Motivation 83
4.2 Next-To-Leading-Logs 86
4.3 Unordered Contributions 88
4.4 Extremal $q\bar{q}$ Contributions 91
4.5 Calculation of Central $q\bar{q}$ Contributions 93
4.5.1 W-Boson Emission from the External Quark Lines 95
4.5.2 W-boson Emission from the Central Quark Line 97
4.5.3 Choosing the W-boson Emission Site 106

4.6 Matrix Element Validation: HEJ_Explorer 108
4.6.1 Explorer Plot of Unordered Processes 109
4.6.2 Explorer Plot of Extremal $q\bar{q}$ Processes 111
4.6.3 Crossing Correspondence 113
4.6.4 Central $q\bar{q}$ (Extremal W Emission) Explorer Plots 114
4.6.5 Central $q\bar{q}$ (Central W Emission) Explorer Plots 120
4.6.6 Further verifications 125

5 Results 127
5.1 Numerical Impact of NLL Components 127
5.2 ATLAS Predictions 135

6 Conclusions 141

Bibliography 145

LIST OF FIGURES

1.1 A visualisation of the size and placement of the proposed Future Circular Collider. Image from CERN website. 2
1.2 This is the Standard Model of Particle Physics 4
1.3 Feynman diagrams representing the increasing contributions in FO contributions at increasing orders. 17
1.4 A real gluonic emission becoming unresolved in both the soft and collinear limits 21
1.5 The CT18NLO PDF set presented at two energy scales. Note that the gluon curve has been reduced by a factor of 5. Plot taken from [1] 24
1.6 The standard figure [2] which shows how the hard scattering process (red) relates to all other parts of scatterings; parton shower (blue), hadronization (light green), hadron decays (dark green), underlying event (violet) and QED radiation (yellow) which occur for typical proton-proton collisions at Hadron Colliders such as the LHC. . . 26

2.1 Feynman diagrams for two-to-two gluon scattering process, illustrating the s-channel (a), t-channel (b), and u-channel (c) contributions . . 39
2.2 A Schematic representation of an example $2 \to n$ gluon scattering amplitude in the MRK limit 41

2.3 The leading-order matrix element squared multiplied by a phase-space factor and a factor of $\frac{C_F}{C_A}$ for each of the quarks in the final state is shown for of various different scattering processes. These matrix elements are plotted against a parameter Δ, which is half of the rapidity separation between the extremal partons in the final state. The MRK limit is shown as a flat line on all plots, and it is seen as the rapidity span is opened, this limit is reached by the fixed-order matrix elements. Plots reproduced from [3] 43

2.4 The average number of jets in inclusive W plus dijet production from Tevatron at a centre-of-mass energy $\sqrt{s} = 1.96$ TeV as a function of the rapidity separation between two hardest jets, $\Delta y(j_1, j_2)$ (left), and rapidity separation between the most forward and backward jets, $\Delta y(j_f, j_b))$ (right). [4] 44

2.5 Differential cross-section with respect to the invariant mass between the two hardest jets, Δm_{12} in inclusive W plus dijet production at the ATLAS detector with a center-of-mass energy of $\sqrt{s} = 7$ TeV Plot reproduced from [5] 45

2.6 This Figure illustrates how the Lipatov Vertex contains within it contributions from all possible gluon emission sites. 53

2.7 This is an example FKL Amplitude. Notice in particular the rapidity ordering with the quarks at the extremal limits. 56

2.8 The possible W-Emissions from the external lines with an effective vertex 60

2.9 Differential cross-section with respect to the scalar sum of transverse momentum, H_T at $\sqrt{s} = 7$ TeV. Figure reproduced from Ref. [6]. A significant discrepancy is observed between `HEJ` and `ATLAS` data for large H_T. 63

2.10 Planar representations of the two different possible 3j subleading contributions. Notably, when in a planar representation it is impossible to draw a planar diagram with the corresponding external legs and the same strict rapidity ordering without the use of a t-channel propagator. 64

3.1 This illustrates the idea of a Monte Carlo integration. By taking the ratio of points which lie within the circle it is possible to work out the area of the circle. 68
3.2 This graph depicts the spectral test performed on a Linear Congruential Random Number Generator 70
3.3 A depiction of importance sampling. A function $f(x)$ is to be integrated, but we sample points for the Monte Carlo integration in a probabilistic fashion from the distribution $p(x)$. 73
3.4 $\overline{n}_g$ as a function of the rapidity gap between extremal jets. 77

4.1 The leading-order $W+3-jet$ [left plot] and $W+4-jet$ cross-sections [right plot] as a function of the invariant mass between the most forward and backward jets, m_{fb}. In addition to the total (black), we also show the split into the contributions from the LL configurations (blue), NLL configurations (green) and other configurations (red). As m_{fb} increases, the LL configurations increase in dominance but the NLL configurations remain significant 84
4.2 The leading-order $W+3-jet$ [left plot] and $W+4-jet$ [right plot] cross-sections as a function of the transverse momentum of the hardest jet, $p_{\perp,1}$. In addition to the total (black), we also show the split into the contributions from the LL configurations (blue), NLL configurations (green) and other configurations (red). As $p_{\perp,1}$ increases, the LL configurations decrease in importance underlining the importance of also applying resummation to the NLL contributions. 86

4.3 These plots show that replacing one t-channel gluon in a FKL configuration introduces suppression by a factor of $s_{j_1 j_2}$. $|\bar{M_1}|^2$ (red) corresponds to the Full FKL contribution, $qQ \to qgHQ$, whereas $|\bar{M_2}|^2$ (blue) and $|\bar{M_3}|^2$ (green) correspond to unordered emissions with a t-channel quark propagator, $qQ \to gqHQ$ and $qQ \to gHqQ$ respectively. The FKL contribution tends to a constant as the rapidity separation increases, while the non-FKL configurations are suppressed by a factor of $s_{j_1 j_2}$ as demonstrated in the right plot. SOURCE: [7] . 88

4.4 A Depiction of the effective current or the unordered impact factor with a W emission in the effective vertex 89

4.5 These are the $q\bar{q}$ contributions to the NLL. 90

4.6 A Depiction of the effective current or the $q\bar{q}$ impact factor with a W emission in the effective vertex 91

4.7 These are the Pure Jet Extremal $q\bar{q}$ contributions. The trick we have to play here is to include all of the possible W-boson emissions to these diagrams to include the analogous W+Jets NLL processes to HEJ 92

4.8 These are the Pure Jet Central $q\bar{q}$ contributions. The trick we have to play here is to include all the possible W-boson emissions to these diagrams to include the analogous W+Jets NLL processes to HEJ . 94

4.9 The possible W-Emissions from the external lines with an effective vertex 95

4.10 The helicity of the central qqx line 97

4.11 This is the effective vertex in the central $q\bar{q}$ with a W-boson emission from the effective vertex. 98

4.12 The two possible $q\bar{q}$ current W-boson Emissions. 99

4.13 These are the possible emission sites for the W-boson when emitted from this central $q\bar{q}$ arrangement. 101

4.14 These are the possible emission sites for the W-boson when emitted from this central $q\bar{q}$ arrangement. 104

4.15 In this case of W Emission we will have possible interference. This will (at least to begin) be assumed negligible. 107

4.16 A comparison of `HEJ` and the leading-order Matrix Elements produced by `MadGraph5` for an unordered gluon configuration as denoted by the phase-space slice described in Eq. (4.6.1). Specifically, the plot demonstrates that the matrix element demonstrates the expected scaling behaviour and also that the `HEJ` prediction is in good agreement across the whole range of rapidities plotted. 111

4.17 A comparison of `HEJ` and the leading-order Matrix Elements produced by `MadGraph5` for an extremal $q\bar{q}$ configuration as denoted by the phase-space slice described in Eq. (4.6.1). Specifically this plot shows that the matrix element demonstrates the expected scaling behaviour and also that the `HEJ` prediction is in good agreement across the whole range of rapidities plotted. 112

4.18 Explorer plots for the Central $q\bar{q}$ process with the emission of a W^+-boson from an Extremal leg. Included in this figure are event types with incoming quarks and/or anti-quarks. On the left we have the `HEJ` and `MadGraph` squared Matrix elements plotted against increasing rapidity. On the right, we have the same plot by with the squared Matrix elements multiplied by the factor $\hat{s}_{q\bar{q}}$, demonstrating the expected scaling behaviour. In each plot, the bottom pane shows the ratio of the two predictions, which trends to unity for large rapidity spans. 116

4.19 Explorer plots for the Central $q\bar{q}$ process with the emission of a W^+-boson from an Extremal leg. Included in this figure are event types which include incoming gluons. On the left we have the `HEJ` and `MadGraph` squared Matrix elements plotted against increasing rapidity. On the right, we have the same plot by with the squared Matrix elements multiplied by the factor $\hat{s}_{q\bar{q}}$, demonstrating the expected scaling behaviour. In each plot, the bottom pane shows the ratio of the two predictions, which trends to unity for large rapidity spans. . 117

4.20 Explorer plots for the Central $q\bar{q}$ process with the emission of a W^--boson from an Extremal leg. Included in this figure are event types with incoming quarks and/or anti-quarks. On the left we have the `HEJ` and `MadGraph` squared Matrix elements plotted against increasing rapidity. On the right, we have the same plot by with the squared Matrix elements multiplied by the factor $\hat{s}_{q\bar{q}}$, demonstrating the expected scaling behaviour. In each plot, the bottom pane shows the ratio of the two predictions, which trends to unity for large rapidity spans. 118

4.21 Explorer plots for the Central $q\bar{q}$ process with the emission of a W^--boson from an Extremal leg. Included in this figure are event types which include incoming gluons. On the left we have the `HEJ` and `MadGraph` squared Matrix elements plotted against increasing rapidity. On the right, we have the same plot by with the squared Matrix elements multiplied by the factor $\hat{s}_{q\bar{q}}$, demonstrating the expected scaling behaviour. In each plot, the bottom pane shows the ratio of the two predictions, which trends to unity for large rapidity spans. . 119

4.22 Explorer plots for the Central $q\bar{q}$ process with the emission of a W^+-boson from the Central $q\bar{q}$ effective vertex. Included in this figure are processes with incoming quarks and/or anti-quarks. On the left we have the `HEJ` and `MadGraph` squared Matrix elements plotted against increasing rapidity. On the right, we have the same plot by with the squared Matrix elements multiplied by the factor $\hat{s}_{q\bar{q}}$, demonstrating the expected scaling behaviour. In each plot, the bottom pane shows the ratio of the two predictions, which trends to unity for large rapidity spans. 121

4.23 Explorer plots for the Central $q\bar{q}$ process with the emission of a W^+-boson from the Central $q\bar{q}$ effective vertex. Included in this figure are processes with incoming gluons. On the left we have the `HEJ` and `MadGraph` squared Matrix elements plotted against increasing rapidity. On the right, we have the same plot by with the squared Matrix elements multiplied by the factor $\hat{s}_{q\bar{q}}$, demonstrating the expected scaling behaviour. In each plot, the bottom pane shows the ratio of the two predictions, which trends to unity for large rapidity spans. . 122

4.24 Explorer plots for the Central $q\bar{q}$ process with the emission of a W^--boson from the Central $q\bar{q}$ effective vertex. Included in this figure are processes with incoming quarks and/or anti-quarks. On the left we have the `HEJ` and `MadGraph` squared Matrix elements plotted against increasing rapidity. On the right, we have the same plot by with the squared Matrix elements multiplied by the factor $\hat{s}_{q\bar{q}}$, demonstrating the expected scaling behaviour. In each plot, the bottom pane shows the ratio of the two predictions, which trends to unity for large rapidity spans. 123

4.25 Explorer plots for the Central $q\bar{q}$ process with the emission of a W^--boson from the Central $q\bar{q}$ effective vertex. Included in this figure are processes with incoming gluons. On the left we have the `HEJ` and `MadGraph` squared Matrix elements plotted against increasing rapidity. On the right, we have the same plot by with the squared Matrix elements multiplied by the factor $\hat{s}_{q\bar{q}}$, demonstrating the expected scaling behaviour. In each plot, the bottom pane shows the ratio of the two predictions, which trends to unity for large rapidity spans. . 124

5.1 Inclusive Njets cross-sections for $pp \to (W \to l\nu) + \geq N_{jets}$ where , in the top left resummation is applied only to LL states. In the top-right resummation is applied to all LL and NLL states. Also shown in each case is the breakdown into the component where all-order resummation is applied (red, dashed) and the component which remains described at fixed- order only (blue, dashed). The final subplot, which shows the relative difference between these two scenarios. 129

5.2 The differential distribution (black, solid) in the rapidity difference between the most-forward and most-backward jets, $\Delta y_{j_f,j_b}$, in $pp \to (W \to l\nu) + \geq 3j$, without and with resummation applied to NLL states. The panels and lines are as in Fig. 5.1 130

5.3 The differential distribution (black, solid) in the invariant mass of the two leading jets in $pp \to (W \to l\nu) \geq 2j$, without and with resummation applied to NLL states. The panels and lines are as in Fig. 5.1 131

5.4 The differential distribution (black, solid) in the transverse momentum of the leading jet in $pp \to (W \to l\nu) \geq 2j$, without and with resummation applied to NLL states. The panels and lines are as in Fig. 5.1 132

5.5 The differential distribution (black, solid) in the transverse momentum of the leading jet in $pp \to (W \to l\nu)+ \geq 3j$, without and with resummation applied to NLL states. The panels and lines are as in Fig. 5.1 133

5.6 The differential distribution (black, solid) in the transverse momentum of the leading jet in $pp \to (W \to l\nu)+ \geq 4j$, without and with resummation applied to NLL states. The panels and lines are as in Fig. 5.1 134

5.7 Predictions for $pp \to (W \to l\nu)+ \geq 2j$ for LHC@7TeV, compared to ATLAS data from [8]. The original HEJ1 predictions are shown in blue, the pure NLO predictions are shown in red and the new HEJ2 predictions incorporating the methods of Chapter 4 and the NLO matching from [9] are shown in green. 137

5.8 Predictions for $pp \to (W \to l\nu)+ \geq 2j$ for LHC@8TeV, compared to ATLAS data from [10]. The original HEJ1 predictions are shown in blue, the pure NLO predictions are shown in red and the new HEJ2 predictions incorporating the methods of Chapter 4 and the NLO matching from [9] are shown in green. 139

LIST OF TABLES

1.1 Timeline of Fundamental Particle Discoveries 3

1.2 QCD Feynman rules: External and internal lines [11] 30

1.3 QCD Feynman rules: Vertices [11] 31

1.4 Some W-boson Feynman rules [12]. Note there are other interactions which are possible within the Electroweak sector, but none which are useful for the discussions contained within this text 32

4.1 A summary of the particle configurations which enter the LL and NLL lines in Fig. 4.1 and Fig. 4.2. All particles except for the W are listed in rapidity order. q, Q etc. may refer to quarks or anti-quarks. Each process refers to itself and its symmetric counterpart, i.e. $qg \to Wq'gg$ is shorthand for $qg \to Wq'gg + gq \to Wggq'$. All other subprocesses not listed above are included in the line labelled 'Other'. 85

5.1 Selection cuts for the data analyses 135

DECLARATION

The work in this thesis is based on research carried out at the Institute of Particle Physics Phenomenology in the Department of Physics at Durham University. The work in this thesis has been carried out in collaboration with Jeppe R. Andersen and Jennifer M. Smillie. No part of this thesis has been submitted elsewhere for any degree or qualification and it is all my own work, unless otherwise stated.

ACKNOWLEDGEMENTS

This thesis represents the culmination of an academic journey enabled by the efforts of many. I am deeply grateful to my parents, Carole and David, whose love and support has always been foundational. To my wife, Rachel, thank you for your constant companionship, encouragement, and unwavering belief that propelled me forward.

The impact of the Covid-19 pandemic was profound, and I am exceptionally thankful for my siblings, Terry and Kaylie, and their spouses, Emily and Graham, whose support was indispensable during those tough times.

I extend my appreciation to my housemates and office mates, Jonny Cullen, Joey Reiness, and Giuseppe De Laurentis, whose camaraderie and insightful discussions greatly enriched my PhD experience at the IPPP.

Jeppe Andersen has gone above and beyond what could be expected of a supervisor, and provided unmatched guidance, patience, and understanding from my Master's project through to completion of this thesis. It was a pleasure collaborating with Jenni Smillie, whose encouragement was always uplifting. Andreas Maier's advice on software development practices throughout our time in Durham significantly influenced not only this thesis but my subsequent career.

All models are wrong, but some are useful.

— George Box

CHAPTER

ONE

INTRODUCTION TO QUANTUM CHROMODYNAMICS

In this section, we present an overview of Particle Physics and some prerequisite concepts to full understanding of the work contained in later chapters. Specifically, we will introduce *The Standard Model* (SM) of Particle Physics, the rich historical context of this theory, and ongoing efforts to test it, such as the experiments at the *Large Hadron Collider* (LHC). We will then take a deep dive into one sector of this theory, *Quantum Chromodynamics* (QCD), and a basic look at how improvements to theoretical predictions are being made.

1.1 Context and Background

The particle physics community is currently in a bit of a quandary. Our best theory of how the Universe fits together, The Standard Model, works too well. That is, it has been tested to an inordinate degree and as yet we see no deviation between its predictions and our current reach in experiments. For example, the experimental measurement of the anomalous magnetic dipole moment agrees with the SM to 10 significant figures [13].

Indeed, it has become very clear that any deviation from the SM in collider experiments will require very precise prediction of dynamics. Despite this, the SM is an

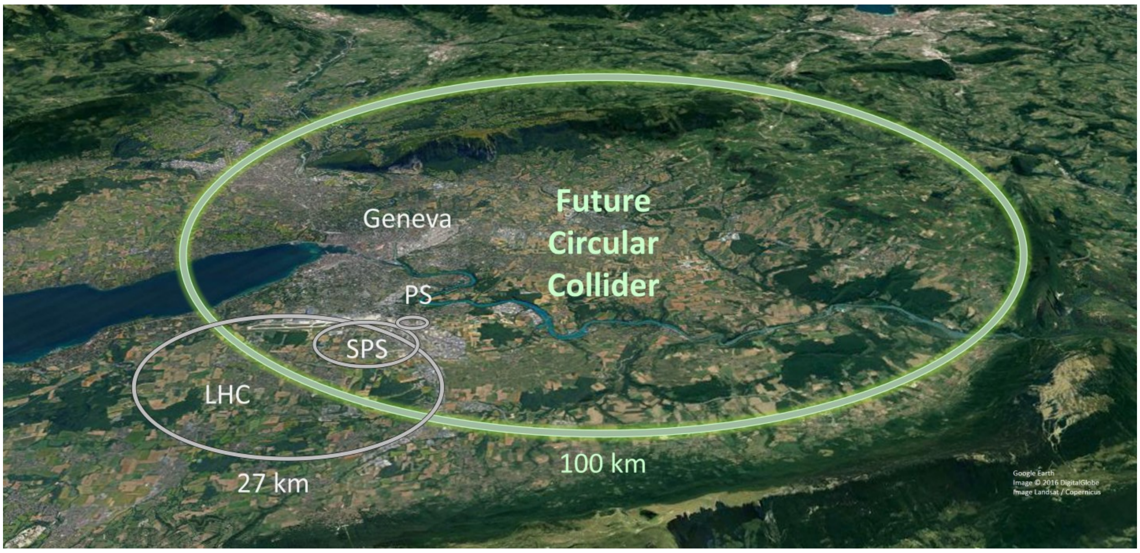

Figure 1.1: *A visualisation of the size and placement of the proposed Future Circular Collider. Image from CERN website.*

incomplete theory. It contains no description of gravity, and does not provide any insight into Dark Matter or Dark Energy, which according to some measurements make up to 96% of the mass of the universe [14]. Even the best models that try to evade the concept of dark matter by describing phenomena such as velocity curves of galaxies with *Modified Newtonian Dynamics* (MOND) simply fall short trying to describe observations such as those made in the bullet cluster [15].

It is bittersweet then, as each successive fundamental particle is discovered, and is subsequently shown to exhibit the behaviours expected of it as predicted by the SM. Table 1.1 contains a timeline of all fundamental particle discoveries and we see that it stretches from the discovery of the Electron by J. J. Thomson [16] in 1897 all the way up to 2012 with the discovery of the Higgs boson by the CMS [17] and ATLAS [18] collaborations, the final and central piece in the SM. With this latest discovery, there is physical evidence and confirmation of *Electroweak Symmetry Breaking* (EWSB), as proposed by Peter Higgs [19], Robert Brout and François Englert [20] via the *Higgs Mechanism.*

A scrupulous reader may notice a couple of trends in this time-line. Over a century of experimentation and observation, the number of collaborators for each of the experimental discoveries has ballooned from one professor to multiple collaborations.

1897	Electron.	J. J. Thomson [16]
1932	Positron.	C. D. Anderson [21] Proposed by P. Dirac (1928) [22]
1937	Muon.	S. Neddermeyer et al. [23]
1956	Electron Neutrino.	F .Reines et al. [24] Proposed by W. Pauli (1930) [25]
1962	Muon Neutrino.	L. M. Lederman et al. [26]
1969	‘Partons’ (u,d and s quarks).	J. Friedman et al. (*SLAC*) [27] Proposed by M. Gell-Mann (1964) [28]
1974	J/Ψ Charm Quark.	B. Richter et al. [29] Proposed by B. Bjørken (1964) [30]
1975	Tau.	M. L. Perl et al. [31]
1977	Υ Meson Bottom Quark.	(*Fermilab*) [32] Proposed by M. Kobayashi (1973) [33]
1979	Gluon.	D. P. Barber (*DESY*) [34]
1983	W+Z Bosons.	(*CERN*) [35]
1999	Top Quark.	(*Fermilab*) [36]
2000	Tau Neutrino.	(*Fermilab*) [37]
2012	Higgs Boson.	(*CERN*) [18] Proposed by P. Higgs (1964) [19]

Table 1.1: *Timeline of Fundamental Particle Discoveries*

The size and expense of each experiment have exponentially grown, with each iteration of a similar experiment operating at much higher energies. The LHC has collisions with a centre-of-mass energy limit of 14 TeV, which is seven times that of the previous hadron-hadron collider at Fermilab. This trend is set to continue with the proposed 100 TeV *Future Circular Collider* (FCC) which can be seen in Fig. 1.1. This is all in an effort in experimental physics to find where the SM's theoretical description breaks down.

The current state of affairs in theoretical particle physics is one of incremental progress, with the hope that this progress may help uncover some discrepancies

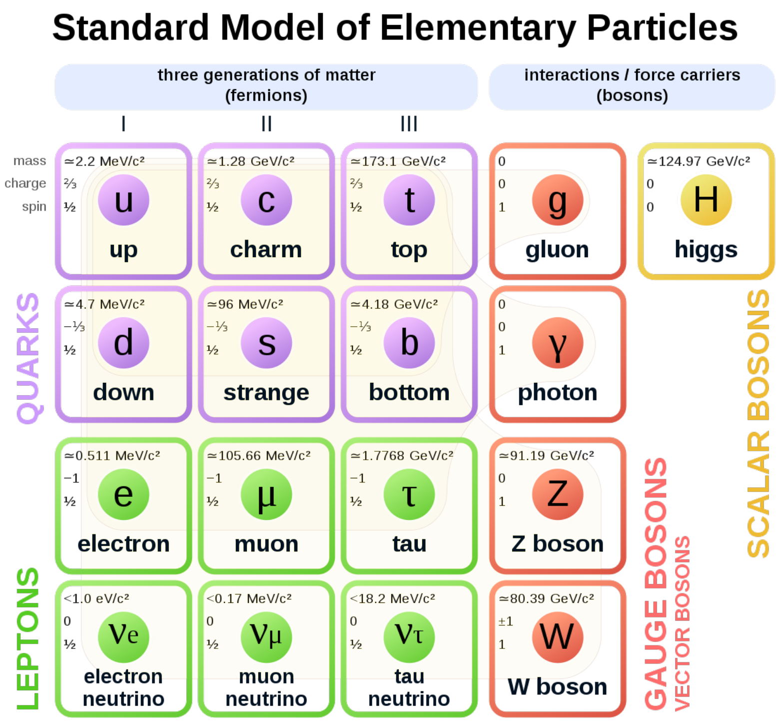

Standard Model of Elementary Particles

	three generations of matter (fermions)			interactions / force carriers (bosons)	
	I	II	III		
mass charge spin	≈2.2 MeV/c^2 ⅔ ½ u up	≈1.28 GeV/c^2 ⅔ ½ c charm	≈173.1 GeV/c^2 ⅔ ½ t top	0 0 1 g gluon	≈124.97 GeV/c^2 0 0 H higgs
QUARKS	≈4.7 MeV/c^2 −⅓ ½ d down	≈96 MeV/c^2 −⅓ ½ s strange	≈4.18 GeV/c^2 −⅓ ½ b bottom	0 0 1 γ photon	SCALAR BOSONS
	≈0.511 MeV/c^2 −1 ½ e electron	≈105.66 MeV/c^2 −1 ½ μ muon	≈1.7768 GeV/c^2 −1 ½ τ tau	≈91.19 GeV/c^2 0 1 Z Z boson	GAUGE BOSONS VECTOR BOSONS
LEPTONS	<1.0 eV/c^2 0 ½ ν_e electron neutrino	<0.17 MeV/c^2 0 ½ ν_μ muon neutrino	<18.2 MeV/c^2 0 ½ ν_τ tau neutrino	≈80.39 GeV/c^2 ±1 1 W W boson	

Figure 1.2: *This is the Standard Model of Particle Physics*

between data and the SM. This in itself testament to the success of the current theory of the SM and is in sharp contrast to the revolutionary state of play in the 1960-70s [1] when the theory of QCD was born.

Throughout the 1960s, many experiments using cloud chambers were conducted to study hadrons. This led to the discovery of countless mesons and baryons which we need not recount here. This did, however, lead to an interesting observation that the spectrum of these baryons and mesons seemed to obey an approximate global $\mathbf{SU}(3)$ symmetry. In 1964, Murray Gell-Mann [28] and George Zweig [38] independently presented the idea of the Quark Model based on fundamental particles with spin-$\frac{1}{2}$. The assertion was that mesons were composed of a quark and an anti-quark, whereas baryons were composed of three quarks. This was later confirmed to be true following a *Deep-Inelastic-Scattering* (DIS) experiment conducted in 1969 at *SLAC* where it was observed that baryons and mesons appeared to have the predicted

---

[1] in particular, 1964, which saw independent models for Electroweak Symmetry Breaking [19,20], independent proposals for the quark model [28, 38] and a proposal for the fundamental color charge [39]

substructure [27] and followed an approximate $\mathbf{SU}(3)$ symmetry.

This led to the discovery of the up (u), down (d), and strange (s) quarks, followed by subsequent discoveries of the charm (c) quark in 1974 [29], the bottom (b) quark in 1977 [32] and finally the top (t) quark in 1999 [36]. That concluded the discovery of all six *flavors* of quark. These formally are arranged into doublets, with the *up-type* quarks (u, c and t) possessing electric charge $+\frac{2}{3}e$, and the *down-type* quarks (d, s and b) having charge $-\frac{1}{3}e$. Anti-quarks have the same arrangement except with the opposite electric charge.

Unfortunately, this model failed to explain the existence of two spin-$\frac{3}{2}$ baryons which consisted only of one flavor of quark: the Δ^{++} (uuu) and Ω^{-} (sss) baryons. This was a problem for the model, since quarks were proposed to be spin-$\frac{1}{2}$ particles, and therefore must obey *Fermi-Dirac statistics.* It was not possible to marry the quantum numbers of the particles involved in these bound states with *Pauli's Exclusion Principle.* Remarkably in the same year as quarks were posited, Oscar Greenberg solved this problem by the proposal of the concept of a new hidden value for quarks, *color charge* [39].

Modifying the theory with this additional quantum number to accommodate the Δ^{++} (uuu) and Ω^{-} (sss) baryons, came with a caveat: an additional arbitrary symmetry of nature, $\mathbf{SU}(N_C)$. This was not related to the approximate global $\mathbf{SU}(3)$ symmetry, but was a real symmetry which seemed to be observed, the major physical implication of this symmetry was that quarks had an additional quantum number, color, which gives an additional degree of freedom in the states available. This symmetry of nature did not help to explain why hadrons and all other particles discovered to this point were color singlets and did not transform under this symmetry. These problems were countered in 1973 when it was realised that the symmetry imposed was not another global one, but a local *gauge* symmetry.

With this realisation, it was clear that each quark field $\psi_i(x)$, with its color state, denoted by the color index, i, at any point in space-time, x transformed under this symmetry as:

$$\psi_i(x) = U_{ij}(x)\psi_j(x)\,, \tag{1.1.1}$$

where $U_{ij}(x) = e^{ig_s\alpha^a(x)T^a}$ with g_s as some scaling factor for the generators of the $\mathbf{SU}(N_C)$ symmetry, T^a, which obey the *Lie algebra*:

$$[T^a, T^b] = if_{abc}T^c\,, \tag{1.1.2}$$

where f_{abc} are structure constants. This promotion to local gauge symmetry within the non-Abelian group, $\mathbf{SU}_C(3)$[1], realised by David Politzer [40], and also by David Gross and Frank Wilczek [41] led to the concept of *asymptotic freedom* as well as that of *confinement*, finally providing an explanation for why hadrons were color singlets, as well as a Nobel Prize for the trio.

Thus was born QCD, the theory which governs the strong interactions of quarks and gluons. It is the $\mathbf{SU}_C(3)$ component of the $\mathbf{SU}_C(3)\times\mathbf{SU}_L(2)\times\mathbf{U}_\mathrm{Y}(1)$ Standard Model of Particle Physics which is in itself a *Quantum Field Theory* (QFT) which is a combination of *Special Relativity* and *Quantum Mechanics*, with some useful concepts from *Classical Field Theory.* In the SM, each particle is an excited quantum of an underlying field and the interactions of these particles are described by interaction terms in the corresponding Lagrangian. In perturbative field theories, we can then visualise these interactions with *Feynman diagrams* and calculate them with the use of *Feynman rules.* This will be explored in Section 1.3, but for now, let us look at the QCD Lagrangian.

1.2 QCD Lagrangian

As described briefly in Section 1.1, the Lagrangian is the starting point for any QFT. We encode all the information we have about particle content, coupling strengths and interactions within the theory itself. The Lagrangian, L, itself is related to the

---

[1] where the subscript simply signifies this is a color symmetry

action, S, through a simple time integral:

$$S = \int L \; dt \,. \tag{1.2.1}$$

The action can alternatively be considered an integral over all space of the *Lagrangian Density*, $\mathcal{L}$, this will be dependent on the set of fields in the theory, ϕ as well as their derivatives. We will from this point on refer to the Lagrangian Density simply as the Lagrangian, and we see that the action functional is:

$$S = \int \mathcal{L}(\phi(x), \partial_\mu \phi(x)) \; d^4x \,. \tag{1.2.2}$$

1.2.1 Quark Content

The quark fields $\psi(x)$ we introduced in Section 1.1 are in fact spin-$\frac{1}{2}$ Dirac Fields, and therefore will (when not interacting) obey the Dirac equation [11]:

$$(i\partial\!\!\!/ - m)\psi(x) = 0 \,, \tag{1.2.3}$$

where m is the mass of the corresponding quanta and *Feynman slash notation*:

$$A\!\!\!/ := \gamma^\mu A_\mu \,, \tag{1.2.4}$$

has been used, and where we have implicitly used *Einstein summation notation* for the contraction of the *Dirac Gamma Matrices*, γ^μ, that satisfy the *Clifford algebra*:

$$\{\gamma^\mu, \gamma^\nu\} = 2g^{\mu\nu} \,. \tag{1.2.5}$$

Further we represent anti-quarks by the conjugate fields: $\bar{\psi}(x) := \psi^\dagger \gamma^0$. This is used, instead of the obvious choice, $\psi^\dagger$, to preserve Lorentz invariance in the theory. At this point, we can state the standard '*free*' Dirac Lagrangian [11]:

$$\mathcal{L}_{\text{Dirac}} = \sum_{f=\text{flavors}} \bar{\psi}_f(x)(i\partial\!\!\!/ - m)\psi_f(x) \,, \tag{1.2.6}$$

where we ensure to include a term for each flavor of quark. From this point on, this summation will be implicit for all quark fields $\psi(x)$. As a brief sanity check at this point, we can utilise the *principle of least action* on Eq. (1.2.2) and obtain the *Euler-Lagrange* (E-L) equations:

$$\partial_\mu \left(\frac{\partial \mathcal{L}}{\partial(\partial_\mu \bar{\psi}(x))} \right) - \frac{\partial \mathcal{L}}{\partial \bar{\psi}(x)} = 0 \,, \tag{1.2.7}$$

which, when applied to Eq. (1.2.6) for the field $\psi(x)$, one obtains the Dirac Equation (1.2.3) once more. One can also apply the E-L equations to the field $\psi(x)$ instead, and would obtain the conjugate Dirac equation:

$$\bar{\psi}(x)\Big(i\overleftarrow{\not\partial} + m \Big) = 0 \,. \tag{1.2.8}$$

1.2.2 The Consequences of Gauged Actions

This all works then, for a generic Dirac spin-$\frac{1}{2}$ field which obeys any and all global symmetries. Unfortunately, as we discussed in Section 1.1, QCD contains a gauge symmetry as specified in Eq. (1.1.1). If we transform the quark fields $\psi_i(x) \to \psi' = e^{ig_s\alpha^a(x)T^a}\psi_j(x)$, it is quickly apparent that our proposed Lagrangian is not gauge invariant:

$$\begin{aligned}
\mathcal{L}'_{\text{Dirac}} &= \bar{\psi}'(x)(i\not\partial - m)\psi'(x) \\
&= \bar{\psi}(x)U^\dagger(x)(i\not\partial - m)U(x)\psi(x) \\
&= \bar{\psi}(x)(i\not\partial - m)\psi(x) + i\bar{\psi}U^\dagger(x)\gamma^\mu \Big[\partial_\mu U(x)\Big]\,\psi(x) \\
&= \mathcal{L}_{\text{Dirac}} + i\bar{\psi}U^\dagger(x)\gamma^\mu \Big[i(\partial_\mu\alpha^a(x))T^a e^{ig_s\alpha^a(x)T^a}\Big]\,\psi(x) \,.
\end{aligned} \tag{1.2.9}$$

This can be solved by an upgrade to our derivative to a *covariant derivative*, D_μ, which contains our partial derivative, ∂_μ, but transforms in such a way that this extra term cancels. If we define the covariant derivative D_μ as:

$$D_\mu\psi(x) = (\partial_\mu - ig_s A^a_\mu(x)T^a)\psi(x) \,, \tag{1.2.10}$$

where g_s is the strong coupling constant and $A^a_\mu(x)$ is the *vector potential* which corresponds to the gluon. Requiring that the covariant derivative transform covariantly,

$$D'_\mu\psi'(x) = U(x)\,D_\mu\psi(x) \,, \tag{1.2.11}$$

fixes the transformation of the gauge field. Writing $A_\mu \equiv A_\mu^a T^a$ and $U(x) = e^{ig_s\alpha^a(x)T^a}$, we obtain

$$A'_\mu(x) = U(x)\,A_\mu(x)\,U^{-1}(x) + \frac{i}{g_s}\,(\partial_\mu U(x))\,U^{-1}(x)\,. \tag{1.2.12}$$

For an infinitesimal transformation $U \simeq 1 + ig_s\alpha^a T^a$, this becomes

$$A_\mu^{a\prime}(x) = A_\mu^a(x) - \partial_\mu\alpha^a(x) - g_s f^{abc}\,\alpha^b(x)\,A_\mu^c(x)\,. \tag{1.2.13}$$

In the Abelian case ($f^{abc} = 0$), this reduces to the familiar form $A'_\mu = A_\mu - \partial_\mu\alpha$ [42]. This vector potential corresponds to the gluon field with a color index, a, which runs from $a = 1$ to $N_c^2 - 1 = 8$. This is because the gluons transform under the adjoint representation of the $\mathbf{SU}(N_c)$ color group. At this point we divulge a particular representation of the corresponding generators, T^a, as introduced in Section 1.1:

$$T^a = \frac{\lambda_a}{2}\,, \tag{1.2.14}$$

where λ_a are the eight 3×3, traceless and Hermitian *Gell-Mann Matrices*. These are a natural extension of the *Pauli Matrices*, which are the basis for the originally proposed $\mathbf{SU}(2)$ quark model [28]. They are normalised to the value of 2, such that the embedded Pauli Matrices are conventionally normalised. This leads to the halving in Equation (1.2.14) and to the following properties:

$$Tr\left[\lambda_i\,\lambda_j\right] = 2\delta_{ij} \tag{1.2.15}$$

$$Tr\left[T^i\,T^j\right] = \tfrac{1}{2}\delta_{ij}\,, \tag{1.2.16}$$

where δ_{ij} is the Kronecker delta. Note, Equation(1.2.10) shows us that the derivatives of the (anti-)quark fields transform like (anti-)quark fields: in the (anti-)fundamental representation of the $\mathbf{SU}(3)$ color group.

We can now slot our covariant derivative (1.2.10) into our Dirac Lagrangian (1.2.6) to obtain a gauge invariant version:

$$\mathcal{L}_{\mathrm{Dirac\,Inv}} = \bar{\psi}(x)(i\not{D} - m)\psi(x)\,. \tag{1.2.17}$$

This is a triumph; we now have a Lagrangian which respects the theorised local symmetry transformations from Equation (1.1.1). Secondly, this requirement naturally leads to the inclusion of the interaction of quarks with gluons, in the description of the dynamics of the quark fields. We also note that Eq. (1.2.13) makes us conclude, that adding a gluon Dirac mass term $\sim m_g A_\mu A^\mu$ is impossible, since it would violate gauge invariance.

What we lack in this new description is the dynamics of the gluons themselves. The gluon gauge field already exists inside our covariant derivative, and since we obtain the dynamics of a field through derivatives, it is natural to look at the commutator of this. This gives us the *Field Strength Tensor* [11], $F_{\mu\nu}$:

$$\begin{aligned} F_{\mu\nu} &= \frac{i}{g_s}[D_\mu, D_\nu] \\ &= \partial_\mu A^a_\nu(x)T^a - \partial_\nu A^a_\mu(x)T^a - igA^a_\mu(x)A^b_\nu(x)[T^a, T^b] \\ &= \partial_\mu A^a_\nu(x)T^a - \partial_\nu A^a_\mu(x)T^a + g_s A^a_\mu(x)A^b_\nu(x)(f_{abc}T^c) \\ &= \left(\partial_\mu A^a_\nu(x) - \partial_\nu A^a_\mu(x) + g_s A^b_\mu(x)A^c_\nu(x)f_{bca}\right)T^a \\ &= F^a_{\mu\nu}T^a \,, \end{aligned} \tag{1.2.18}$$

where we have used the Lie Algebra to resolve the commutator in the second line. We note that if our symmetry group was Abelian, the last term would vanish, as is the case in QED [11]. In QCD, what arises as a consequence of this is gluon self-interaction, which is notably absent in QED. Unfortunately, this extra term also has consequence and this problem is manifest if we gauge transform:

$$\begin{aligned} F'_{\mu\nu} &= \frac{i}{g_s}[D'_\mu, D'_\nu] \\ &= \frac{i}{g_s}[U(x)D_\mu U^\dagger(x), U(x)D_\nu U^\dagger(x)] \\ &= \frac{i}{g_s}U(x)[D_\mu, D_\nu]U^\dagger(x) \\ &= U(x)F_{\mu\nu}U^\dagger(x) \,. \end{aligned} \tag{1.2.19}$$

The field strength tensor is not gauge invariant in QCD, which means we cannot include it in the form above. Luckily, the trace of the field strength tensor *is* gauge invariant:

$$Tr\left[F'_{\mu\nu}\right] = Tr\left[U(x)F_{\mu\nu}U^\dagger(x)\right] = Tr\left[F_{\mu\nu}U^\dagger(x)U(x)\right] = Tr\left[F_{\mu\nu}\right]. \qquad (1.2.20)$$

However, since we need our Lagrangian to also be Lorentz invariant, we cannot simply add it in by itself, since it transforms as a rank-2 tensor under Lorentz transformations. We need to contract it with something, and an obvious candidate for this is itself. We can rewrite it as:

$$Tr\left[F_{\mu\nu}F^{\mu\nu}\right] = Tr\left[F^a_{\mu\nu}\,T^a\;F^{b\,\mu\nu}\,T^b\right] = F^a_{\mu\nu}F^{b\,\mu\nu}\;Tr\left[T^aT^b\right] = \frac{1}{2}\,F^a_{\mu\nu}F^{a\,\mu\nu}. \quad (1.2.21)$$

If we place this in our gauge invariant Dirac Lagrangian, Equation (1.2.17), we arrive at the famous *Yang-Mills Lagrangian* [11]:

$$\mathcal{L}_{\text{Yang-Mills}} = -\frac{1}{4}F^a_{\mu\nu}F^{a\,\mu\nu} + \bar{\psi}(x)(i\not{D} - m)\psi(x)\,, \qquad (1.2.22)$$

where the $-\frac{1}{4}$ coefficient is simply a normalisation. We now have a gauge invariant Lagrangian which includes all of the particle content which we wanted at the outset; however, if we wish to quantise the theory we will need to add some final terms. First, we need to break the gauge invariance which we worked so hard to achieve. We will introduce a gauge fixing term as one would obtain from the *Faddeev-Popov* method of gauge fixing [42]:

$$\mathcal{L}_{\text{Gauge-Fix}} = -\frac{1}{2\xi}(\partial^\mu A^a_\mu)^2\,, \qquad (1.2.23)$$

where ξ is any finite constant, and is a free parameter of the theory that fixes our gauge choice. The end result will be independent of gauge, but different calculations are easier in different gauges. Two frequently used gauges are:

$$\begin{array}{ll} \xi \to 0 & \text{Landau gauge} \\ \xi \to 1 & \text{Feynman gauge}\,. \end{array}$$

Since the Lagrangian is invariant under gauge transformation, this gauge fixing is necessary to avoid integration over an infinite set of physically equivalent degrees of freedom. In Non-Abelian theories, this gives rise to a new problem: the gauge bosons have non-physical time-like and longitudinal polarisation states which must be cancelled. These are removed by the addition of one final term to our QCD Lagrangian [43]:

$$\mathcal{L}_{\text{FP-Ghosts}} = \bar{c}^a \left(-\partial^2 \delta^{ac} - g_s \partial^\mu f^{abc} A^b_\mu \right) c^c \,, \tag{1.2.24}$$

where the complex scalar fields c and $\bar{c}$ known as *Faddeev-Popov ghosts*, are used to cancel the extra degrees of freedom present in the gauge bosons. These non-physical fields must be included for higher-order calculations unless one chooses an appropriate gauge. Following this, we have our full QCD Lagrangian:

$$\mathcal{L}_{\text{QCD}} = \mathcal{L}_{\text{Yang-Mills}} + \mathcal{L}_{\text{Gauge-Fix}} + \mathcal{L}_{\text{FP-Ghosts}} \,. \tag{1.2.25}$$

This contains our best description of the strong force, including the particle content and also their interactions. It is from this that we can derive formulae which can be compared against experiment.

1.2.3 The Θ Term and the Strong CP Problem

While the QCD Lagrangian presented in Equation (1.2.25) offers a comprehensive description of the strong interactions, it is not entirely complete. An additional term, known as the Θ *term*, can be incorporated without violating the renormalizability of the theory:

$$\mathcal{L}_\Theta = \Theta \frac{g_s^2}{32\pi^2} F^a_{\mu\nu} \tilde{F}^{a\,\mu\nu} \,, \tag{1.2.26}$$

where $\tilde{F}^{a\,\mu\nu} = \frac{1}{2}\epsilon^{\mu\nu\rho\sigma} F^a_{\rho\sigma}$ is its dual, and Θ is a dimensionless parameter.

The inclusion of the Θ term introduces CP (charge-parity) violation into the strong interactions. Experimentally, however, such CP violation in QCD is highly constrained. For instance, the non-observation of the neutron electric dipole moment imposes that Θ must be extremely small, $\Theta \lesssim 10^{-10}$. This fine-tuning problem is known as the *strong CP problem*.

Several theoretical solutions have been proposed to address the strong CP problem.

The most prominent among them is the Peccei-Quinn mechanism [44], which introduces a new global symmetry that dynamically relaxes Θ to zero. This mechanism predicts the existence of a new pseudo-Nambu-Goldstone boson, the axion, which is also a viable dark matter candidate.

In summary, while the Θ term is allowed by the symmetries of QCD, its physical implications lead to significant theoretical challenges. The absence of observed CP violation in strong interactions suggests that either Θ is incredibly small or that new physics mechanisms, such as the Peccei-Quinn symmetry, are at play.

1.3 From Feynman rules to Cross-Sections

We have our theory of Quantum Chromodynamics, but without further manipulation this does not tell us much. To verify our findings above, we look explicitly into the interactions of particles in our QCD Lagrangian, Eq. (1.2.25) and make predictions as to the resultant particles from collisions and their respective likelihood. We then compare this to experimental results, such as those at the LHC[1].

The number of scattering events per time N is related to the *flux* of incoming particles, $F = 4\sqrt{(p_a \cdot p_b)^2 - m_a m_b}$, by the *cross-section*, σ:

$$\sigma = \frac{N}{F}\,. \tag{1.3.1}$$

This effective area can be interpreted as a probability for a particular interaction to occur, and in turn can be related to a transition amplitude between initial and final states of definite momentum, the *S-Matrix*, S:

$$\langle f|S-1|i\rangle \equiv \langle f|iT|i\rangle = (2\pi)^4\delta^4(p_f - p_i)i\mathcal{M}_{fi}\,, \tag{1.3.2}$$

where we have used isolated the interacting part of the S-Matrix T, as $S = 1 + iT$.

---

[1] The experimental undertaking here is remarkably complex, and the LHC from accelerators to detectors is a marvel of engineering. The complications arising from this are beyond the scope of this text, but I implore the reader to not underestimate the sheer scale and ingenuity of the experiments which provide the data compared to within this text

This gives us our *Lorentz invariant matrix element* $\mathcal{M}$. From that object, we are able to calculate an event rate in the form of:

$$\hat{\sigma} = \int \left(\prod_f \frac{d^3 p_f}{(2\pi)^3} \frac{1}{2E_f} \right) \frac{|\mathcal{M}_{fi}|^2}{2E_{i_1} E_{i_2} |\nu_{i_1} - \nu_{i_2}|} (2\pi)^4 \delta^4 (p_f - p_i) \,, \tag{1.3.3}$$

where the ˆ signifies that this is a *partonic* cross-section, describing the rate of interaction of the fundamental partons which we model within the Matrix Element. We will see in Eq. (1.3.30) just how easily this can be utilised to then calculate something which can be compared against the measurements from experiments. For now, we consider the matrix elements themselves, which may be calculated through the use of Feynman rules. The basic premise is that $i\mathcal{M}$ is equal to the sum of all *connected*, *amputated* Feynman diagrams. By calling for diagrams to be connected we do not calculate extra terms which only contribute a phase shift in the vacuum energy which is not relevant to the quantity we wish to calculate. This is, in short, because it excludes vacuum bubbles and ensures that all external lines are connected. By ‘amputated’, we require that any loops attached to external legs also interact with another part of the diagram and that the effect isn’t just localised to a single leg of the diagram. We will discuss this concept more in depth later in Section 1.3.1.

Tables 1.2 and 1.3 show the correspondence between Feynman diagram elements in QCD and their contribution to the overall diagram. There are further constraints on these diagrams, and these follow:

- Dirac indices are contracted along Feynman lines
- Momentum must be conserved at each vertex
- Each loop contains an undetermined momenta p_i, which must be integrated over with $\frac{d^4 p_i}{(2\pi)^4}$
- There is a factor of -1 for each fermion or ghost loop within the diagram
- There is a relative factor of -1 for each odd permutation of fermions.

- There is a symmetry factor which needs to be divided out in the case of identical particles.

External fermion lines in Feynman diagrams correspond to the four component spinors $u^s(p)$ and $v^s(p)$ which are the positive ($\psi(x) = u^s(p)\, e^{-ip\cdot x}$) and negative ($\psi(x) = v^s(p)\, e^{+ip\cdot x}$) frequency solutions to the Dirac Eq. (1.2.3). This actually heralded the prediction of anti-matter, by Dirac in 1928 (see Table 1.1).

These spinors satisfy the special property known as *spin sums*:

$$\sum_s u^s(p)\, \bar{u}^s(p) = \not{p} + m \tag{1.3.4}$$

$$\sum_s v^s(p)\, \bar{v}^s(p) = \not{p} - m\,, \tag{1.3.5}$$

and can be represented themselves, by:

$$u^s(p) = \begin{pmatrix} \sqrt{p\cdot\sigma}\,\xi^s \\ \sqrt{p\cdot\bar{\sigma}}\,\xi^s \end{pmatrix}, \qquad v^s(p) = \begin{pmatrix} \sqrt{p\cdot\sigma}\,\eta^s \\ -\sqrt{p\cdot\bar{\sigma}}\,\eta^s \end{pmatrix}, \qquad s = 1, 2\,, \tag{1.3.6}$$

where ξ^s and η^s are bases of two component spinors. We can make the choice that $\xi^1 = \left(\begin{smallmatrix}1\\0\end{smallmatrix}\right)$ and $\xi^2 = \left(\begin{smallmatrix}0\\1\end{smallmatrix}\right)$ represent spin-up and spin-down the z-axis respectively. A particle's spin is an intrinsic quantum number, which has many effects on the calculations ahead. Not least, it leads to the concept of a particle's *helicity*: the projection of its spin along the direction of momentum. A particle travelling in the same direction as its spin will have helicity $+s$ and is said to be *right-handed* and a particle travelling conversely to the direction of its spin will have helicity $-s$, and said to be *left-handed.* The same choices for the other basis vectors, η^s, lead to the opposite helicity assignment and left- and right-handed spinors instead. The projection operators, P_{L} and P_{R}, allow us to project the left and right handed components from a spinor:

$$u_{\pm}(p) = P_{\substack{\mathrm{R}\\\mathrm{L}}}\, u(p) = \left(\frac{1 \pm \gamma^5}{2}\right) u(p) \tag{1.3.7}$$

$$\nu_{\mp}(p) = P_{\substack{\mathrm{R}\\\mathrm{L}}}\, v(p) = \left(\frac{1 \pm \gamma^5}{2}\right) v(p)\,, \tag{1.3.8}$$

where γ^5 is the fifth gamma matrix given by $\gamma^5 = -i\gamma^0\gamma^1\gamma^2\gamma^3$. Interestingly enough, we find that in the massless limit, these spinors become equivalent:

$$u_{\pm}(p) = v_{\mp}(p)\,. \tag{1.3.9}$$

This allows us to use the compact *spinor-helicity* notation:

$$u_{\pm}(p) = v_{\mp}(p) = \left|p^{\pm}\right\rangle \tag{1.3.10}$$

$$\bar{u}_{\pm}(p) = \bar{v}_{\mp}(p) = \left\langle p^{\pm}\right| \tag{1.3.11}$$

$$\langle pq\rangle = \langle p^{-}|q^{+}\rangle \tag{1.3.12}$$

$$[pq] = \langle p^{+}|q^{-}\rangle\,. \tag{1.3.13}$$

External gluons on the other hand, are represented by the *polarisation vector* $\varepsilon_\mu(p)$, which, using spinor helicity formalism can be written as:

$$\varepsilon^{\mu}_{\pm}(p,k) = \pm\frac{1}{\sqrt{2}}\frac{\langle k^{\mp}|\gamma^{\mu}|p^{\mp}\rangle}{\langle k^{\mp}p^{\pm}\rangle}\,. \tag{1.3.14}$$

These obey the sum rule:

$$\sum_{\lambda=\pm1}\varepsilon^{\lambda}_{\mu}\left(\varepsilon^{\lambda}_{\nu}\right)^{*} = -g_{\mu\nu} + \frac{p_\mu q_\nu + p_\nu q_\nu}{p\cdot q}\,, \tag{1.3.15}$$

where λ is the helicity of the gluon and q is some reference vector.

A problem should be apparent at this point: if loops are allowed, there are an infinite number of diagrams. Luckily the whole premise of Feynman diagrams is to represent an order-by-order expansion in the strong coupling, α_s, which means we know exactly which diagrams we expect to be most significant and include those in our predictions first. We can therefore make theoretical predictions based on a finite number of diagrams and we can further improve the precision of these predictions by including a higher number of diagrams.

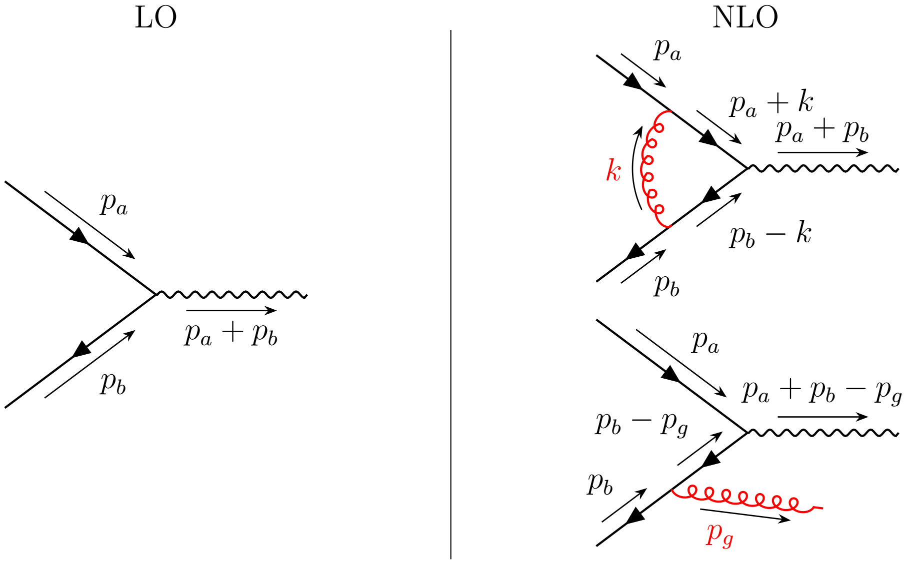

Figure 1.3: *Feynman diagrams representing the increasing contributions in FO contributions at increasing orders.*

Indeed, the partonic cross-section can be treated as a perturbative expansion in α_s:

$$\begin{aligned} d\hat{\sigma}_{ij} &= \sum_{n=0}^{\infty} \left(\frac{\alpha_s}{2\pi}\right)^n d\hat{\sigma}_{ij}^{(n)} \\ &= d\hat{\sigma}_{ij,\,LO} + \left(\frac{\alpha_s}{2\pi}\right) d\hat{\sigma}_{ij,\,NLO} + \left(\frac{\alpha_s}{2\pi}\right)^2 d\hat{\sigma}_{ij,\,NNLO} + \dots\,, \end{aligned} \tag{1.3.16}$$

where the lowest order term is referred to as *Leading Order* (LO), and subsequent terms are labelled *Next-to-leading order* (NLO) and *Next-to-Next-to-leading order* (NNLO). Each successive term either adds an extra external particle into the diagram or a loop, which unlocks new diagrams which can be drawn.

We begin by noticing that any higher-order corrections in the perturbative series of the strong coupling constant is going to add an extra factor α_s, the premise, as stated before being that because the value of this is small, the series will converge despite the numerous new possibilities of diagrams each new 'order' presents. For each additional 'N' new diagrams are possible, since each new term adds a particle into the Feynman diagram representation of a process. There are two ways to add a new particle: as an internal *virtual* line or as an external line. These break down the two key components of higher-order corrections in *Fixed Order QCD*. If a new internal line is added, this is a *virtual correction*, and if a new external line is added this is a *real emission*. These successive corrections can be seen in Fig. 1.3 for the case of the production of a boson from a quark line.

If we consider these diagrams further, we encounter significant computational problems. Specifically, if we look at one of the NLO corrections contained in Fig. 1.3, the one loop (virtual) correction to the quark-gluon vertex diagram we will see two types of divergence. The unconstrained loop momenta needs to be integrated over, and this integral can be expressed as:

$$I_{\text{loop}} = \int \frac{d^4k}{(2\pi)^4} \frac{(\not{p}_a + \not{k})(-ie\gamma_\mu)(\not{k} - \not{p}_b)}{k^2 (k+p_a)^2 (k-p_b)^2} \,. \tag{1.3.17}$$

If we consider the case in which the virtual particle is high energy and $k^2 \gg p^2$ we see that:

$$\begin{aligned} I_{\text{loop}} &\sim \int_0^\infty \frac{d^4k}{(2\pi)^4} \frac{k^2}{k^6} \\ &\sim \int d\Omega_3 \int_0^\Lambda \frac{d|k|}{(2\pi)^4} \frac{|k|^5}{|k|^6} \\ &\sim \lim_{\Lambda \to \infty} \log(\Lambda) \,, \end{aligned} \tag{1.3.18}$$

where Λ is some ultraviolet cut-off we have introduced to regulate the divergence. Notably, it is clear that the diagram diverges as we move this cut-off to infinity, and so our integral does indeed diverge as $k \to \infty$, as this occurs at large momenta, the divergence is termed an *ultraviolet* (UV) divergence.

Another divergence can be seen in the massless limit; however, an unphysical mass parameter can be added, μ, to demonstrate this:

$$I_{\text{loop}} = \int_0^\infty \frac{d^4k}{(2\pi)^4} \frac{(\not{p}_a + \not{k})(-ie\gamma_\mu)(\not{k} - \not{p}_b)}{[k^2 - \mu^2][(p_a + k)^2 - \mu^2][(k-p_b)^2 - \mu^2]} \,, \tag{1.3.19}$$

which leads to terms of the form:

$$\log^2 \left(\frac{-\hat{s}^2}{\mu^2} \right) \,, \tag{1.3.20}$$

where s is a *mandelstam variable*, $\hat{s} = (p_a + p_b)^2$ for this process, which will be discussed in greater detail later in Section 2.1. This expression is termed a *Sudakov Logarithm*, and we will discuss its significance later. This will clearly diverge in the case of massless particles ($\mu \to 0$). Whereas the UV divergence corresponds to the high energy loop momenta, the divergence here corresponds to the case where the momenta goes to zero. This type of divergence is known as an *infrared* (IR) divergence. In the next few sections we will discuss the implications of and how to approach the problems associated with these divergences.

1.3.1 Regularising UV Divergences in QFT

This perturbative description of QFTs naturally brings in discussion of higher-order loop diagrams and virtual corrections. As we discussed above, these lead to divergences since the momentum in the virtual particles is allowed to range to infinity. To manage these high-energy divergences, we introduce a regularisation process, which subsequently leads to the introduction of a 'renormalisation' scale, μ_r. Measurable observables must be independent of this scale that is defined within the *Renormalisation Group Equations*:

$$\begin{aligned} 0 &= \mu_r^2 \frac{d}{d\mu_r^2} \mathcal{O}\left(\log\frac{q^2}{\mu_R^2}, \alpha_s(\mu_R^2)\right) && (1.3.21) \\ &= \left[\frac{\partial}{\partial \log(q^2/\mu_R^2)} + \beta(\alpha_s)\partial_{\alpha_s}\right] \mathcal{O}\left(\log\frac{q^2}{\mu_R^2}, \alpha_s(\mu_R^2)\right) , && (1.3.22) \end{aligned}$$

where the beta function:

$$\beta(\alpha_s(\mu_R^2)) = \mu_R^2 \frac{\partial \alpha_s(\mu_R^2)}{\partial \mu_R^2} , \tag{1.3.23}$$

describes the rate of change of the renormalised coupling with respect to the renormalisation scale, and $\alpha_s = g_s/4\pi$ is the strong coupling constant. The μ_r-dependence is moved from the observables in the theory to the coupling, and also the particle masses.

This running of the coupling is a fundamental property of QFT itself, and not an artifact of numerical trickery. In fact, this can be modelled and even used to test the SM. Eq. (1.3.23) can be expanded perturbatively as a series in α_s:

$$\beta(\alpha_s) = -\beta_0\alpha_s(1 + \beta_1\alpha_s + \beta_2\alpha_s^2 + \dots)\,, \tag{1.3.24}$$

where β_i are the perturbative coefficients of each term. For QCD, this β-function is known to five-loops [45, 46]. The leading order contribution, β_0 is given by:

$$\beta_0 = \frac{11 - 2n_f}{3}\,, \tag{1.3.25}$$

which is positive for a small enough number of quarks, n_f. If we truncate Eq. (1.3.24) at leading order, we can solve Eq. (1.3.23) and we see that the coupling runs with the following form:

$$\alpha_s(\mu_R^2) = \frac{g_s^2(\mu_R^2)}{4\pi} = \frac{\alpha_s(\mu_0^2)}{1 + \alpha_s(\mu_0^2)\frac{\beta_0}{4\pi}\ln\frac{\mu_R^2}{\mu_0^2}}\,, \tag{1.3.26}$$

where μ_0 is some reference scale at which it may be measured.

In the SM, the sign of the beta function is negative and thus leads to the concept of *confinement* at 'low' energies and also *asymptotic freedom* at 'high' energies, since the coupling strength decreases with increasing energy scale. This differs from QED, where β_0 has a negative coefficient causing the coupling strength to grow with energy. If we consider the weak interaction, we see that it also has a positive β_0 value, but that it is suppressed below the $W^{\pm}$-Boson and Z-Boson mass thresholds and as such the strong force dominates soft physics.

For $\mu_R = \mu_0 = \mathcal{O}(0.2\text{GeV})$ the strong coupling diverges, which physically manifests in the observation of *color confinement* in which partons always group into color-neutral hadrons. This also highlights the scale at which we expect the perturbative predictions to break down. Indeed, as one approaches $\alpha_s \sim 1$, other predictive methods and models (such as Lattice QCD) must be used to predict the interactions of particles.

Finally we note that physical observables will be independent of the choice of this scale, since it is an artifact of our numerical dealings around divergences. Since we are not calculating the theory to all orders; instead, we truncate the series we will end up with some residual dependence on this scale choice. Since physical observables should not depend on the scale choice; any fluctuation in the values of physical observables due to the scale choice used can be considered a decent theoretical uncertainty. Further, if the variation in values obtained is reduced as more terms in the perturbative series are calculated, we know that the underlying perturbation theory is at least a theoretically sound approach.

1.3.2 IR Divergences and Dimensional Regularisation

The next type of divergence we have to deal with arises in several places within the perturbative calculations: loop diagrams with arbitrarily small momenta; and real emissions wherein the momenta of an external particle becomes too soft or collinear with other external particles. These both are scenarios in which the momenta can no longer be resolved, and as in the case of UV divergences, our instinct is to insert a scale where we no longer think we are able to model the resultant physics. That is, we separate the physics into long and short distance scales, into perturbative and non-perturbative regimes. To showcase these two, separate problems, we use the real emission depicted in Fig. 1.4. Following the Feynman rule for a quark propagator in Table 1.2, we can describe the quark propagator with the following expression:

$$\begin{aligned} P_q &\sim \frac{\not{q} + \not{k}}{(q^\mu + k^\mu)^2} \\ &\sim \frac{\not{q} + \not{k}}{2E_q E_k (1 - \cos(\theta_{qg}))}\,, \end{aligned} \tag{1.3.27}$$

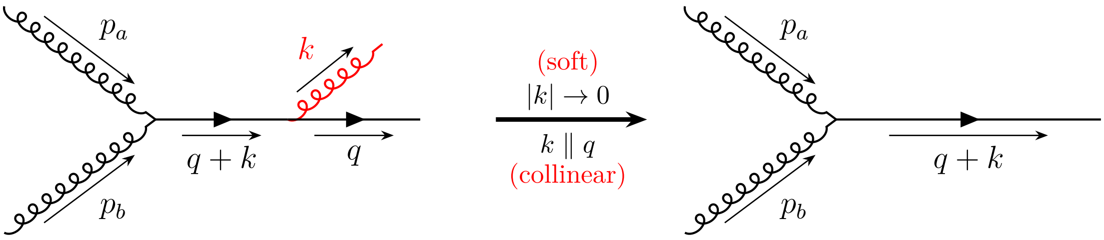

Figure 1.4: *A real gluonic emission becoming unresolved in both the soft and collinear limits*

where θ_{qg} is the angle between the gluon and quark's trajectories, and E_q and E_k are the energies of particles q and k respectively. It is clear at this point that the propagator with diverge in two scenarios which we qualitatively described earlier:

1. $E_k \to 0$, the *soft* limit,
2. $\theta_{qg} \to 0$, the *collinear* limit.

these limits, depicted in Fig. 1.4, make it clear that these divergences correspond to a scenario in which experimentally the particles can no longer be resolved, and theoretically the states become degenerate. The way this is resolved theoretically is through the use of Jets. We will discuss the concept behind the third initial of `HEJ` in Section 1.4. For now, it is enough to note that this same divergent problem occurs within loops, and so we have IR divergences with the same origins in two different sectors, and it turns out that these divergences cancel. Further, this has actually been shown to be the case for QCD by Kinoshita [47], Lee and Nauenberg [48] for all-orders, in what is known as the *KLN Theorem.* The only requirement is that the calculation is sufficiently *inclusive.*

An inclusive calculation is one in which all diagrams, both real and virtual, are summed over for a given order of α_s. This means that we need to regulate the divergences in both the real and virtual phase-space integrals. This is typically performed by *Dimensional Regularisation*, in which we perform integrations in $d = 4 + 2\epsilon$ dimensions and isolate the divergences in the limit $\epsilon \to 0$. There are many complications in practice with this procedure mostly due to the fact that the divergences we wish to cancel exist within integrations with dimensionally different phase-space measures. Specifically, the virtual corrections exist within the N-body phase-space and the real corrections, exist in $N + 1$-body phase-space.

This is of course theoretically challenging as well as being numerically very expensive. The poles existing in different phase-spaces, and the most common methods of dealing with this issue is through the intoduction of counter-terms. For example, at

NLO:

$$\sigma^{\rm NLO} = \int d\Phi_N \left[\mathcal{B}_n + \mathcal{V}_n + \mathcal{I}_n + \int d\Phi_1 (\mathcal{R}_{n+1} - \mathcal{C}_{n+1})\right] \, , \tag{1.3.28}$$

where B_n is the *Born-level* (in most cases, LO) contribution. The subtraction term $\mathcal{C}_{n+1}$ is the theoretically challenging part of this process, since it needs to have a finite difference from $\mathcal{R}_{n+1}$, while also being analytically integrable to calculate $\mathcal{I}_n$:

$$\int d\Phi_N \left(\mathcal{I}_n - \int d\Phi_1 \mathcal{C}_{n+1}\right) \, . \tag{1.3.29}$$

This at first seems to be quite a problem; although methods for NLO [49] and NNLO [50] have been developed and automated by now. This is, however, without doubt computationally demanding. Aside from the vast extra phase-space which has to be sampled the integrand which has to be resolved is suddenly significantly more complicated. As such, although higher-order calculations are a sledgehammer that will get better results, they become computationally prohibitive rapidly.

1.3.3 PDFs and Factorisation

There is one final problem with our approach thus far. Experimentally we cannot collide colored particles at exact energies, since as discussed earlier, they are bound together in color singlet states. Hence our initial states are hadronic; which inherently means we will be dealing with non-perturbative effects. The spread of energies of these hadronic states is negligible; however, we need to accurately model the substructure. We therefore make a few assumptions about the constituent partons inside of our incoming hadronic states:

1. they are massless
2. they move in parallel with their parent hadrons
3. they each have a different energy fraction, parameterised by the *Bjorken-x* and the sum of these fractions equals unity.

Parton Distribution Functions (PDFs) are structure functions and can be seen as a probabilistic distribution of the contents of any bound state. These depend on the

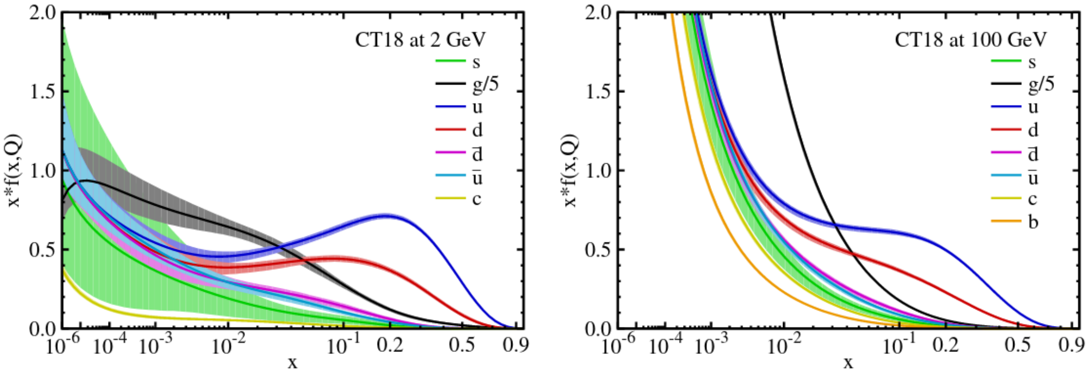

Figure 1.5: *The CT18NLO PDF set presented at two energy scales. Note that the gluon curve has been reduced by a factor of 5. Plot taken from [1]*

energy scale of the scattering, since, as the energy scale is increased the interior of the hadron modelled will be more precisely probed. The distributions are presented as a function of the *Bjorken-x* momentum fraction, x, of any given parton within it. Fig. 1.5 shows how there is a peak for the valence quarks of any given hadron at quite a high momentum fraction but there is also a large number of 'low-x' sea quarks and gluons, which need to be considered also. These are generally derived from experimental data from *Deep Inelastic Scattering* (DIS) experiments and from Lattice QCD results.

The problem with this approach to factorising the soft physics from the perturbative physics is that there is an inherent ambiguity when one considers initial state radiation, since it could be considered a part of the PDF, or a part of the hard process. To better define where an emission belongs, we insert a *factorisation scale*, μ_F, below which an emission is considered a part of the PDF and irrelevant for the hard process, and above which it is an emission which forms a part of our hard process. This expectation is supported by the *factorisation theorem* [51], which allows us to systematically separate the long-distance, non-perturbative physics encapsulated in the PDFs from the short-distance, perturbative hard scattering processes.

Luckily, this technique of factorising the process into different physics scales has been shown to hold to all orders for many scattering processes [51], and is known as the *factorisation theorem*. Further, PDFs are *universal* [52, 53] and as such we can use data from previous collider experiments and from different processes to reduce uncertainties further.

Using these objects, we can actually write down the total proton-proton cross-section as a integral of the partonic cross-section which we detailed in Eq. (1.3.3) and the PDFs of the associated incoming particles for which, we sum over all possibilities, in the *QCD factorisation formula*:

$$d\sigma(P_a, P_b) = \sum_{i,j} \int_0^1 dx_a \int_0^1 dx_b \, f_{i/h_a}(x_a,\, \mu_F)\, f_{j/h_b}(x_b,\, \mu_F)\, d\hat{\sigma}(x_a P_a, x_b P_b, \mu_F, \mu_R)\,, \tag{1.3.30}$$

where i, j denote the partons within the incoming hadrons h_1 and h_2, $x_a P_a$ and $x_b P_b$ are the rescaling of the incoming hadronic momenta P_a and P_b to give the incoming partonic momenta, p_a and p_b. Finally, f_i are the PDFs.

As with the renormalisation scale, this factorisation scale this leaves an imprint on our predictions in the form of residual dependence which physically should not be present. So the deep question remains, how do we choose our factorisation scale, μ_F? As with the renormalisation scale, observables should have no dependence on the value of this scale; however, there are artifacts. When one estimates the error due to the renormalisation scale it is standard practice to also vary the factorisation scale. This is known as *scale variation* and is a helpful tool when parameterising uncertainties to gain a quick understanding of the convergence of the perturbative series.

The dependence of physical observables on the factorisation and renormalisation scales is intrinsically linked to the truncation of the perturbative series. At leading order (LO), both μ_F and μ_R dependence are large, reflecting the significant contributions from higher-order terms that have not yet been included in. As we progress to next-to-leading order (NLO), next-to-next-to-leading order (NNLO), and beyond, the inclusion of additional loop corrections systematically cancels parts of the scale dependence present at lower orders.

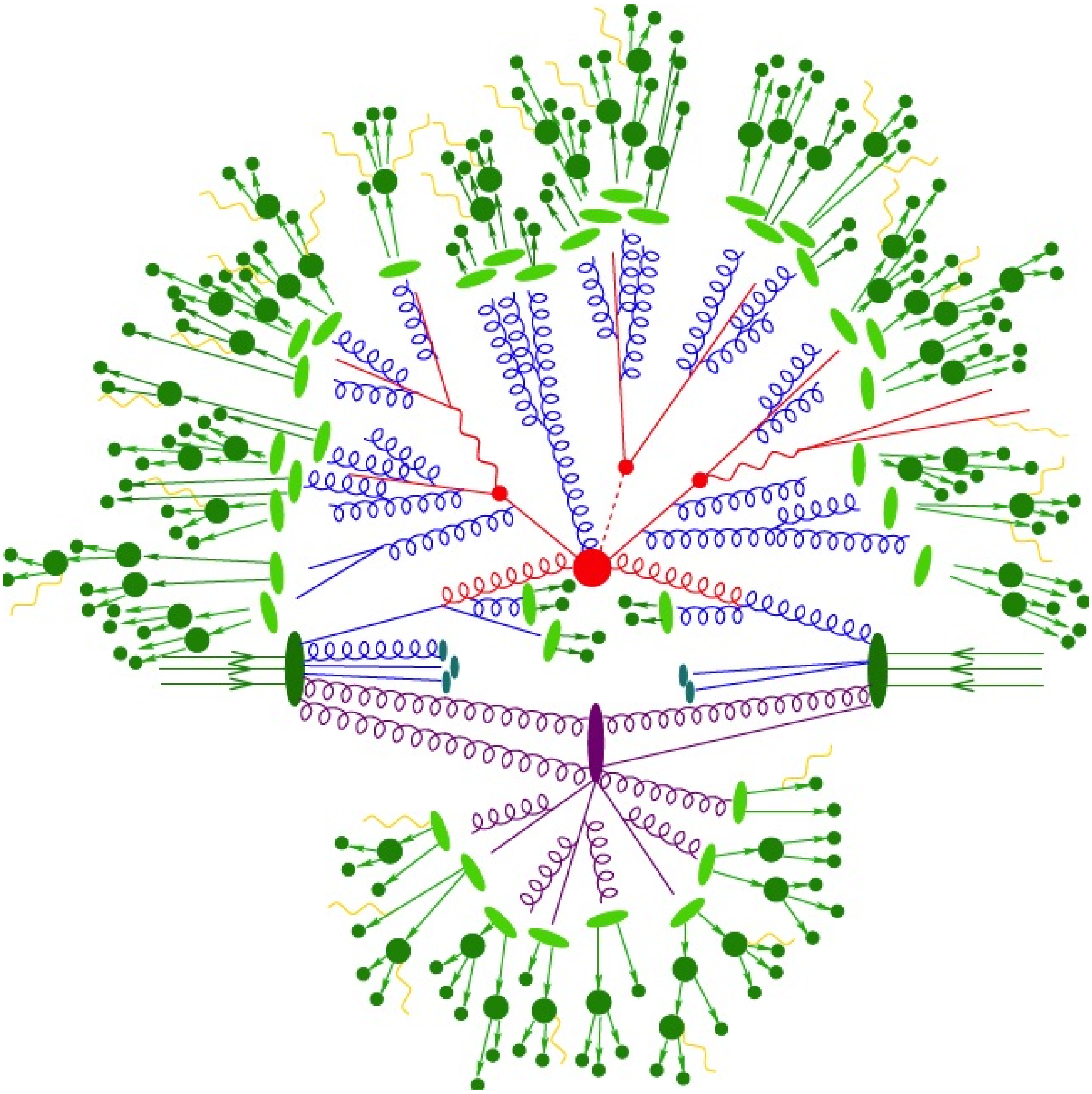

Figure 1.6: *The standard figure [2] which shows how the hard scattering process (red) relates to all other parts of scatterings; parton shower (blue), hadronization (light green), hadron decays (dark green), underlying event (violet) and QED radiation (yellow) which occur for typical proton-proton collisions at Hadron Colliders such as the LHC.*

1.4 Further Improvements

So far we have introduced the QCD Lagrangian and walked from there to the methodology used to obtain a prediction for the rate of collisions at the LHC. While the total cross-section is far from the only thing we wish to look at, specific observables will be discussed later on when we cover the specific job which *High Energy Jets* (HEJ) fulfils when improving the predictions we have discussed so far. Consider the typical looking collision depicted in Fig. 1.6, we now have a route to predict the collision between the dark green incoming hadrons all the way through to the hard process depicted in red.

But this, clearly, is not the full story. We see experiments deviate from these predictions, and even higher-order versions such as NLO all the time. In fact, if one looks at inclusive 2-jet differential cross-sections, there is unwavering agreement for a vast swathe of different distributions; however, if one looks in more granular detail, at some exclusive distributions such as additional jets in vector boson production, see e.g. [54] there are clear issues with this approach.

There are many, many improvements which can be made. Firstly, at an experiment we have no hope measuring colored states at any detector, and instead we need to detect hadronic outgoing particles. Our theoretical predictions are based on a premise: the hard process occurs at very high energy and is partonic in nature. We also know that at lower energy scales, these interacting partons must *hadronise* into bound states, but the scales where both of these processes occur is at odds. In an experiment we actually measure a cone-like structure of energy in the detectors. This experimentally observable phenomenon is called a *Jet*. This needs to be a theoretically sound as well as experimentally valid definition.

Theoretically there are many ways to define a Jet, but all amount to defining a region around a hard parton for which all soft momenta are encapsulated, as well as a *Jet cut*, a scale where any parton with a lower transverse momentum is not classified a Jet. Notice that these two definitions naturally help us to avoid two major problems from the outset. First, by defining a region around a hard parton which constitutes a Jet, we naturally avoid situations in which two Jets become collinear, since as they get closer at some point a different Jet that encapsulates both hard partons is formed. Secondly, by defining a low transverse momentum cut, we avoid particles which are too soft within the prediction. In this way we remove both the collinear and soft divergences by avoidance.

There are three commonly used algorithms used to define jets, all with an iterative approach which slowly clusters particles into finalised jets. This is done with the definition of a distance d_{ij} between objects i and j as follows [55]:

$$d_{ij} = \min\left(k_{t\,i}^{2p}, k_{t\,j}^{2p}\right) \frac{\Delta_{ij}^2}{R^2} \tag{1.4.1}$$

$$d_{iB} = k_{t\,i}^{2p} \, , \tag{1.4.2}$$

where $\Delta_{ij}^2 = (y_i - y_j)^2 + (\phi_i - \phi_j)^2$ with y_i and ϕ_i being rapidity and azimuthal angle to be introduced in Section 2.1. The premise is that d_{ij} is calculated for various objects relative to a Jet, until the smallest $d_{ij} < d_{iB}$, at which point the object corresponding to the distance d_{iB} is labelled as a jet. For $p = 1$ one sees the *k_t algorithm*, $p = 0$ is a special case corresponding to the *Cambridge/Aachen algorithm*, and $p = -1$ corresponds to the *Anti-k_t Algorithm*, which favours clusterings that involve hard particles rather than clusterings that involve soft particles [56]. We will be using Anti-k_t algorithm for the rest of this text and in all comparisons.

It is clear; however, that simply discarding particles that do not meet this criteria means we are not getting the full picture. There are regions of phase-space that are simply not being populated, which is a problem when our method of integration requires full coverage. We need a way to transition between the hard process and Jets, which are experimentally observable. This, traditionally comes in the form of a parton shower which evolves the few, high energy, hard partons to multiple, softer partons which hadronise and naturally form Jets.

Parton showers generally achieve this through the use of the *DGLAP Splitting*

Kernels, which simply describe the likelihood of further emissions below some scale, through *Sudakov factors*, the ‘no emission probability’ for any particular state, and traversing a tree of probabilities to integrate over the very large phase-space of possibilities. These Sudakov factors are not unrelated to the previously mentioned Sudakov logarithms, and indeed this process actually includes the terms of the form found in Equation (1.3.20) in a safe way.

So, aside from the clear physical benefits of evolving our model in this fashion, towards the objects which we actually see in detectors, we also get the benefit of including more terms in our model. Further, it is clear to see that in certain regions of phase-space these Sudakov logarithms become very large, and actually spoil the previously assumed perturbative series convergence built around the small strong coupling constant α_s. By noting the negative coefficient of the Mandelstam variable $\hat{s}$ inside of the logarithm, we notice that these will become very large for small values of S, which occurs when the two momenta p_i and p_j which inform it either become soft or collinear these logarithms diverge.

Including these logarithms improves our theoretical predictions, and, if done correctly leads to a *Leading Logarithmic* (LL) accuracy prediction. It is very much worth saying that there are many different logarithms which become very large and spoil the party for fixed-order calculations across various regions of phase-space. In these approaches to improving predictions by including logarithms to *all-orders* one typically has to make some approximations, which hold very true in the regions of phase-space in which they are designed, but do not hold up so well outside of those regions. Thus, it is often prudent to perform a *matching* with a fixed-order calculation to ensure the prediction is never worse than without the inclusion of these logarithms. We will cover how this is achieved in greater detail in Section 2.3.4.

The remainder of this thesis will be devoted to the inclusion of one such logarithm into predictions, and showing that it is indeed important for the description of many different phase-space regions. This is the *High Energy Logarithm*, included by *High Energy Jets* (`HEJ`) in its *all-order* predictions.

Diagram Element	Feynman Rule
External Lines	
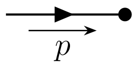	$= u^s(p)$
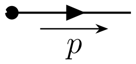	$= \bar{u}^s(p)$
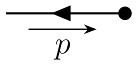	$= \bar{\nu}^s(p)$
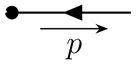	$= v^s(p)$
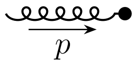	$= \varepsilon_\mu(p)$
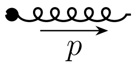	$= \varepsilon^*_\mu(p)$
Internal Lines	
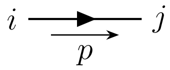	$= \frac{i\delta_{ij}(\not{p}+m)}{p^2-m^2+i\epsilon}$
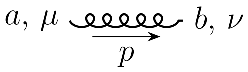	$= \frac{-i\delta^{ab}}{p^2+i\epsilon}\left(g_{\mu\nu} - (1-\xi)\frac{p_\mu p_\nu}{p^2}\right)$
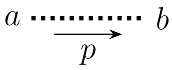	$= \frac{i\delta^{ab}}{p^2}$

Table 1.2: *QCD Feynman rules: External and internal lines [11]*

Diagram Element	Feynman Rule
Vertices	
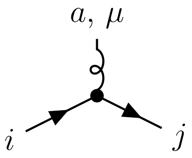	$= ig_s\gamma^\mu T^a_{ij}$
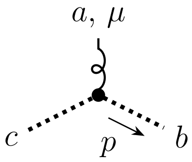	$= -g_s f^{abc} p^\mu$
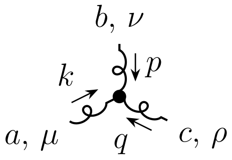	$= \begin{array}{r} g_s f^{abc}[g^{\mu\nu}(k-p)^\rho + \\ g^{\nu\rho}(p-q)^\mu + \\ g^{\rho\mu}(q-k)^\nu] \end{array}$
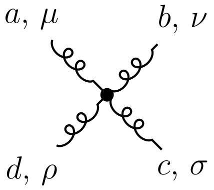	$= \begin{array}{r} -ig_s^2[f^{abe}f^{cde}\,(g^{\mu\sigma}g^{\nu\rho} - g^{\mu\rho}g^{\nu\sigma}) + \\ f^{ace}f^{bde}\,(g^{\mu\nu}g^{\sigma\rho} - g^{\mu\rho}g^{\sigma\nu}) + \\ f^{ade}f^{bce}\,(g^{\mu\nu}g^{\rho\sigma} - g^{\mu\sigma}g^{\rho\nu})] \end{array}$

Table 1.3: *QCD Feynman rules: Vertices [11]*

Diagram Element	Feynman Rule
External Lines	
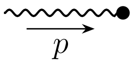	$= \varepsilon(p)$
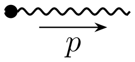	$= \varepsilon^*(p)$
Internal Lines	
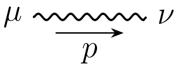	$= \frac{-i\left(g_{\mu\nu}-\frac{p_\mu p_\nu}{m_W^2}\right)}{p^2-m_W^2+i\epsilon}$
Vertices	
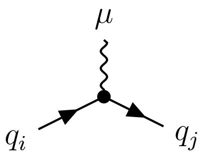	$= -i\frac{g_W}{2\sqrt{2}}\gamma^\mu(1-\gamma^5)V_{ji}$
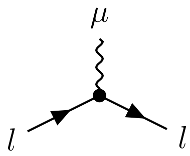	$= -i\frac{g_W}{2\sqrt{2}}\gamma^\mu(1-\gamma^5)$

Table 1.4: *Some W-boson Feynman rules [12]. Note there are other interactions which are possible within the Electroweak sector, but none which are useful for the discussions contained within this text*

CHAPTER

TWO

HIGH ENERGY JETS

One characteristic property of the LHC is that the average multiplicity of events at the collision sites is much higher than at previous colliders [56]. This is in part due to large amounts of pile-up with each bunch crossing, but also the much higher energy of collisions will open up new areas of phase-space in which hard emissions are more likely.

Models which are applied to understand physics on a more fundamental level will never be perfect, but it is clear that there is some tension between current theory and the results from experiments. Even back as far as the 1.96 TeV Tevatron experiment there were consistently a larger number of additional jets present in W-production in association with dijets than expected from purely fixed-order computations [57], at least at NLO. This discrepancy has only been further highlighted at the LHC in multiple analyses showing higher numbers of additional jets in both large dijet invariant mass and also large rapidity separation [58, 59].

Throughout Chapter 1, we built up the necessary tools to be able to make basic predictions for the hard process for collisions at the hadron colliders. We note that this is a very good model for basic predictions, but there are very large uncertainties which exist due to the exclusion of higher-order terms and also areas of phase-space which provide significant contributions. For this chapter we will present the framework and methodology of *High Energy Jets* (`HEJ`), which aims to include one such significant contribution in the *High Energy Limit*.

`HEJ`, is a Monte Carlo generator that aims to describe high multiplicity events at the LHC by including this large logarithm into its predictions. We will discuss the Monte Carlo method in Chapter 3 and some of its implications within the context of High Energy Physics. `HEJ` provides perturbative predictions and maintains leading logarithmic accuracy with its resummation of hard corrections to all orders [60] in the High Energy Limit. This is possible due to the systematic inclusion of the solution to and extension of the BFKL equation [61–64], which describes the tower of logarithms from virtual corrections which we utilise sums to leading logarithmic accuracy (to all orders). These hard corrections although α_S-suppressed, are enhanced by phase-space in large invariant mass scenarios. This means that at higher energy colliders, such as the LHC the exclusive (n+1)-jet rate will be a significant component of the inclusive n-jet rate. The inclusion of the multiple hard perturbative corrections in this manner are in general an improvement on fixed-order and complementary to parton shower formulations [3]. These all-order corrections in the large rapidity separation can then be matched to (currently only) tree level accuracy to ensure at least fixed-order accuracy.

2.1 Framing Discussions

We now introduce some tools which become useful in framing our discussions going forward. We first note that it is clear that any scattering amplitude should be frame independent both experimentally and theoretically. In mathematical formulation this becomes clear as they depend only on covariant quantities such as masses and products of momenta. If we start by considering a generic particle collision experiment, there is a special geometry in which the axis of the incoming beams is uniquely defined. This is typically taken as the z-axis. Even in experiments where the beams do not collide head-on[1], it is possible to get into such a frame via *Lorentz boosts*. Such a set-up allows for very simple descriptions to be made about the system.

A coordinate system can easily be defined where there is a *polar angle* θ with respect to the beam axis, and an *azimuthal angle*, ϕ around the beam axis. This coordinate system, whilst intuitive is not particularly useful since it is frame-dependent and not Lorentz invariant. Fortunately we can define the *rapidity* of a particle as the following:

$$y = \frac{1}{2} \log \frac{p^+}{p^-} \,, \tag{2.1.1}$$

where $p^\pm$ represents the *light-cone momenta*, given by:

$$p^\pm = E \pm p_z \,. \tag{2.1.2}$$

The rapidity of a particle is a particularly useful quantity, since it transforms nicely for boosts along the z-axis:

$$y' = y - \gamma \,, \tag{2.1.3}$$

this linear translational property implies that any differences in rapidity between particles is a Lorentz invariant construct (at least for longitudinal boosts). At this point, we can then parameterise four-momentum as follows:

$$\begin{aligned} p &= (p^+, p^-; \vec{p}_\perp) && (2.1.4) \\ &= (m_\perp e^y, m_\perp e^{-y}; \vec{p}_\perp) \,, && (2.1.5) \end{aligned}$$

where the transverse mass is defined as:

$$m_\perp = \sqrt{m^2 + p_\perp^2} \,, \tag{2.1.6}$$

which is invariant under longitudinal boosts. We can go further than this, and define a set of kinematic variables which can be useful in our calculations going forward

---

[1] such as BaBar

for particular processes. If we consider a basic 2 → 2 scattering process, $(a\,b \rightarrow 1\,2)$ as depicted in Fig. 2.1. There are six possible scalar products of momenta, three of which are distinct:

$$\hat{s} = (p_a + p_b)^2 = (p_1 + p_2)^2 \longrightarrow 4E^2 \tag{2.1.7}$$

$$\hat{t} = (p_a - p_1)^2 = (p_b - p_2)^2 \longrightarrow 2E^2(1 - \cos(\theta)) \tag{2.1.8}$$

$$\hat{u} = (p_a - p_2)^2 = (p_b - p_1)^2 \longrightarrow 2E^2(1 + \cos(\theta))\,, \tag{2.1.9}$$

where $\hat{s}$, $\hat{t}$ and $\hat{u}$ are the *Lorentz invariant Mandelstam Variables*, and the last equivalence in each line is only reached in the centre-of-mass frame. We note here, that as with Eq. (1.3.3), the hat signifies that this is a partonic quantity, there is a another quantity, which specifies the beam centre of mass energy, s, which is related by: $\hat{s} = x_a x_b s$. We have already seen one Mandelstam variable in Eq. (1.3.20). Although there are three of these in a $(2 \rightarrow 2)$ scattering process, there are only two linearly independent variables, since they are constrained by:

$$s + t + u = \sum_i p_i^2 = m_a^2 + m_b^2 + m_1^2 + m_2^2\,. \tag{2.1.10}$$

We can go further than this, and generalise this concept of Lorentz invariant scalar products of momenta for $(2 \rightarrow n)$ scattering processes, and define:

$$s_{ij} = (p_i + p_j)^2 \tag{2.1.11}$$

$$t_{ij} = (p_i - p_j)^2\,. \tag{2.1.12}$$

As before, these invariants are not all independent; for $(2 \rightarrow n)$ scattering there are only $3n - 4$ independent invariants.

2.2 The High Energy Limit

Here we will try to uncover the behaviour of multi-jet cross sections in the limit of large invariant mass. By large, what we require is that it is the largest relative scale within the process such that, for a $(2 \to 2)$, process we have:

$$\hat{s} \gg \hat{t}\,. \tag{2.2.1}$$

This is known as the *Regge limit.* Within this limit there are several interesting and useful equations which one can construct. If we consider the momenta which will be present in this scattering in the form parameterised as in Equation (2.1.4) we see:

$$\begin{aligned}
p_a &= (x_a\sqrt{s},\, 0;\, \vec{0}) && (2.2.2)\\
p_b &= (0,\, x_b\sqrt{s};\, \vec{0}) && (2.2.3)\\
p_1 &= (|\vec{k}_\perp|e^{y_1},\, |\vec{k}_\perp|e^{-y_1};\, \vec{k}_\perp) && (2.2.4)\\
p_2 &= (|\vec{k}_\perp|e^{y_2},\, |\vec{k}_\perp|e^{-y_2};\, -\vec{k}_\perp)\,, && (2.2.5)
\end{aligned}$$

because we set up these parameterisations in a Lorentz invariant way, we can now boost into a frame in which $x_a = x_b$ as well as $y_1 = -y_2 = \frac{\Delta y}{2}$. In this frame we get that the mandelstam variables are given by:

$$\begin{aligned}
\hat{s} &= 2|\vec{k}_\perp|^2(\cosh\Delta y + 1) && (2.2.6)\\
\hat{t} &= -\sqrt{\hat{s}}|\vec{k}_\perp|e^{-\Delta y/2}\,. && (2.2.7)
\end{aligned}$$

If we take the limit of large rapidity separation, $\Delta y \to \infty$, we see that:

$$\begin{aligned}
\hat{s} &= k_\perp^2 e^{\Delta y}\,,\\
\hat{t} &= -k_\perp^2\,,\\
\Delta y &= \log\left(\frac{\hat{s}}{|\hat{t}|}\right)\,, && (2.2.8)
\end{aligned}$$

so we see that large rapidity separation naturally gives us the Regge limit $\hat{s} \gg \hat{t}$ in $(2 \to 2)$ scattering. We can expand this concept to $(2 \to n)$ scattering quite easily.

This corresponds to the *Multi-Regge-Kinematic* (MRK) limit, which calls for strict rapidity ordering and a large rapidity separation between all final state particles which should all have equal transverse momenta:

$$y_1 \gg y_2 \gg \cdots \gg y_i \gg \cdots \gg y_n \qquad |\vec{k}_{i\,\perp}| \approx k_\perp\,. \tag{2.2.9}$$

In this limit we get Mandelstam variables given by: [60]

$$\hat{s} \sim k_{1\,\perp} k_{n\,\perp} e^{y_1 - y_n} \tag{2.2.10}$$

$$\hat{s}_{ij} \sim k_{i\,\perp} k_{j\,\perp} e^{|y_i - y_j|} \tag{2.2.11}$$

$$\hat{t}_{ij} \sim -k_{i\,\perp} k_{j\,\perp} e^{|y_i - y_j|}\,, \tag{2.2.12}$$

we note further that this is equivalent to:

$$\hat{s} \gg \hat{s}_{ij} \sim |\hat{t}_{ij}| \gg k_{i\,\perp}^2\,, \tag{2.2.13}$$

such that we see that the centre-of-mass energy is the largest energy scale to be considered. If we define:

$$q_1 = p_a - p_1, \qquad q_{i+1} = q_i - p_i \qquad t_i = q_i^2\,, \tag{2.2.14}$$

we find that $t_i \sim -k_{i\,\perp}^2$, and therefore:

$$\Delta y_{ij} \equiv |y_i - y_j| \sim \log\left(\frac{\hat{s}_{ij}}{|\hat{t}_i|}\right)\,. \tag{2.2.15}$$

Now we understand the kinematics involved, we are able to calculate the Matrix Element for ($2 \to 2$) scattering for all types of particles scattering. We note here, as we will see shortly, that only the t-channel diagrams are significant in the MRK limit and as such we will only include their contribution.

Further, we omit overall color factors in order to expose the kinematic structure relevant for the MRK discussion. In the MRK limit the color algebra factorises from the kinematics, so the leading behaviour and the rapidity dependence are unchanged by color [3]. Including them here would add clutter without altering our conclusions about t-channel dominance in the MRK limit.

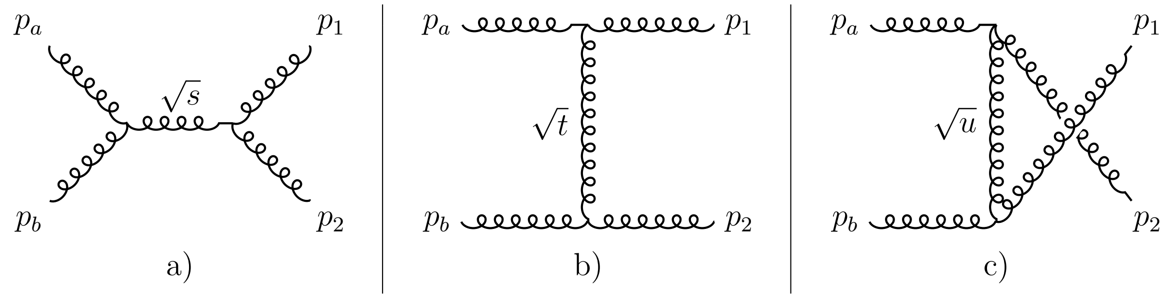

Figure 2.1: *Feynman diagrams for two-to-two gluon scattering process, illustrating the s-channel (a), t-channel (b), and u-channel (c) contributions*

From here, we can easily derive [3]:

$$|\mathcal{M}_{qQ\to qQ}|^2 = |\mathcal{M}_{q\bar{q}'\to q\bar{q}'}|^2 = 16\pi^2\alpha_s^2\left[\frac{4}{9}\frac{\hat{s}^2+\hat{u}^2}{\hat{t}^2}\right] \tag{2.2.16}$$

$$|\mathcal{M}_{q\bar{q}\to q\bar{q}}|^2 = 16\pi^2\alpha_s^2\left[\frac{4}{9}\left(\frac{\hat{s}^2+\hat{u}^2}{\hat{t}^2}+\frac{\hat{t}^2+\hat{u}^2}{\hat{u}^2}\right)-\frac{8}{27}\frac{\hat{u}^2}{\hat{t}\hat{s}}\right] \tag{2.2.17}$$

$$|\mathcal{M}_{qq\to qq}|^2 = 16\pi^2\alpha_s^2\left[\frac{4}{9}\left(\frac{\hat{s}^2+\hat{u}^2}{\hat{t}^2}+\frac{\hat{s}^2+\hat{t}^2}{\hat{u}^2}\right)-\frac{8}{27}\frac{\hat{s}^2}{\hat{t}\hat{u}}\right] \tag{2.2.18}$$

$$|\mathcal{M}_{qg\to qg}|^2 = 16\pi^2\alpha_s^2\left[\frac{\hat{s}^2+\hat{u}^2}{\hat{t}^2}-\frac{4}{9}\frac{\hat{s}^2+\hat{u}^2}{\widehat{su}}\right] \tag{2.2.19}$$

$$|\mathcal{M}_{gg\to gg}|^2 = 16\pi^2\alpha_s^2\left[\frac{9}{2}\left(3-\frac{\hat{t}\hat{u}}{\hat{s}^2}-\frac{\hat{s}\hat{u}}{\hat{t}^2}-\frac{\hat{t}\hat{s}}{\hat{u}^2}\right)\right]. \tag{2.2.20}$$

In the MRK limit, $(\hat{s} \gg \hat{t})$, in which $\hat{s} = -\hat{u}$, these become:

$$|\mathcal{M}_{gg\to gg}|^2 = 16\pi^2\alpha_s^2\frac{9}{2}\frac{\hat{s}^2}{\hat{t}^2} \tag{2.2.21}$$

$$|\mathcal{M}_{qg\to qg}|^2 = \left(\frac{C_F}{C_A}\right)|\mathcal{M}_{gg\to gg}|^2 \tag{2.2.22}$$

$$|\mathcal{M}_{qQ\to qQ}|^2 = |\mathcal{M}_{qq\to qq}|^2 = |\mathcal{M}_{q\bar{q}\to q\bar{q}}|^2 = \left(\frac{C_F}{C_A}\right)^2|\mathcal{M}_{gg\to gg}|^2, \tag{2.2.23}$$

where $C_F = \frac{4}{3}$ and $C_A = 3$. Note then, that all channels are related very simply in the MRK limit, with the only substitution necessary being a change in color factors due to the different interacting particles. Note in particular, that it is simply necessary to multiply by a factor of $\frac{C_F}{C_A}$ for every gluon which is swapped for a quark or anti-quark. We will see in Section 2.3.2 that this can be improved much further, and a statement relating these different channels is possible even away from the MRK limit.

2.2.1 Regge Theory and the MRK Limit

We have seen that we can describe easily scattering of 2 → 2 processes in the Regge limit, and we have the kinematic variables needed to clearly calculate the corresponding 2 → n processes. At this point it would be wise to delve a little into Regge theory, the predictions of which surprisingly hold to be true in fully fledged QCD decades after their proposal. In particular, it predicts in the High Energy Limit the scattering amplitude of a process will scale as the Mandelstam variable $\hat{s}$ raised to the power of the spin of the exchange particle in the t-channel, α:

$$\mathcal{M}_{\text{Regge}} \sim \hat{s}^{\alpha} \, . \tag{2.2.24}$$

This, and many more interesting propositions in Regge theory are contained within various texts [65]. A full discussion of this theory and its implications is well beyond the scope of this text, but we will conclude the above expression can be generalised to a ‘chain’ of exchanged particles in a t-channel configuration, for which the corresponding Matrix Element will scale as:

$$\mathcal{M}_{\text{MRK}} \sim \hat{s}_{12}^{\alpha_1} \hat{s}_{23}^{\alpha_2} \ \ldots \ \hat{s}_{n-1\,n}^{\alpha_{n-1}} \, , \tag{2.2.25}$$

where α_i is the spin of the i^{th} t-channel exchange particle. This, to the reader should signal that the dominant diagrams in any particular scattering amplitude will be through gluon (also referred to as color octet) exchange. We take this moment to note that this has several important ramifications going forward.

Firstly, this defines very nicely for us the kinematics of the dominant contributions in the MRK limit: along with the strict rapidity ordering and separation of final state particles, it will also be necessary that any particles which are ‘central’[1] will be gluons. The external particles will be the same flavor as their corresponding incoming types (except in the case of W-boson emission, as we will discuss later). This configuration was first noted by Fadin, Kuraev and Lipatov [61] to be the

---

[1] that is not external in rapidity

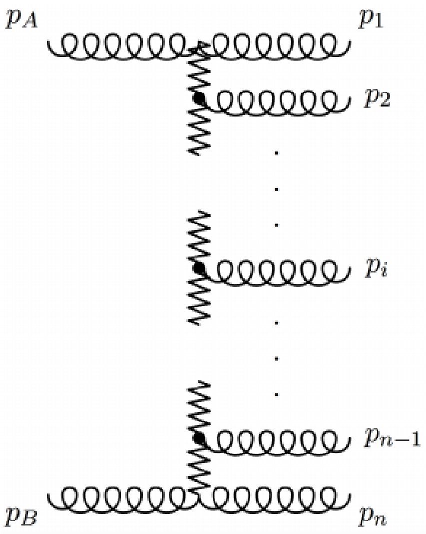

Figure 2.2: *A Schematic representation of an example* $2 \to n$ *gluon scattering amplitude in the MRK limit*

dominant contribution in the MRK limit and are called *FKL Amplitudes*. These are depicted schematically in Fig. 2.7.

Secondly, if the FKL contributions dominate, we gain an insight into what might be the *subleading* contributions. That is, configurations which lead to one of the t-channel exchanges being performed by a spin$-\frac{1}{2}$ particle (either a quark or an anti-quark) will lead to a suppressed contribution. The power which lies in this prediction is not just that we know what contributions this corresponds to, but also the level of suppression we expect in comparison to the dominant FKL amplitudes. We will discuss these subleading contributions much further in Chapter 4.

2.3 HEJ Framework

Within `HEJ`, our goal is to include hard radiative corrections which, while α_s suppressed in comparison to other contributions at any particular order of perturbation theory, they are also enhanced by large logarithms in the large invariant mass limit. To include these large logarithmic corrections, `HEJ` models the Matrix Elements for the hard scattering process using the FKL amplitudes described above, and includes both real emissions, via effective *Lipatov Vertices* and virtual corrections through the use of the *Lipatov ansatz*. We begin with a brief discussion motivating the use of `HEJ`.

2.3.1 Motivation for HEJ

Our motivation for seeking a new approach is due to a major problem with the approach taken in FKL formalism within the MRK limit, and that is apparent if one considers the 2 → 2 process $qQ \to qQ$. The whole result was given by Eq. (2.2.16) and reduces to Eq. (2.2.23) in the MRK limit. The problem is illustrated by considering the Mandelstam variables in the MRK limit actually behave as: $\hat{t} \to -k_\perp^2$ and $\hat{s} \approx -\hat{u} \to \infty$, and as such in the FKL formalism:

$$|\mathcal{M}^{\mathrm{FKL,\,MRK}}_{qQ\to qQ}|^2 = g_s^4 \frac{8}{9} \frac{\hat{s}^2}{(k_\perp^2)^2} \,. \tag{2.3.1}$$

This is problematic, since for the relevant phase-space of the LHC, $\hat{t}$ and $-k_\perp^2$ differ by at least an order of magnitude and the relation $\hat{s} \approx -\hat{u}$ is dubious at best [66].

We can further demonstrate this issue as in [3] by considering three different scattering processes, for $2 \to 2, 3, 4$ parton scattering evaluated at the MRK limit and compared to the leading-order tree level matrix elements. If we consider a slice of phase-space for each of these with fixed transverse momenta ($k_{\perp i}$, and rapidities and azimuthal angles in each respective case as:

1. $y_1 = -y_2 = \Delta;\ \phi_1 = 0;\ \phi_2 = \pi\,,$
2. $y_1 = -y_3 = \Delta;\ y_2 = 0;\ \phi_1 = 0;\ \phi_2 = -\phi_3 = \frac{2\pi}{3}\,,$
3. $y_1 = -y_4 = \Delta;\ y_2 = -y_3 = \frac{\Delta}{3};\ \phi_1 = 0;\ \phi_2 = -\phi_3 = \frac{\pi}{2};\ \phi_4 = \pi\,,$

such that Δ is a simple parameterisation of half of the rapidity separation between the extremal partons in the scattering process. The matrix elements generated by a fixed-order generator are evaluated at different phase-space points on the slice of phase-space in which Δ is incrementally increased are then divided by a flux factor. The results are plotted in Fig. 2.3 we see the problems with just using the MRK result manifest. The MRK limit in all cases is independent of Δ and corresponds to

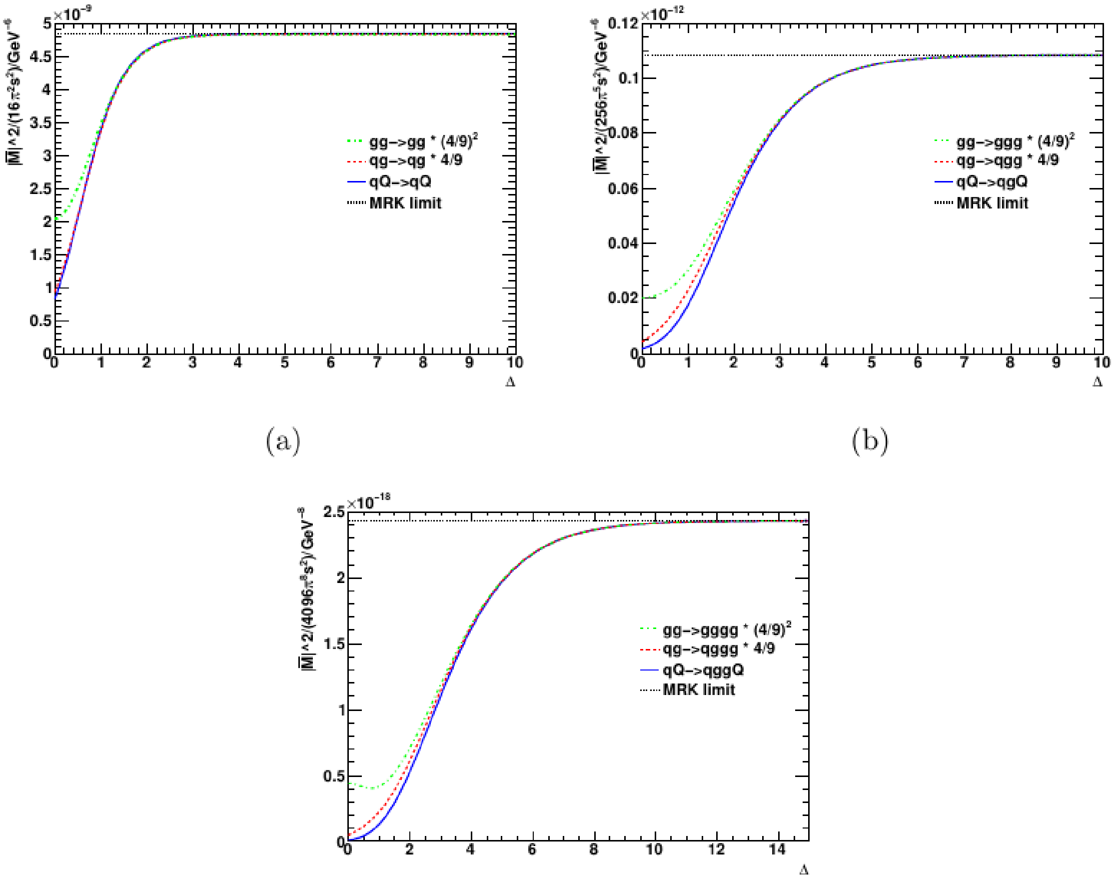

(a) (b)

(c)

Figure 2.3: *The leading-order matrix element squared multiplied by a phase-space factor and a factor of* $\frac{C_F}{C_A}$ *for each of the quarks in the final state is shown for of various different scattering processes. These matrix elements are plotted against a parameter* Δ, *which is half of the rapidity separation between the extremal partons in the final state. The MRK limit is shown as a flat line on all plots, and it is seen as the rapidity span is opened, this limit is reached by the fixed-order matrix elements. Plots reproduced from [3]*

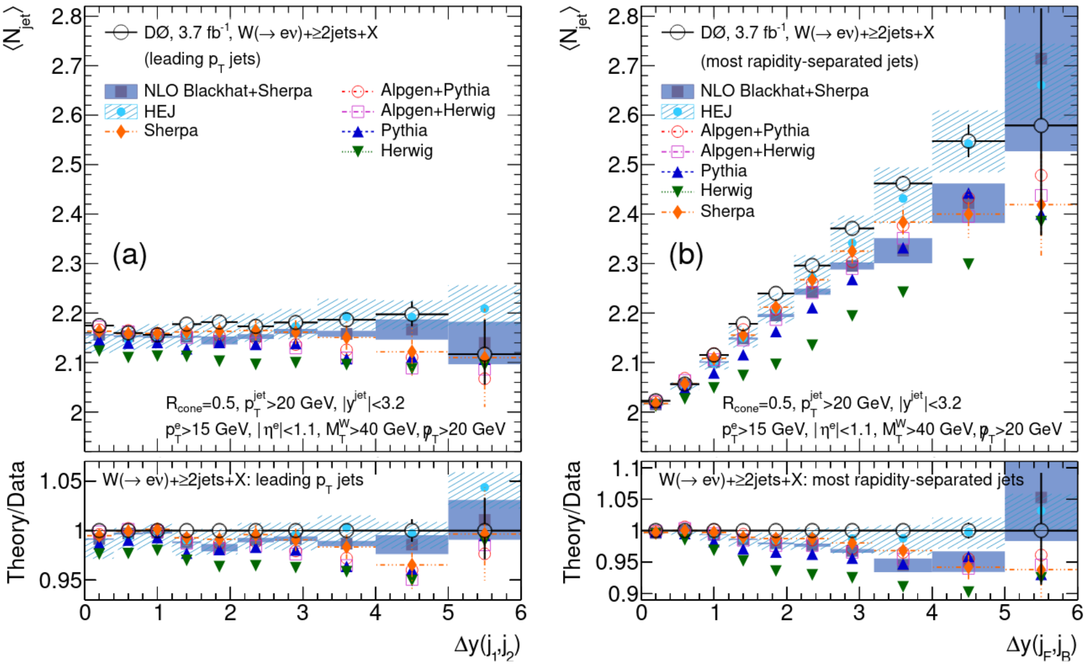

Figure 2.4: *The average number of jets in inclusive W plus dijet production from Tevatron at a centre-of-mass energy* $\sqrt{s} = 1.96$ *TeV as a function of the rapidity separation between two hardest jets,* $\Delta y(j_1, j_2)$ *(left), and rapidity separation between the most forward and backward jets,* $\Delta y(j_f, j_b)$*) (right). [4]*

the flat line in the figure. The leading-order matrix elements approach this value in the MRK limit, but this is as expected at large rapidity separation (between 6 and 16 units of rapidity depending on the process). Unfortunately, at the LHC the main detectors have a *pseudorapidity*[1] coverage significantly lower than this required value for the MRK limit. Specifically, $|\eta| \leq 3.0$ for the CMS detector [67] and $|\eta| \leq 4.9$ for the ATLAS detector [68]. As such, it is clear that for much of the phase-space of the LHC, the MRK result is not valid.

This might seem to be a bad sign for the calculation we are attempting within `HEJ`, since it means that where its approximation is most valid is a very slim area of phase-space. However, as we have alluded, and will demonstrate here that large logarithms play a significant role when these terms are added, and as such the inclusion of such terms which `HEJ` calculates is necessary to achieve leading[2] logarithmic accuracy in

---

[1] The pseudorapidity, η is strictly equivalent to the rapidity (see Eq. (2.1.1)) for massless particles, and is defined as $\eta = -\ln(\tan\theta)$

[2] and, looking to the future, Next-To-Leading

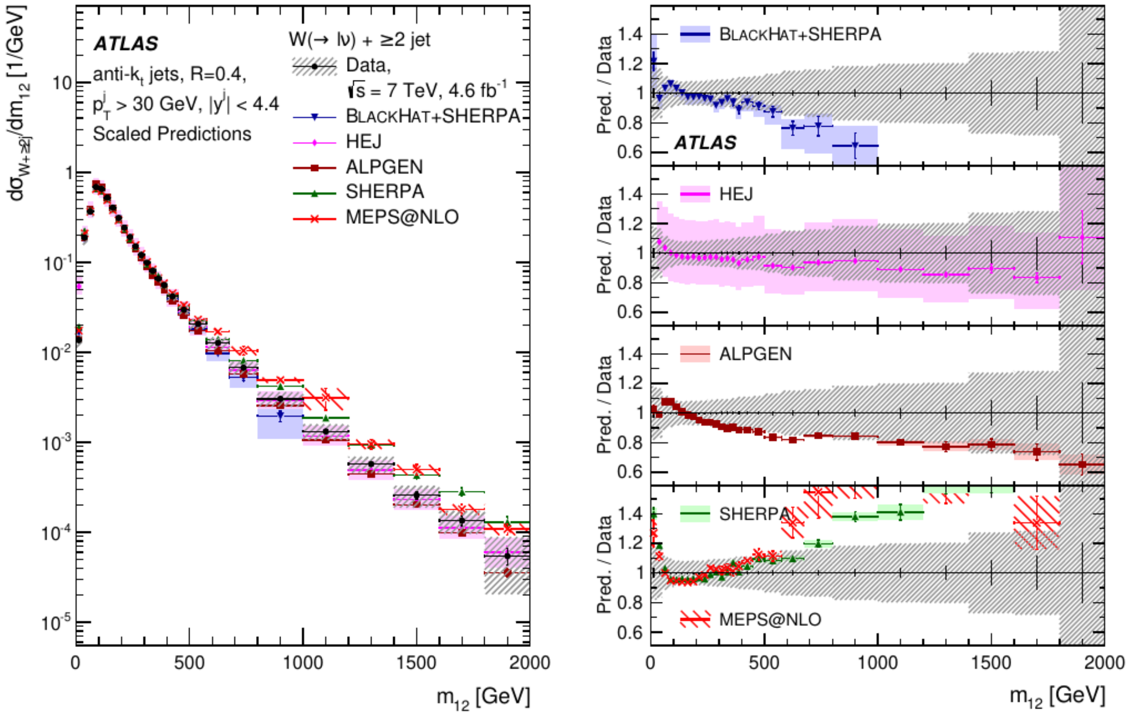

Figure 2.5: *Differential cross-section with respect to the invariant mass between the two hardest jets, Δm_{12} in inclusive W plus dijet production at the ATLAS detector with a center-of-mass energy of $\sqrt{s} = 7$ TeV Plot reproduced from [5]*

the high energy logarithms. An all-order approach such as this is unnecessary for sufficiently inclusive processes; however, for a more exclusive analysis it becomes necessary to consider these large logarithms.

For example, if one considers a jet veto in a rapidity span such as in a *VBF Higgs production* analysis [69], where the major QCD background from gluon fusion production is largely removed. To fully understand these vetoes, it is necessary to have a good description of the exclusive quantities such as the average number of hard jets in a particular rapidity interval for which the all-order approach of `HEJ` will be necessary. We note that there is no other alternative to systematically include these logarithms, since the traditional resummation achieved by parton showers are known to not describe the physics of hard jets [70]. This is due to the fact that rather than resumming high energy logarithms like HEJ, Standard parton showers resum soft/collinear (DGLAP) logarithms under strong k_T or angular ordering and leading color, so the extra jets they generate are typically soft/collinear; they are not systematically accurate for multiple well-separated, high-p_T jets.

To drive this home and finalise our motivation, we will look at a couple of analyses performed by the D0 and ATLAS collaborations respectively. In Fig. 2.4 we see the `HEJ` predictions for average number of jets compared to the data collected at the Tevatron collider at $\sqrt{s} = 1.96$TeV. In the analysis presented in [4] many predictions were made with parton showers matched to LO (`PYTHIA` and `HERWIG`), a parton shower matched to NLO, (`BLACKHAT + SHERPA`) and `HEJ`. Specifically we have the average number of jets as a function of the rapidity separation between two hardest jets, $\Delta(y_1, y_2)$ and the most forward and backward jets $\Delta(y_f, y_b)$.

On the left, we see that the average number of jets is independent of the rapidity separation between the two hardest jets, and on the right, we see that there is a linear correlation between the rapidity separation between the extremal jets and the average number of jets. Notably, `HEJ` provides a good description of data where attempts matched with parton showers fall short and predict fewer jets than data would suggest.

In Fig. 2.5 we have the differential cross-section with respect to the invariant mass between two hardest jets, Δm_{12}, at a centre-of-mass energy of $\sqrt{s} = 7$TeV, as presented in [5]. This compares the predictions of various parton shower merging methods as well as predictions from `HEJ`. In the limit of large Δm_{12} the logarithms included by `HEJ` are significant; hence, the predictions by `HEJ` in this scenario give the best description of this variable.

These analyses present very simply two important points. Firstly, that the predictions produced by `HEJ` include important phase-space enhanced terms in sufficiently high dijet invariant masses and large rapidity separations, which are not predicted well within other prescriptions. Further, it is clear that one does not have to access MRK limit phase-space for these components to become significant, with effects even being seen at the (relatively) small centre-of-mass energy of $\sqrt{s} = 1.96$TeV.

Before delving into the corrections to the HEJ amplitude and their benefits, we first consider the construction of the HEJ amplitude and the necessary approximations for the later inclusion of these corrections. We shall see that the HEJ framework leads to the correct limit of N-jet amplitudes but also goes beyond the FKL formalism's description of the leading logarithmic accuracy [66].

2.3.2 HEJ Amplitudes

We want to improve the basic fixed-order prediction, but we also want to improve on the MRK limit predictions for these corrections which are phase-space enhanced. So, if we want to improve this approximation from the BFKL formalism, we need to look in a little more detail at the scattering process, and evaluate all terms in Equation (2.2.16) separately and include all of their effects rather than homogenising them as would be done (and valid in) the MRK limit.

We use *spinor helicity* notation for the quark currents where we have $j_{a1}^{-\,\mu} = \bar{u}_1^{-}\gamma^\mu u_a^{-}$ is written as $\langle 1|\mu|a\rangle$ we can write the amplitude in the color- and coupling-stripped form:

$$\mathcal{M}_{q^-Q^-\to q^-Q^-} = \langle 1|\mu|a\rangle \frac{g^{\mu\nu}}{\hat{t}} \langle 2|\nu|b\rangle\,. \tag{2.3.2}$$

If we go further we can define a *spinor string*, the contraction of these two currents, as:

$$S_{qQ\to qQ}^{h_a h_b\to h_1 h_2} = \langle 1\ h_1|\mu|a\ h_a\rangle g^{\mu\nu} \langle 2\ h_2|\nu|b\ h_b\rangle\,, \tag{2.3.3}$$

and we denote the sum of helicities over the square of this by the more compact notation:

$$||S_{qQ\to qQ}||^2 = \sum_{h_a,h_1,h_b,h_2} |S_{qQ\to qQ}^{h_a h_b\to h_1 h_2}|^2\,, \tag{2.3.4}$$

and therefore we can write the full color and helicity summed matrix element for this process as:

$$|\bar{\mathcal{M}}_{qQ\to qQ}|^2 = \frac{16\pi^2\alpha_s^2 C_F^2}{4(N_C^2-1)} \frac{||S_{qQ\to qQ}||^2}{\hat{t}^2}\,. \tag{2.3.5}$$

We have noted in Section 2.2 that there is a simple relation in the MRK limit which allows one to translate between the results of different channels of 2 → 2 scattering processes by a simple factor of $\frac{C_F}{C_A}$ for each quark swapped to a gluon involved in the process. However, it is clear that under the treatment above, it is possible to expose the true power of the `HEJ` formalism at this point, and that is that one can write the $qg \to qg$ scattering process in the following form [60]:

$$\mathcal{M}_{q^-g^+\to q^-g^+} = -i4\pi^2\alpha_s \frac{p^*_{2\perp}}{|p_{2\perp}|}\left(t^2_{ea}t^b_{1e}\sqrt{\frac{p_b^-}{p_2^-}} - t^b_{ea}t^2_{1e}\sqrt{\frac{p_2^-}{p_b^-}}\right)\frac{S^{-+\to-+}_{qg\to qg}}{\hat{t}}\,, \tag{2.3.6}$$

this leads to the very surprising result that the color-summed and averaged matrix element for this process can be written as:

$$|\bar{\mathcal{M}}_{q^-g^+\to q^-g^+}|^2 = \frac{16\pi^2\alpha_s^2 C_F}{4(N_C^2-1)}\left(\frac{\tilde{C}_A}{C_F}\right)\frac{||S^{-+\to-+}_{qg\to qg}||^2}{\hat{t}^2}\,, \tag{2.3.7}$$

where we have utilised the momentum-dependent color factor, $\tilde{C}_A$, termed a *color acceleration multiplier* (CAM) factor, given by:

$$\tilde{C}_A = \frac{1}{2}\left(C_A - \frac{1}{C_A}\right)\left(\frac{p_b^-}{p_2^-} + \frac{p_2^-}{p_b^-}\right)\,, \tag{2.3.8}$$

where it is then clear that in the limit $p_2^- \sim p_b^-$, $\tilde{C}_A \to C_A$, and thus we recover our factor previously stated factor in the MRK limit in Eq. (2.2.22). Eq. (2.3.8) expresses how the strength of the current increases with increasing acceleration of the scattering gluon. Motivation and derivation of this can be found in [60]. There is a similar factor corresponding to quark/gluon swapping in the forwards direction, which is given in the cited text, and can be found in alternate forms in [66]. From this point forward, these CAM factors are used in replacement of C_A where appropriate to better describe the color factors in the cases of different channels for the same diagrams. Note that this swap is an exact result, valid for all approximations within `HEJ`, which is a significant finding.

So far we have still assumed non-identical quarks in the initial state, aside from swapping a quark for a gluon through use of this effective color factor. For the case of swapping the non-identical quarks for gluons it is necessary to divide by an extra symmetry factor of 2.

To consider the impact of swapping our quarks for anti-quarks we begin by noting the following relations:

$$P_L\nu(p) = \nu_+(p) = |p^-\rangle \tag{2.3.9}$$

$$\langle i^-|\mu|j^-\rangle = \langle j^+|\mu|i^+\rangle \,. \tag{2.3.10}$$

As such, we know that if we replace quarks with anti-quarks on a simple extremal current in `HEJ`, we only need to replace:

$$\langle 2^\pm|\mu|b^\pm\rangle \to \langle 2^\mp|\mu|b^\mp\rangle \,, \tag{2.3.11}$$

which in the `HEJ` formalism is inconsequential, since we perform a sum over helicities and as such the end result of the total summed matrix element squared is unchanged. As such, we can swap between any channel of the same process effortlessly.

It must be stressed, that the main power of this result is not the simple relation between different channels, but it lies within the form. There is an explicit t-channel factorisation and there is no pole in the s- or u-channels. This, remarkably, is true for all helicity assignments for which the gluon does not flip helicity under the scattering. It is notable to mention at this point that any amplitude corresponding to a scattering under which the gluon flips helicity is suppressed by a factor of $\hat{s}$. In fact, s and u channel poles only exist for scatterings in which the quark and incoming gluon have the same helicity assignment, *and* the gluon helicity is flipped [66].

It is apparent then, that the quark scattering calculation we performed above, all contributions from $qQ \to qQ$ and the dominant contributions from $qg \to qg$ and even half of the contributions for $gg \to gg$ can be described in full by only varying color factors. If we continue down this train of thought, and consider $gg \to gg$ scattering, one sees once again this t-channel factorisation in scatterings in which the gluons have opposite helicities [66]. This is an important result, and will lead into the systematic improvements made within `HEJ`. These systematic improvements enable the inclusion of higher-order corrections within the perturbative series which are enhanced by large logarithms in the high energy limit. These are hard, radiative corrections accompanied by virtual corrections to all orders. We will begin with a discussion on the addition of real corrections within the `HEJ` formalism.

2.3.3 Real Emission Corrections

We discussed in Section 2.2.1 that the configuration of the dominant amplitudes is such that any quarks in the final state are the extremal particles in rapidity. Thus, any single *real emission* will be the radiation of a gluon within the rapidity span between the two external legs, since any quark production must also have an anti-quark pair and will therefore be two extra particles, and lead to a t-channel quark propagator and thus a suppression, according to Regge theory, of $\hat{s}_{q\bar{q}}$.

For $(2 \to n)$ scattering we can use some results from multi-Regge theory. We know that in the MRK limit for every gluon emitted after the first two, there is an extra factor which is just the MRK limit of the Lipatov vertices [7]:

$$\frac{4g_s^2\mathcal{C}_A}{k_{i\perp}^2}\,. \tag{2.3.12}$$

For example, the MRK limit of the color and spin summed and averaged matrix element for $gg \to gg$ is

$$\left|\mathcal{M}^{\bar{M}RK}_{gg\to gg}\right|^2 \to \frac{4\hat{s}^2}{\left(N_c^2-1\right)}\,\frac{g_s^2\mathcal{C}_A}{k_{1\perp}^2}\,\frac{g_s^2\mathcal{C}_A}{k_{2\perp}^2}\,. \tag{2.3.13}$$

Further, the MRK limit for the $gg \to ggg$ process is:

$$\left|\mathcal{M}^{\bar{M}RK}_{gg\to ggg}\right|^2 \to \frac{4g_s^2\mathcal{C}_A}{k_{i\perp}^2}\left|\mathcal{M}^{\bar{M}RK}_{gg\to gg}\right|^2 = \frac{4\hat{s}^2}{\left(N_c^2-1\right)}\,\frac{g_s^2\mathcal{C}_A}{k_{1\perp}^2}\,\frac{4g_s^2\mathcal{C}_A}{k_{2\perp}^2}\,\frac{g_s^2\mathcal{C}_A}{k_{3\perp}^2}\,. \tag{2.3.14}$$

This is a nice result, but it is only valid in the MRK limit, which as we have already discussed is an ambitious target area of phase-space for the LHC to reach. This is an encouraging development; however, since it suggests that it is possible to factorise the addition of an extra gluon to the process into a simple factor, allowing us to simply state these phase-space enhanced emissions.

Instead, let us build a more flexible description of these emissions and check we get this result in the correct limit. We begin with the emission of a gluon from qQ scattering, and build a description of $qQ \to qgQ$. We immediately note that the extra gluon is constrained to be within the rapidity span of the two final state quarks, but that it could be emitted from any leg of the born level $qQ \to qQ$ scattering diagram. This is indicated in Fig. 2.6.

As one would expect, the addition of an extra particle into the diagram leads to one needing to consider many more diagrams (or, terms in the perturbative series) to form the final result. However, we can distil all of these extra diagrams into one and include this real emission in the form of an effective *Lipatov Vertex* [3]. Note, that this means we can calculate the dominant higher-order real emissions in this area of phase-space very efficiently and accurately, since we are not only selective[1] in the terms we include, but also we calculate many at the same time.

Now, let us construct this effective vertex by calculating the impact of each of the diagrams from which it is composed; for the extra emission from the t-channel propagator we get a contribution [3]:

$$\begin{aligned}\mathcal{A}_g = \frac{-\mathcal{C}_g g_s^3}{t_1 t_2}\ \bar{u}(p_1)\gamma_\mu u(p_A)\ \bar{u}(p_3)\gamma_\nu u(p_B) \,*\\ \varepsilon_\rho^* \left((q_1+q_2)^\rho g^{\mu\nu} + (p_2-q_2)^\mu g^{\nu\rho} - (q_1+p_2)^\nu g^{\mu\rho}\right)\ ,\end{aligned} \tag{2.3.15}$$

where $\mathcal{C}_g = T^w_{a_1 a_A} f^{w i_2 v} T^v_{a_3 a_B}$. This is depicted in Fig. 2.6b. If we consider the MRK Limit we have the relations $q_1 = p_3 - p_B + p_2$ and $q_2 = p_A - p_1 - p_2$ and as such Eq. (2.3.15) can be rewritten as:

$$\mathcal{A}_g^{\mathrm{MRK}} = \frac{-2 g_s^3 \hat{s}}{t_1 t_2}\ \varepsilon_\rho^* \left(-2p_A^\rho \frac{s_{2B}}{\hat{s}} + 2p_B^\rho \frac{s_{2A}}{\hat{s}} + (q_1+q_2)^\rho\right)\ . \tag{2.3.16}$$

Next we consider the contributions where the gluon is emitted from any of the external quark legs as in Fig. 2.6a.

The eikonal approximation simplifies calculations in the high-energy limit by assuming that the momentum of the emitted gluon is small compared to the momenta of

---

[1] Justifiably

the external particles. This results in a factorization of the scattering amplitude, where gluon emissions from external legs are proportional to their momenta divided by the eikonal denominator $p_i \cdot p_2$ [3]. This approximation captures the dominant behavior of soft and collinear emissions. Additionally, it highlights the coherent nature of gluon radiation, where interference effects between emission sources are governed by the color structure and contribute to the overall amplitude.

We note here that we are using the Eikonal approximation, which, in this context enables the decomposition of the gluon emission contributions in Eq. (2.3.17) into a sum over individual sources, each weighted by its respective color factor, $\mathcal{C}_i$. This simplifies the treatment of the MRK limit. The four diagrams corresponding to this contribution sum up to yield [3]:

$$\mathcal{A}_q = \mathcal{A}_{qQ\to qQ} \times (ig_s)\; \varepsilon^*_\rho \left(\mathcal{C}_1 \frac{p_1^\rho}{p_1 \cdot p_2} - \mathcal{C}_A \frac{p_A^\rho}{p_A \cdot p_2} + \mathcal{C}_3 \frac{p_3^\rho}{p_3 \cdot p_2} - \mathcal{C}_B \frac{p_B^\rho}{p_B \cdot p_2} \right), \tag{2.3.17}$$

where $\mathcal{C}_i$ are the relevant color factors for each interaction:

$$\mathcal{C}_1 = T^{i_2}_{a_1 b} T^{w}_{b a_A} T^{w}_{a_3 a_B}\,, \tag{2.3.18}$$

$$\mathcal{C}_A = T^{w}_{a_1 b} T^{i_2}_{b a_A} T^{w}_{a_3 a_B}\,, \tag{2.3.19}$$

$$\mathcal{C}_3 = T^{w}_{a_1 a_A} T^{i_2}_{a_3 b} T^{w}_{b a_B}\,, \tag{2.3.20}$$

$$\mathcal{C}_B = T^{w}_{a_1 a_A} T^{w}_{a_3 b} T^{i_2}_{b a_B}\,. \tag{2.3.21}$$

We are performing this calculation, and then imposing the MRK limit, and thus: $p_A \to p_1$, $p_B \to p_3$ and $\mathcal{A}_{qQ\to qQ} = S_{qQ\to qQ}/t$, so

$$\mathcal{A}_q^{MRK} \to \frac{S_{qQ\to qQ}}{q_1^2 q_2^2} \left(-i g_s^3\right) \varepsilon^*_\rho \left(\left(\mathcal{C}_1 - \mathcal{C}_A\right) q_1^2 \;\frac{p_A^\rho}{p_A \cdot p_2} + \left(\mathcal{C}_3 - \mathcal{C}_B\right) q_2^2 \;\frac{p_B^\rho}{p_B \cdot p_2} \right). \tag{2.3.22}$$

We note of course that $(\mathcal{C}_1 - \mathcal{C}_A) = i\mathcal{C}_g$ and $(\mathcal{C}_3 - \mathcal{C}_B) = -i\mathcal{C}_g$ therefore, we have the same color factor for all 5 contributing diagrams (despite the complexity). This similar color factor allows us to sum Eqs. (2.3.16) and (2.3.22) and arrive at the following result [3]:

$$\mathcal{A}^{MRK}_{qQ\to qgQ} = \mathcal{A}_g^{MRK} + \mathcal{A}_q^{MRK} = g_s^3\; \mathcal{C}_g\; \varepsilon^*_\rho\; \frac{S_{qQ\to qQ}}{q_1^2 q_2^2}\; V^\rho(q_1, q_2)\,, \tag{2.3.23}$$

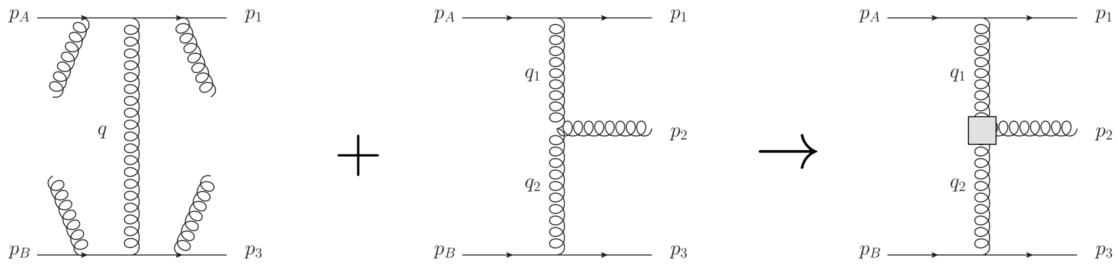

(a) External Legs **(b)** 3-Gluon Vertex **(c)** Lipatov Vertex

Figure 2.6: *This Figure illustrates how the Lipatov Vertex contains within it contributions from all possible gluon emission sites.*

where

$$\begin{aligned} V^\rho(q_i, q_{i+1}) = &- (q_i + q_{i+1})^\rho \\ &+ \frac{p_a^\rho}{2}\left(\frac{q_i^2}{p_{i+1}\cdot p_a} + \frac{p_{i+1}\cdot p_b}{p_a\cdot p_b} + \frac{p_{i+1}\cdot p_3}{p_a\cdot p_3}\right) + p_a \leftrightarrow p_i \\ &- \frac{p_b^\rho}{2}\left(\frac{q_{i+1}^2}{p_{i+1}\cdot p_b} + \frac{p_{i+1}\cdot p_a}{p_b\cdot p_a} + \frac{p_{i+1}\cdot p_i}{p_b\cdot p_i}\right) - p_b \leftrightarrow p_n \,. \end{aligned} \tag{2.3.24}$$

is an effective vertex referred to as a Lipatov Vertex which is represented by a grey square vertex in Fig. 2.6c corresponding to the amplitude in Eq. (2.3.23). In Fig. 2.6, we follow the process laid out above. We can see then, that the process of an extra gluon emission in the MRK Limit can be treated as the emission of a gluon from an effective Lipatov vertex established in the t-channel gluon propagator. We can then, write a general form for the process $qQ \to qg\ldots gQ$ with $n-2$ final state gluons where the quarks are extremal in rapidity as:

$$\begin{aligned} |\bar{\mathcal{M}}_{qQ\to qg\ldots gQ}|^2 = &\frac{1}{4\left(N_C^2-1\right)}||S_{qQ\to qQ}||^2 \\ &\cdot \left(g_s^2 C_F \frac{1}{\hat{t}_1}\right)\cdot\left(g_s^2 C_F \frac{1}{\hat{t}_{n-1}}\right) \\ &\cdot \prod_{i=1}^{n-2}\left(\frac{-g_s^2 C_A}{\hat{t}_i \hat{t}_{i+1}} V^\mu\left(q_i,\, q_{i+1}\right) V_\mu\left(q_i,\, q_{i+1}\right)\right) \,. \end{aligned} \tag{2.3.25}$$

To generalize this further, we apply the Color Acceleration Multiplier (CAM) factors from Eq. (2.3.8), extending the expression to all incoming particle types. This representation concludes the possible real emissions in Fadin-Kuraev-Lipatov (FKL) amplitudes. However, these real emissions include an infrared divergence, as discussed in

Section 1.3.2, which must be canceled by the corresponding virtual corrections.

In `HEJ`, these cancellations are incorporated through the Lipatov Ansatz, a crucial element of the formalism that embeds the high-energy behavior of QCD into the amplitude. The Lipatov Ansatz originates from the BFKL formalism [3, 71, 72], which resums logarithmic corrections proportional to $\alpha_s \ln(s)$. It assumes a modification of propagators in the t-channel to account for the resummation of gluon exchanges:

$$\frac{1}{t_i} \to \frac{1}{t_i} \exp[\hat{\alpha}(q_i)(y_{i-1} - y_i)]\,, \tag{2.3.26}$$

where

$$\hat{\alpha} = -g^2 C_A \frac{\Gamma(1-\varepsilon)}{(4\pi)^{2+\varepsilon}} \frac{2}{\varepsilon} \left(\frac{q^2}{\mu^2}\right)^{\varepsilon}, \tag{2.3.27}$$

is the Regge Trajectory [3] encapsulating the all-order corrections from gluon exchanges between scattering particles. This Ansatz allows for the consistent inclusion of higher-order corrections, bridging the gap between fixed-order calculations and all-order resummations, as required by the `HEJ` framework. The exponential factor encapsulates the dependence of gluon interactions on rapidity separation, ensuring that the amplitude remains infrared finite by balancing divergences between real and virtual emissions. The transition to an all-order α_s treatment is a defining feature of `HEJ`, distinguishing it from traditional fixed-order calculations.

At this point, we are then able to apply the Lipatov Ansatz, Eq. (2.3.26) to obtain a full expression reproducing the leading logarithmic terms to all orders in coupling:

$$\begin{aligned}|\overline{\mathcal{M}_{f_1 f_2 \to f_1 g \cdots g f_2}}|^2 =& \frac{1}{4\left(N_C^2 - 1\right)} ||S_{qQ\to qQ}||^2 \\ &\cdot \left(g_s^2 K_{f_1} \frac{1}{\hat{t}_1}\right) \cdot \left(g_s^2 K_{f_n} \frac{1}{\hat{t}_{n-1}}\right) \\ &\cdot \prod_{i=1}^{n-2} \left(\frac{-g_s^2 C_A}{\hat{t}_i \hat{t}_{i+1}} V^{\mu}\left(q_i,\, q_{i+1}\right) V_{\mu}\left(q_i,\, q_{i+1}\right)\right) \\ &\cdot \prod_{j=1}^{n-1} \exp\left[\hat{\alpha}\left(q_i\right)\left(y_{i-1} - y_i\right)\right]\,,\end{aligned} \tag{2.3.28}$$

where $K_q = K_{\bar{q}} = C_F$, and $K_g = \tilde{C}_A$. This virtual correction cancels the pole from the real emission exactly, as we require. We can see this behaviour by considering the extremal partons in the final state of the $(qQ \to qgQ)$ process to be 'hard' while others are then considered to be radiative corrections, then the phase-space integration of the middle parton will give a factor [7]:

$$\int \frac{\mathrm{d}^2 k_{2\perp}}{(2\pi)^2} \int_{y_1}^{y_3} \frac{dy_2}{4\pi} \frac{4 g_s^2 \mathcal{C}_A}{k_{2\perp}^2} = \frac{\Delta y_{31}}{4\pi} \int \frac{\mathrm{d}^2 k_{2\perp}}{(2\pi)^2} \frac{4 g_s^2 \mathcal{C}_A}{k_{2\perp}^2} = 4 \; \Delta y_{31} \; \alpha_s \; \mathcal{C}_A \; \int \frac{\mathrm{d}^2 k_{2\perp}}{(2\pi)^2} \frac{1}{k_{2\perp}^2} \,, \tag{2.3.29}$$

where $\Delta y_{ij} = (y_i - y_j)$. We see in Eq. (2.3.29) that the real emission of a parton introduces a dependence on the rapidity difference of the two extremal partons. This integral exhibits an IR divergence; however, it adheres to the KLN theorem and the divergence cancels with the divergence of the virtual corrections of the $(2 \to 2)$ process. It then logically follows (since Δy_{31} is an overall factor in Eq. (2.3.29)) that the virtual corrections will also produce a dependence on this rapidity difference. In the MRK limit, $\log \hat{s}/\hat{t} \to \Delta y_{31}$ [7], so we have included logarithmic corrections to the perturbative series. Although presented for a single real emission, this result holds for all orders of α_s, as is presented in [66].

The result is a set of amplitudes in the form depicted by Fig. 2.7.

These FKL amplitudes dominate the phase-space under Multi-Regge Kinematics (MRK) by resumming the leading logarithms in s/t. Although these amplitudes represent only a subset of the total phase-space, they capture the dominant contributions in the high-energy limit. As shown in Eq. (2.3.29), the logarithmic dependence on rapidity differences (Δy_{31}) arises from real emission corrections, with divergences canceled by virtual corrections [60].

However, the FKL framework, being limited to leading power in s/t, becomes less accurate outside MRK. Two main strategies address this limitation:

1. **Inclusion of Subleading Terms:** Extending the formalism to account for subleading contributions in s/t broadens its applicability and which improves the description of processes with smaller rapidity separations [3].
2. **Matching to Fixed-Order Predictions:** Combining resummed predictions

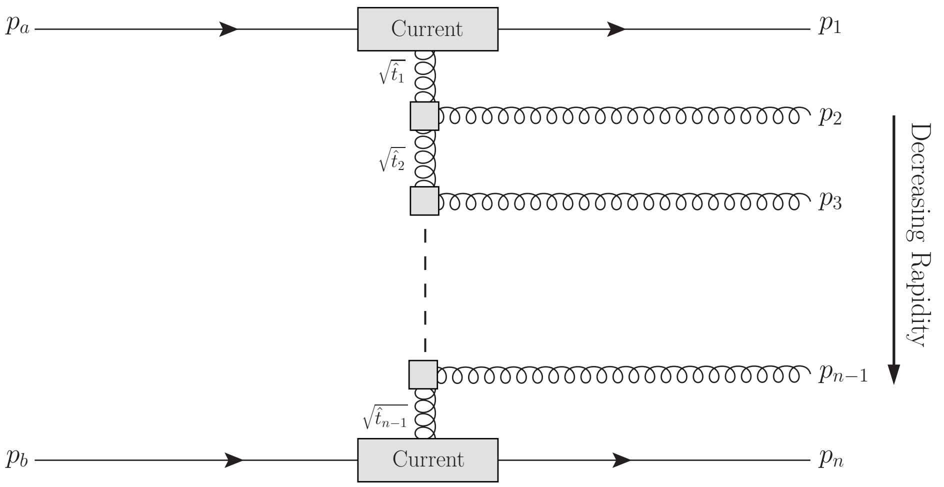

Figure 2.7: *This is an example FKL Amplitude. Notice in particular the rapidity ordering with the quarks at the extremal limits.*

with fixed-order QCD ensures accuracy across all kinematic regimes, seamlessly transitioning between logarithmic and fixed-order regions [7].

These improvements enhance the robustness of `HEJ`, allowing it to describe high-energy scattering processes with an accuracy well beyond the strict MRK limit. We will now discuss the concept of matching before covering the subleading terms in Chapter 4.

2.3.4 Matching

Since the approximation made towards the Matrix Elements within `HEJ` will be inaccurate away from the high energy limit, it is best to reweight the matrix element prediction with the result of a leading (Fixed) order calculation of the result, such that the overall accuracy is never worse than the prediction from the most naive perturbative calculation. The reweighting methodology has evolved in recent years. Up until the release of `HEJ2` [73], this was achieved by clustering the final state of a generated event into jets and figuring out what born level process this equated to. This was achieved by reshuffling transverse momenta in such a way that jet rapidities remained fixed throughout this reclustering process, and as such the `HEJ` event classification would never be altered. Subsequently, the fixed-order matrix element prediction was computed with the use of standalone MadGraph code [74], which was then used to reweight the `HEJ` prediction as:

$$w_{m-\text{jet}} = \frac{\overline{|\mathcal{M}_{\text{LO}}^{\text{MG}}\left(\left\{p_{\mathcal{J}}^{\mathcal{B}}\left(p_i\right)\right\}\right)|^2}}{\overline{|\mathcal{M}_{\text{tree}}^{\text{HEJ}}\left(\left\{p_{\mathcal{J}}^{\mathcal{B}}\left(p_i\right)\right\}\right)|^2}}\,. \tag{2.3.30}$$

As of `HEJ2`, fixed-order events are read in as input, and this clustering step is no longer necessary, since we already know the process at hand upon reading the event in. We simply calculate the `HEJ` prediction for the born level process and reweight it using Eq. (2.3.30). This reweighting means that our `HEJ` cross-section[1] prediction for the processes under the logarithmic control of the `HEJ` resummation at a fully inclusive level is obtained as follows:

$$\begin{aligned}\sigma_{Nj}^{\text{resum,match}} =& \sum_{f_1,f_2}\sum_{n=2}^{\infty}\mathbf{T}_y\prod_{i=1}^{n}\left(\int_{p_{i\perp}=\lambda}^{p_{i\perp}=\infty}\frac{\mathrm{d}^2\mathbf{p}_{i\perp}}{(2\pi)^3}\int\frac{\mathrm{d}y_i}{2}\right)\frac{\overline{|\mathcal{M}_{\text{HEJ}}^{f_1f_2\to f_1g\cdots gf_2}\left(\left\{p_{\mathcal{J}}^{\mathcal{B}}\left(p_i\right)\right\}\right)|}^2}{\hat{s}^2}\\ &\times\sum_{m\geq N}\mathcal{O}_{mj}^{e}(\{p_i\})\;w_{m-\text{jet}} \qquad\qquad (2.3.31)\\ &\times\;x_Af_{A,f_1}(x_A,Q_A)\;x_Bf_{B,f_2}(x_B,Q_b)\;(2\pi)^4\;\delta^2\!\left(\sum_{i=1}^{n}\mathbf{p}_{i\perp}\right)\;\mathcal{O}_{2j}(\{p_i\})\,,\end{aligned}$$

where $\mathcal{O}_{mj}^{e}(\{p_i\})$ is the exclusive m-jet measure applied to each n-parton kinematic point of the resummation event. This quantity equals unity for exactly m-jets and zero otherwise. $\mathbf{T}_y$ indicates rapidity ordering.

Further, there are contributions which are not calculated within the framework of `HEJ`, these processes, referred to within `HEJ` as *non-resummable* events, are included within the `HEJ` prediction by simply including them in the overall cross-section prediction without performing any resummation on them. This allows us to recover the full LO accuracy away from the limit. This leads us to the statement that the fully inclusive `HEJ` cross-section is given by:

$$\sigma_{Nj}^{\texttt{HEJ}} = \sigma_{Nj}^{\text{resum,match}} + \sum_{m\geq N}\sigma_{mj}^{\text{non-resummable}}\,, \tag{2.3.32}$$

where $\sigma_{mj}^{\text{non-resummable}}$ are the exclusive leading order cross-sections for m-jets corresponding to all channels which do not exist within the `HEJ` formulation. Up until

---

[1] as well as all kinematic distributions

this point we have only discussed that the leading contribution in the MRK limit corresponds to FKL amplitudes. A significant portion of the work presented in this thesis has been to reduce the number of significant channels of processes which are included in this manner, thereby reducing the direct dependence on fixed-order calculations within our predictions and bringing more of the cross-section under logarithmic control. The multiplicity of the matching and inclusion of non-resummable processes is limited by the generation of fixed order event samples. Since leading-order input is used, this is theoretically possible for any number of jets; however, there are considerations including RAM usage, which limit our jet multiplicities in the fixed-order input even generation.

Before delving into these *subleading* corrections to the `HEJ` prediction we will look at one further nicety of the `HEJ` formalism which directly results from the current scattering nature of the calculation.

2.4 W+Jets in HEJ

`HEJ` formalism is centred around the idea of current scattering. This is intuitive when considering the high energy limit, since one leg of the diagram is unlikely to significantly interact with the opposite leg separated from it by many units of rapidity. This is only an approximation, which is why we use matching. However, in addition to enabling the resummation of high-energy logarithms as we have discussed in Section 2.3.1, this factorisation of the process into currents which can be contracted gives us a very nice property. Namely, we can calculate new processes with relative ease. If we have a purely QCD process, for example $ud \to ud$, we can consider an analogous W+Jets process, $ud \to d\nu_l \bar{l} d$, by simply taking a W emission as an electroweak correction to the pure jet process current factor by the inclusion of:

$$||S_{ud\to d\nu_l\bar{l}d}||^2 = \frac{g_W^2}{4}\left|\frac{1}{(p_l+p_{\bar{l}})^2 - m_W^2 + i\Gamma_W m_W}\right| \sum_{h_b,h_2} |S^{-h_b\to -h_2}_{ud\to d\nu_l\bar{l}d}|^2\,, \qquad (2.4.1)$$

where m_W is the W-boson mass, Γ_W is the decay width and g_W is the weak coupling strength, and we defined:

$$S^{-h_b \to -h_2}_{ud \to d\nu_l \bar{l} d} = j^{-}_{W\mu} \frac{g^{\mu\nu}}{\hat{t}} \langle 2^{h_2} | \nu | b^{h_b} \rangle \,. \tag{2.4.2}$$

So, we can see, apart from several correction factors, we have changed from a QCD process to a W+Jets process, by simply swapping out one of the currents for a quark current which emits a W-boson. In this case, Fig. 2.8 visually demonstrates what different contributions go into this effective current and mathematically, this is given by:

$$j^{\mu}_{W}(p_a, p_l, p_{\bar{l}}, p_1) = \langle 1^- | \left(\frac{\gamma^{\nu} (\not{p}_l + \not{p}_{\bar{l}} + \not{p}_1) \gamma^{\mu}}{(p_l + p_{\bar{l}} + p_1)^2} + \frac{\gamma^{\mu} (\not{p}_a - \not{p}_l - \not{p}_{\bar{l}}) \gamma^{\nu}}{(p_a - (p_l + p_{\bar{l}}))^2} \right) | a^- \rangle \tag{2.4.3}$$

$$\cdot \langle l^- | \nu | \bar{l}^- \rangle \,, \tag{2.4.4}$$

where we take that p_l and $p_{\bar{l}}$ are the momenta of the lepton (e^-, ν) and anti-lepton ($\bar{\nu}$, e^+) which result from the decay of the W-boson in any particular process. However, additional complications arise when it comes to the consideration of swapping between different channels in W+Jets. To begin, before the addition of any new processes, a gg incoming state is not feasible within `HEJ`, and as such the application of two CAM factors to transform a quark-quark incoming state would not have made sense due to the lack of a possible emission site of a W-boson.

We also have to be more careful when swapping between quarks and anti-quarks when there is a W-boson involved. If the leg in question emits the W-boson, it is no longer a question of simply swapping the helicity as was the case due to the relatively simple relation used in the pure jet current swap in Eq. (2.3.11). Instead we need to consider a few more relations:

$$\langle i^- | \mu \not{p} \nu | j^- \rangle = \langle j^+ | \nu \not{p} \mu | i^+ \rangle \tag{2.4.5}$$

$$\langle i^- | \mu \not{p} \nu \not{q} \rho | j^- \rangle = \langle j^+ | \rho \not{q} \nu \not{p} \mu | i^+ \rangle \,. \tag{2.4.6}$$

Now, if we swap a quark which emits a W-boson to an anti-quark which emits a

W-boson, we see the following behaviour:

$$\langle 1^- | \mu \not{p} \nu \not{q} \rho | a^- \rangle = \langle 1 | \mu \not{p} \nu \not{q} \rho P_L | a \rangle \to \langle a | \rho P_L \not{q} \nu \not{p} \mu | 1 \rangle = \langle 1^+ | \mu \not{p} \nu \not{q} \rho | a^+ \rangle \,. \tag{2.4.7}$$

We observe that rather than simply ignoring the change in helicity, it has a fundamental change to the structure of the current which cannot be ignored. As such, we need to swap the helicity and continue as we would in the calculation as usual.

We now have predictions for all fundamental W+Jets processes which fall under the High Energy Limit, as by simply inserting this spinor string in Eq. (2.4.1) into Eq. (2.3.28) we have the `HEJ` approximation for any resulting matrix element, and we can proceed with resummation and matching as with QCD processes. We note that this approximation does not take into account the scenario where interference occurs between the W-boson emission sites from two identical legs; however, this has been found to be negligible in the high energy limit, which is expected, as the different emission sites are separated by several units of rapidity, and it has been found that a W-boson is more likely to be close in rapidity to its emission site than far away. Note, that because we read in fixed-order events as input in `HEJ2` we don't actually have to consider which leg will emit a W-boson, since the change in flavor which results from the emission will already signal where the emission occurred.

It is at this point that we note also that in `HEJ` we assume the *CKM Matrix* is the identity matrix, and that there are no intergenerational flavor changes within the model. As such, any factors of CKM matrix elements are implicitly taken to be unity (or zero in the case of off-diagonal elements). This is, of course, an approximation;

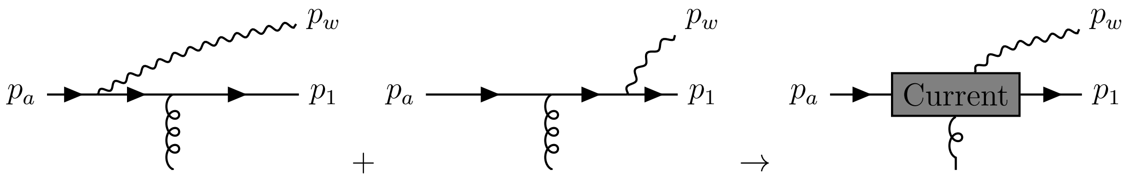

Figure 2.8: *The possible W-Emissions from the external lines with an effective vertex*

although it is one which factors out since this factor is included in the fixed-order matrix element used as input and utilised within the matching process.

2.5 Implementation within `HEJ2`

It is worth noting that while the unordered sub process had been calculated and presented within `HEJ1`, on the release of `HEJ2`, there was only support for pure jets production, and jet production in association with a Higgs Boson, both with very limited support for subleading processes. Support for jet production in association with $W^{\pm}$-Bosons, and Z-Bosons was included in `HEJ` V2.1. As such, a significant portion of the work behind this thesis has involved porting all necessary functionality into the new phase-space integration and matching methodology. This has also led to the porting of all remaining subleading processes for pure jet production.

Before this section, we discussed the calculation as it was at the time of release of `HEJ1`. We now present very briefly a motivation as to why this is insufficient for a full picture of the processes involved, particularly when very large energies are involved.

The hierarchy of scales involved in the Regge Limit, Eq. (2.2.1), leads to large logarithms which are resummed by the approach utilised by `HEJ` and imposing the limit at the level of the amplitude construction allows for the extraction of the leading logarithmic contributions. This means in practice, that the dominant contributions in terms of the cross-section, the FKL configurations, are included by `HEJ` in the high-energy-limit to all orders at leading logarithmic accuracy.

All other channels through which the incoming particles can interact to various outgoing states are included only through matching. As a result, they are not brought under logarithmic control and are included solely through matching to leading-order calculations within `HEJ`. We will discuss in Chapter 3 how this process differs in revamped version of `HEJ2`; however, the point stands there are many processes which are therefore excluded from this calculation to all-order at leading logarithmic accuracy.

Higher orders are needed to obtain a more accurate description of data by simply including more interaction channels. This is clearly demonstrated when one looks at appropriate distributions. For example, in Fig. 2.9, we see the differential cross-section with respect to the scalar sum of transverse momenta, H_T for W-boson production in association with at least two jets at $\sqrt{s} = 7$TeV. As the transverse momentum of the jets increases the requirement of the high-energy-limit, that $\hat{s}_{ij} \gg |\hat{t}_{ij}|$ is less and less convincing, since the larger $\sum_i \hat{t}$ is, the more capacity there is for a larger individual $\hat{t}_i$. In simple terms, this means that our high-energy-limit is less dominated by the FKL contributions which are the main amplitudes in play for a purely MRK limit.

Instead then, it is clear that we need to work on the inclusion of subleading terms to better our predictions. This means that our reliance on fixed-order calculations is lessened a great deal, as well as providing an excellent leaping off point for the journey towards NLL accuracy within `HEJ`. While we have demonstrated the necessity of this for a very particular variable, it should be understood by the reader that the improvements made by the inclusion of subleading terms will have a far greater reach in the predictions made by `HEJ`, since it can also be considered a relaxation of the strict limit imposed by the Multi-Regge-Kinematics thereby increasing the area of phase-space in which `HEJ` can be reasonably applied. In the end, it means that more terms are included and logarithmically controlled.

We will discuss at length in Chapter 4 what these contributions entail; however, we will simply state for now that in HEJ formalism, processes that can be drawn solely via a gluon exchange in this planar representation are the Leading Logarithmic (LL) channels. If a single t-channel gluon is changed for a quark, the diagram will be suppressed by an invariant mass parameter between the corresponding outgoing jets - exactly the Regge scaling which was discussed in Section 2.2.1 - which leads to such processes being referred to in HEJ formalism as subleading channels, or Next-to-Leading Logarithmic (NLL) processes.

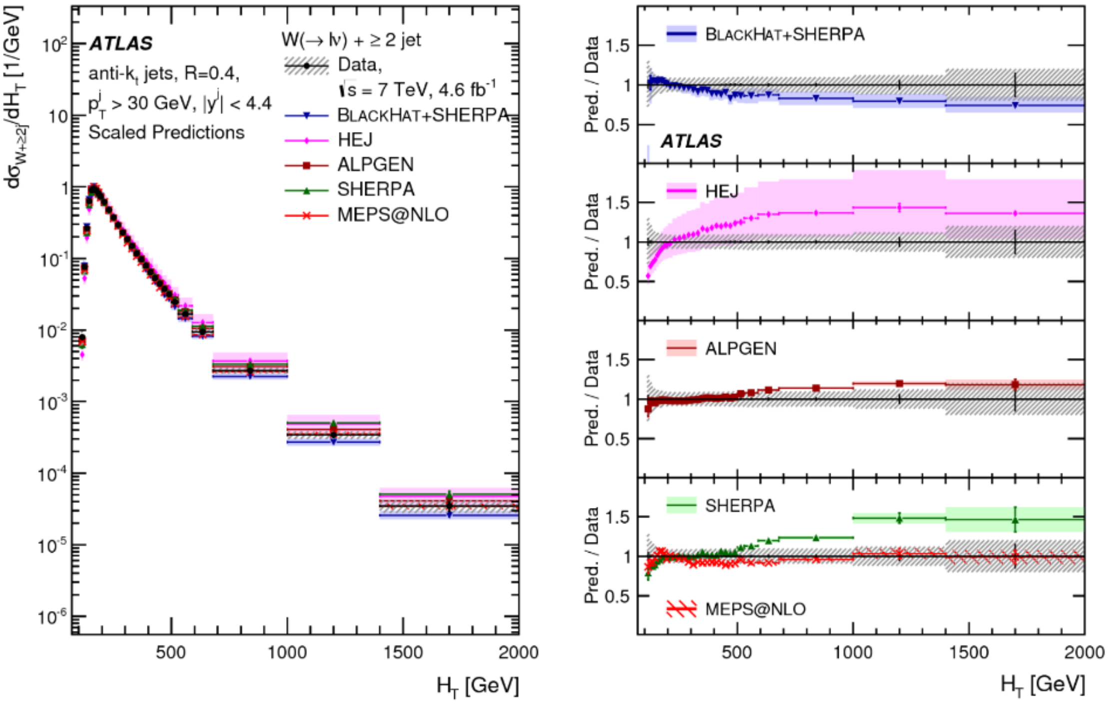

Figure 2.9: *Differential cross-section with respect to the scalar sum of transverse momentum, H_T at $\sqrt{s} = 7$ TeV. Figure reproduced from Ref. [6]. A significant discrepancy is observed between **HEJ** and **ATLAS** data for large H_T.*

.

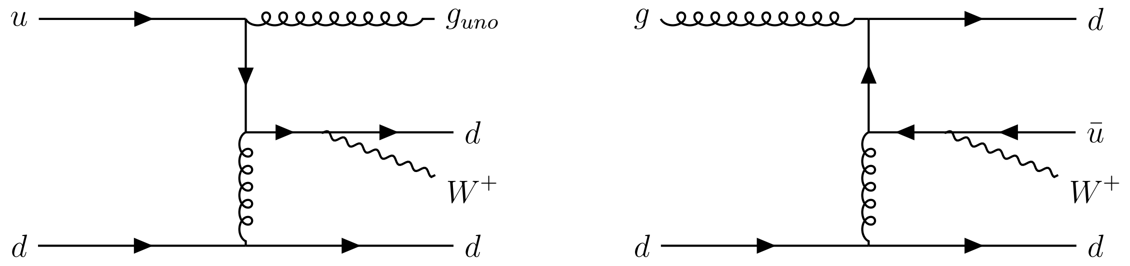

(a) Example Unordered Process **(b)** Example Extremal $q\bar{q}$ Process

Figure 2.10: *Planar representations of the two different possible 3j subleading contributions. Notably, when in a planar representation it is impossible to draw a planar diagram with the corresponding external legs and the same strict rapidity ordering without the use of a t-channel propagator.*

One then quickly realises that there are only three possible categories of subleading process in HEJ beyond the strict FKL ordering:

1. Emission of an Unordered Gluon, AKA *Unordered*
2. Extremal Quark pair production, AKA *Extremal* $q\bar{q}$
3. Central Quark pair production, AKA *Central* $q\bar{q}$

The first of these, the *unordered* subleading channel, had already been implemented within other processes within `HEJ` before the release of `HEJ2`. As can be seen in the planar representations illustrated in Fig. 2.10a, the t-channel quark propagator indeed leads to a suppression of the matrix element as predicted by Regge Scaling. It has also been shown that the second subleading channel, the extremal $q\bar{q}$ process type can be derived from the unordered subleading channel within `HEJ` through the use of crossing-symmetry. As can be seen in Fig. 2.10b, this also requires a t-channel quark propagator to be drawn in a planar representation.

The final subleading channel, known as the Central $q\bar{q}$ type, is the focus of the work in this thesis. Its inclusion in W+Jets concludes all possible real emission cases for the move towards NLL accuracy predictions within `HEJ`. We will pick up the discussion of these pieces in Chapter 4. First, we will take a look at the integration method employed within `HEJ`, and how we have improved it between `HEJ1` and `HEJ2`.

CHAPTER

THREE

MONTE CARLO SIMULATIONS

> Monte Carlo is an extremely bad method; it should only be used when all alternative methods are worse
>
> *Cécile Dewitt-Morette* [75]

There are many numerical integration methods available. Monte Carlo integration is horribly inefficient and should only be used when the other numerical methods are even less efficient. Depending on your tastes you could choose to convert your integral into a discrete sum, use the trapezoid rule or even Simpson's Rule. These methods typically yield rapid convergence and satisfactory results in numerous scenarios. However, when dealing with higher-dimensional integrals, one encounters the *Curse of Dimensionality*, a concept introduced by Richard E. Bellman. Applied to the scenario of integration it states that integrals of higher dimensions are significantly more complex and computationally intensive. For example, if performing integration in more than $d > 8$ dimensions, Monte Carlo integration generally outperforms even Simpson's rule in terms of convergence [75]! In particle physics, particularly within `HEJ`, we often face very high dimensionality due to final-state multiplicities that can range from 20 to 30 particles, and therefore, as a last resort, we consider the Monte Carlo method.

In fact, the preceding paragraph was somewhat facetious, intended to emphasize that Monte Carlo integration is fundamentally inefficient. Consequently, it demands careful manipulation of the calculation to maximize efficiency. This chapter covers the basics of Monte Carlo generation, its use within the particle physics community and then follows this with a discussion of the sampling used with `HEJ` events to improve efficiency and the implications this has. Despite earlier criticisms, Monte Carlo integration allows simultaneous calculation of all required distributions, a task not feasible with alternative integration methods, and enables straightforward implementation of cuts in calculations. These additional capabilities clearly establish Monte Carlo integration as the most versatile—and indeed most efficient—method for integration in extremely high-dimensional phase-space scenarios

3.1 What is a Monte Carlo Generator

Monte Carlo integration is a method of stochastic integration which can be used to approximate integrals numerically. The name was derived in the 1940s from the Monte Carlo resort - famous for its casinos. The etymology of this name has been recycled many times, for example with the *VEGAS* algorithm named after another Casino location. If we briefly consider what the process of integration is we can quickly ascertain that if we can find the area under a curve then we can evaluate an integral numerically. Generally, Monte Carlo integration operates by estimating the area through the ratio of randomly generated points that fall within the area of interest.

3.1.1 First Example

A very simple example which illustrates the process nicely is in the use of Monte Carlo integration to calculate the area of a circle. To numerically integrate, we need to estimate the area enclosed by a given shape accurately. Consider a circle inside a box, as in Fig. 3.1. The circle in this case is highlighted as the area we wish to calculate. Since we trivially know the area of the square ($A_{\text{total}} = 6 \cdot 6 = 36$) we randomly select points within this two-dimensional plane and determine whether they lie inside the circle. For this example we generated random points using two random flat generations within `Python`'s `Random` module, and then plotted basically the output in two planes[1] The ratio of points inside the circle to total number of points will be our prediction of the ratio of the circle and squares area's. This leads to:

$$\frac{p_{\text{circle}}}{p_{\text{total}}} = \frac{A_{\text{circle}}}{A_{\text{total}}} \tag{3.1.1}$$

$$\Rightarrow A_{\text{circle}} = \frac{p_{\text{circle}}}{p_{\text{total}}} A_{\text{total}} = 27.36\,. \tag{3.1.2}$$

Note how similar this estimation is to the true value of $\pi r^2 = 28.27$, but also that if we know the radius of the circle, we can in fact estimate the value of the fundamental constant π, using this method, giving us the central value prediction: $\pi = 3.04$; a remarkable achievement from 50 random points being generated in a 2D-plane. It is clear that we need to be able to estimate the error involved in this calculation for it to have any meaning at all, so, we consider the errors within Monte Carlo methods.

3.1.2 The Error of Our Ways

To begin this discussion, we will consider a simple integral:

$$\langle f \rangle = \frac{\int_\Omega f(\vec{x}) d\vec{x}}{\int_\Omega d\vec{x}}\,. \tag{3.1.3}$$

If we apply a Monte Carlo method to this integral and choose M random points x_i in Ω then we obtain the expression:

$$\langle f \rangle \approx \frac{1}{M} \sum_{i=1}^{M} f\left(\vec{x}_i\right)\,. \tag{3.1.4}$$

---

[1] Note, we have naturally chosen a Cartesian coordinate system here to simplify the discussion, but any coordinate system would of course be sufficient.

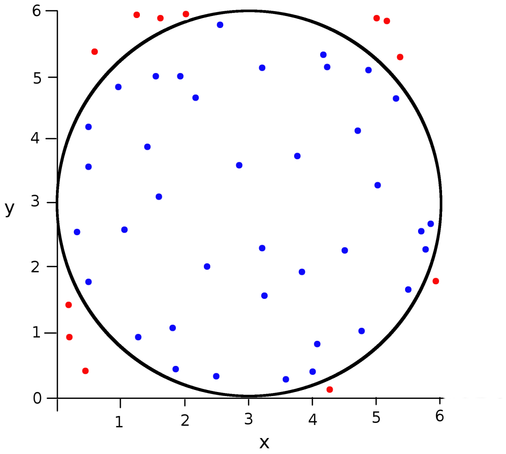

Figure 3.1: *This illustrates the idea of a Monte Carlo integration. By taking the ratio of points which lie within the circle it is possible to work out the area of the circle.*

This yields an approximate numerical result which has a well-known statistical error:

$$\Delta = \sqrt{\frac{\sigma^2(f)}{M}}, \tag{3.1.5}$$

where $\sigma^2(f)$ is simply the variance:

$$\sigma^2(f) = \left\langle f^2 \right\rangle - \langle f \rangle^2 , \tag{3.1.6}$$

and M is the number of points used in the integration. This resulting expression for the error of the Monte Carlo integration is valid in the limit of large M where according to the central limit theorem [75] we expect the result of multiple measurements of an integral with values I_n to be normally distributed around a mean $\langle I \rangle$. The standard deviation of these results, σ_M is given by:

$$\sigma_M^2 = \left\langle I^2 \right\rangle - \left\langle I \right\rangle^2, \tag{3.1.7}$$

where

$$\left\langle I \right\rangle = \frac{1}{M} \sum_{n=1}^{M} I_n \tag{3.1.8}$$

$$\left\langle I^2 \right\rangle = \frac{1}{M} \sum_{n=1}^{M} I_n^2 . \tag{3.1.9}$$

For large M we obtain [75]:

$$\sigma_M \approx \frac{\sigma}{\sqrt{N}} \,. \tag{3.1.10}$$

Notably here we see that the uncertainty given in Eqs. (3.1.5) and (3.1.10) is proportional to the inverse square root of the number of points used in the integration[1]. This means to reduce the error by a factor of 2 it is necessary to increase the number of points of integration fourfold. It is necessary to multiply the number of points of integration by 100 to reduce the error to 10% of its previous value. The dependence on N in Eq. (3.1.10) is undesirable especially when attempting high precision results (as we are), but there is simply no alternative which offers as much flexibility or even as fast convergence at such high dimensionality. With the help of *importance sampling* (see Section 3.1.4) the situation can be improved by a multiplicative factor of up to 10^6 [75] but the dependence on N remains the same. A crucial point of Monte Carlo integration is that the these points must be random. This means we need some method to generate random numbers to fuel the integration.

3.1.3 Random Number Generation

For the Monte Carlo Integration to function we therefore require random numbers. While it may be possible to generate truly random numbers based on the many values of computer state which are changing over time, generating truly random results is actually an undesirable premise for us, since it would make debugging problems or reproducing interesting phase-space points significantly more difficult.

Luckily, it is far easier to produce a string of fully deterministic and seemingly random[2] *pseudo-random numbers.* All that we require is a ‘seed’ number to initialise a Random Number Generator (RNG). By using the same random number seed for each integration, we can ensure reproducibility of the result. On the other hand if we want to produce meaningful results we need to ensure the random numbers we

---

[1] luckily this is independent of the number of dimensions involved in the integration

[2] by this, we mean that each number produced by the algorithm will not have any relation to the previously generated number in the string

produce are ‘random’ enough, and that means that there is no discernible pattern in their generation.

When choosing a random number set it is important to show that the set of pseudo-random numbers adheres to many requirements. Firstly you want the *Pseudo-Random Number Generator* (PRNG) to produce a string of numbers with a high multiplicity which pass statistical tests and replicating random number sequence distributions well. One well known statistical test is the Spectral Test shown in Fig. 3.2 [76]. This was the test which even well-designed Linear Congruential Generators (LCG) could be shown to be problematic with. It shows that if one considers the relationship between successive points in a LCG there is a distinctive pattern which shows itself in plots such as that in Fig. 3.2.

LCG Generators operate in a straightforward manner. The next number in the string is determined fully by an equation of the form:

$$x_{i+1} = (x_i \cdot a + c) \mod n\,, \tag{3.1.11}$$

with a the multiplier, c the addition, n the modulus. There are many PRNG on the market now, yet one still has to be careful that they produce numbers which are random enough for purpose. For example, a random number generator may work fantastically with one seed, but get stuck in a very low multiplicity loop with another

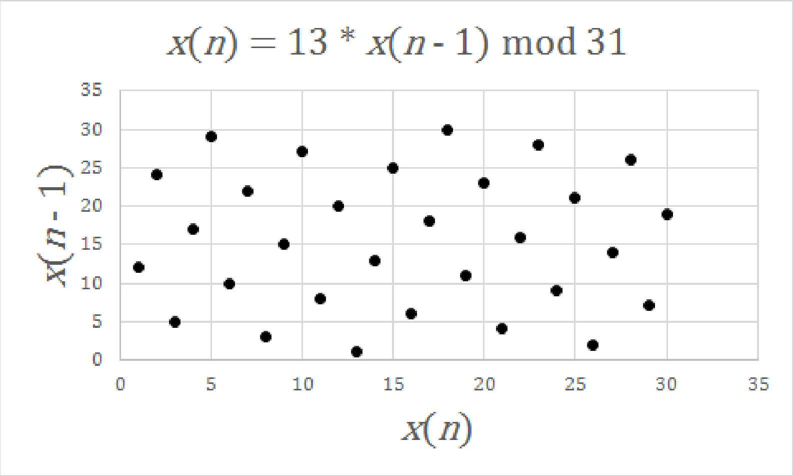

Figure 3.2: *This graph depicts the spectral test performed on a Linear Congruential Random Number Generator*

seed.

Due to the nature of `HEJ` we must perform very high dimensional integrations. As such, we need to be very stringent with our choice of random numbers. Because of this, `HEJ` does not produce random numbers itself; instead choosing to utilize an external program, `MinMax` to produce all the random numbers required.

3.1.4 Sampling

Once you have an integrator up and working the battle is not won. In particle physics generally—and particularly in `HEJ`—we have very high dimensional integrals which can be very complex to evaluate even numerically. This means that efficiency is a key priority. In the simple example outlined in Section 3.1.1 we performed flat sampling to choose our random points within the 2 dimensional plane. This means we didn't attempt to be clever with how we chose the random points. This would give a perfectly accurate answer as the number of points we choose, N, tends to being a large value; however, for a much more complex integration we need to be more efficient.

The integral may converge very quickly in some regions, but not so quickly in others. We can be smarter with our algorithms that we don't waste CPU time on calculating something we already know (or we are simply not interested in) when the error of the calculation is dominated by another region. This brings us to the discussion of how we use our random numbers.

There are many sampling types which allow you to improve the efficiency of integration. Flat sampling is essentially a brute-force method for achieving convergence. Depending on the integration in question it will almost certainly be better to use a smarter sampling. These methods are employed throughout Monte Carlo Generators to increase the speed of the convergence of the numerical integration. In previous versions of `HEJ` we utilised *importance sampling* to ensure that the MRK region of phase-space which we probe was under control quickly. However, due to the alteration in how matching is performed as of the release of `HEJ2` [73], we currently perform flat generation within specific regions. We discuss importance sampling here briefly since this is a method used throughout all fixed-order generators which we use as input for `HEJ`.

There are many available choices for this with `HEJ` opting for a particular variety of importance sampling. This approach leverages the fact that if one region of the integrand converges more quickly than others, it is advantageous to select test points more effectively within the integration space.

With importance sampling we no longer choose points uniformly but with a probability $p(\vec{x})$ which allows us to consider:

$$\langle f \rangle = \left\langle \frac{f}{p} \right\rangle_p := \frac{\int_\Omega \frac{f(\vec{x})}{p(\vec{x})} p(\vec{x}) d\vec{x}}{\int_\Omega d\vec{x}} , \tag{3.1.12}$$

where $w(\vec{x})$ is the importance sampling weight:

$$w(\vec{x}) = \frac{f(\vec{x})}{p(\vec{x})} . \tag{3.1.13}$$

To this end we essentially sample from a distribution different to the one we will integrate. This concept is demonstrated (qualitatively) in Fig. 3.3. The distribution we sample from is different from the original distribution. This allows us in the case in Fig. 3.3 to focus our integration on the tail of the distribution to increase the convergence there.

This is VEGAS importance sampling, which takes sampling and adaptive techniques to focus computational resources where they are most needed on a real integration run. It does this by approximating the integrand with a piecewise-constant probability density function [77], which in our context is a parton density function (PDF) that resembles the function's structure [53].

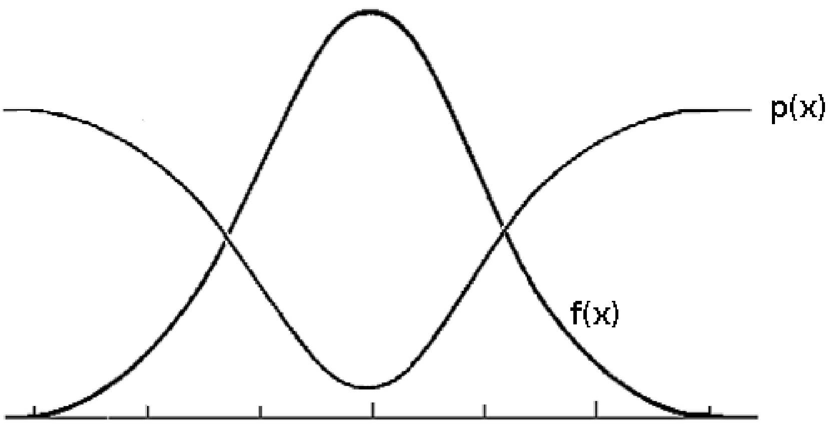

Figure 3.3: *A depiction of importance sampling. A function $f(x)$ is to be integrated, but we sample points for the Monte Carlo integration in a probabilistic fashion from the distribution $p(x)$.*

3.2 Phase-Space Generation in HEJ

If we want to calculate the cross-section predicted by the formalism of `HEJ` in Eq. (2.3.31) we need to perform numerical integration, and the best methodology for such a high dimensional integral as this is through Monte Carlo integration.

There has been a radical change to how this is performed in `HEJ2` as compared to the original release of `HEJ`, and that is namely that we now take fixed-order event files as input and supplement their cross-section prediction with the resummation performed by `HEJ` [73]. Consequently, we require a method for performing this integral, along with an entirely new phase-space generation approach.

3.2.1 Changes needed for HEJ2

Firstly, we must rewrite Eq. (2.3.31) to achieve fixed-order accuracy for jet rates within the `HEJ` framework, enabling resummation over fixed-order samples of exclusive jet rates. It has been found that this methodology is significantly faster than old implementations of the `HEJ` resummation and has the added benefit that eventually we will be able to match to NLO[1] event samples.

So, as of `HEJv2.0`, we match to leading-order using exclusive jet event files as input.

---

[1] far from trivial, there are many kinks to figure out

We begin by introducing an integration over the Born level kinematics of the on-shell reshuffled jets $\{j_B^i\}$ which are reconstructed from the resummed kinematics.

$$
\begin{aligned}
\sigma_{2j}^{\text{resum,match}} = \sum_{f_1,f_2} \sum_{m} \prod_{j=1}^{m} & \left(\int_{p_{j\perp}^B=0}^{p_{j\perp}^B=\infty} \frac{\mathrm{d}^2\mathbf{p}_{j\perp}^B}{(2\pi)^3} \int \frac{\mathrm{d}y_j^B}{2} \right) (2\pi)^4 \, \delta^{(2)}\!\left(\sum_{k=1}^{m} \mathbf{p}_{k\perp}^B \right) \\
& \times \; x_a^B \; f_a(x_a^B, Q_a^B) \; x_b^B \; f_b(x_b^B, Q_b^B) \; \frac{\overline{|\mathcal{M}^B|}^2}{(\hat{s}^B)^2} \\
& \times \frac{w_{m-\text{jet}}}{\overline{|\mathcal{M}^B|}^2} \times (2\pi)^{-4+3m} \; 2^m \\
& \times \sum_{n=2}^{\infty} \mathbf{T}_y \prod_{i=1}^{n} \left(\int_{p_{i\perp}=0}^{p_{i\perp}=\infty} \frac{\mathrm{d}^2\mathbf{p}_{i\perp}}{(2\pi)^3} \int \frac{\mathrm{d}y_i}{2} \right) \mathcal{O}_{mj}^e \\
& \times \left(\prod_{l=1}^{m-1} \delta^{(2)}(\mathbf{p}_{\mathcal{J}_l\perp}^B - \mathbf{j}_{l\perp}) \right) \left(\prod_{l=1}^{m} \delta(y_{\mathcal{J}_l}^B - y_{\mathcal{J}_l}) \right) \\
& \times \frac{\overline{|\mathcal{M}_{\text{HEJ}}^{f_1 f_2 \to f_1 g \cdots g f_2}(\{p_i\})|}^2}{\hat{s}^2} \times (\hat{s}^B)^2 \\
& \times \frac{x_a f_{a,f_1}(x_a, Q_a) \; x_b f_{b,f_2}(x_b, Q_b)}{x_a^B \; f_{a,f_1}(x_a^B, Q_a^B) \; x_b^B \; f_{b,f_2}(x_b^B, Q_b^B)} \; (2\pi)^4 \, \delta^{(2)}\!\left(\sum_{k=1}^{n} \mathbf{p}_{k\perp} \right) \; \mathcal{O}_{2j}(\{p_i\}) \, .
\end{aligned}
\tag{3.2.1}
$$

The first two lines represent LO generated events. Obviously, $\frac{w_{m-\text{jet}}}{\overline{|\mathcal{M}^B|}^2} = \overline{|\mathcal{M}^t|}^{-2}$, the born level HEJ approximation to the matrix element, which we have written in this form to explicitly show the cancellation of the fixed-order Matrix element. Now, we need to generate all the resummation kinematics which are overlaid on each specific reconstructed born level event, so we delve into a formalism which allows for this to be achieved efficiently.

We note on the fifth line the δ-functional which connects the reconstructed Born-level kinematics with the resummation phase-space points. This means that we have the following relation between the transverse momenta in both cases:

$$
\mathbf{p}_{\mathcal{J}_l\perp}^B = \mathbf{j}_{l\perp} \equiv \mathbf{p}_{\mathcal{J}_l\perp} + \mathbf{q}_\perp * \frac{|\mathbf{p}_{\mathcal{J}_l\perp}|}{P_\perp} \, , \tag{3.2.2}
$$

where p^B is the momentum of a born level jet, $q_\perp$ is the sum of non-jet resummation partons which by momentum conservation equals minus the transverse momentum of the resummation jets and $P_\perp$ is the scalar sum of the resummation jets. Finally, we note that the rapidities of the jets are kept fixed. To begin with fixed-order events and apply high-energy logarithmic resummation, we must invert this relation and reshuffle the transverse momenta of resummation jets while maintaining their rapidities fixed relative to the Born-level fixed-order jets. So, in order to perform this phase-space integration we change our δ-functions $\delta^{(2)}(\mathbf{p}^B_{\mathcal{J}_l\perp} - \mathbf{j}_{l\perp})$ to be linear in the resummation parton momenta instead of the fixed-order event momenta. This inherently introduces a Jacobian:

$$\prod_{l=1}^{m} \delta^{(2)}(\mathbf{p}^B_{\mathcal{J}_l\perp} - \mathbf{j}_{l\perp}) = \frac{1}{\Delta} \prod_{l=1}^{m} \delta^{(2)}(\mathbf{p}_{\mathcal{J}_l\perp} - \mathbf{j}^B_{l\perp}) \,, \tag{3.2.3}$$

where $\mathbf{j}^B_{l\perp}$ only depends on the Born momenta from the input fixed-order phase-space point. We have extended the product to run to m instead of $m-1$ by eliminating the last δ function $\delta^{(2)}(\sum_{k=1}^{n} \mathbf{p}_{k\perp})$. The Jacobian Δ is the determinant of a $2m \times 2m$ matrix with $l, l' = 1, \ldots, m$ and $X, X' = x, y$.

$$\Delta = \left| \delta_{ll'}\delta_{XX'} + \frac{q_X \, p_{\mathcal{J}_{l'}X'}}{|\mathbf{p}_{\mathcal{J}_{l'}\perp}| P_\perp} \left(\delta_{ll'} - \frac{|\mathbf{p}_{\mathcal{J}_l\perp}|}{P_\perp} \right) \right| . \tag{3.2.4}$$

We are performing a Monte Carlo integration of resummation phase-space points around each individual fixed-order input event. As such, we will be generating many resummation phase-space points for every fixed-order event taken as input. A significant concern arises from our lack of direct control over fixed-order event generation, making several conditions necessary:

1. We have to trust the fixed-order generation is performed correctly.
2. We need the fixed-order inputs distributions to be smooth and stable
3. We need to know some information about certain parameters within the fixed-order generation.

Let us break this down, point by point. First, if there are any bugs within any external generator which we rely on for input to our simulation, we simply have no control over these, and as such we are at the mercy of the programs whose integrations we are attempting to improve.

Secondly, we are also limited to the accuracy of the result produced by the fixed-order event sample. That is, if the results for our input have yet to converge, the convolution of the errors which are present in the input will ensure that no matter how good the convergence of our integration on each individual fixed-order phase-space point is, we simply cannot improve upon the baseline of error from the fixed order input. This implies two consequences: we must verify that our input results are stable, but also that we are hamstrung by the computational limitations which are present in fixed-order generators.

This is even true at LO; although matrix elements and phase-space integrations are *'trivial'*, integrating high-multiplicity events—particularly in association with boson production—remains computationally challenging. As such, we have also developed a fixed-order Generator, `HEJFOG` alongside the release of `HEJ2` [73] which uses the `HEJ` approximations of matrix elements to produce higher multiplicity events than would otherwise be computationally feasible with traditional fixed-order generation. As such, using this method, we have actually been able to provide resummation on Higgs Boson production in association with 7 Jets in the past [7, 78].

Finally, addressing the third point, we require information about the fixed-order sample that typically lies outside the standard particle physics event file specifications. Namely, we need to know several parameters such as the jet cuts to ensure cohesion between both calculations is as smooth as possible. With this all in mind, we move on to the generation of resummation phase-space points within `HEJ2`.

3.2.2 Generation of Resummation Phase-Space Points

As with all Monte Carlo integrations, we generate random numbers and assess their impact; phase-space sampling follows the same principle. One number which we must generate for each phase-space point we generate is the number of extra gluon emissions. The optimal gluon multiplicity and its distribution have been empirically determined [7] through comprehensive phase-space studies in `HEJ1`. This study confirmed an expected strong correlation between emitted gluon multiplicity and

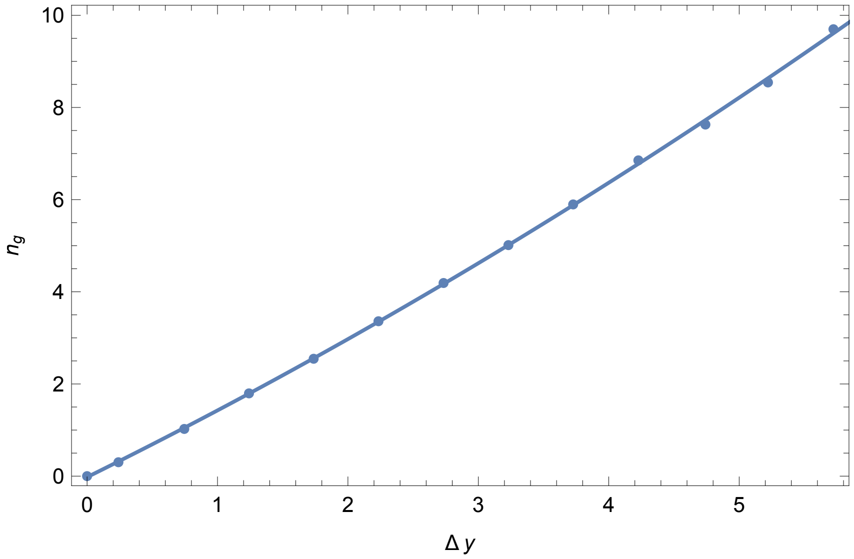

Figure 3.4: $\overline{n}_g$ *as a function of the rapidity gap between extremal jets.*

the rapidity span of the input event, revealing an approximately linear relationship augmented by a quadratic term for improved fitting at smaller rapidity intervals. This relationship can be seen in Fig. 3.4. The random number of gluons generated is sampled according to a Poisson distribution around this number for each resummation event corresponding to the original fixed-order event. The actual integration is fairly trivial. We first remove the rapidity ordering of the outgoing event to avoid double counting:

$$\mathbf{T}_y \prod_{i=1}^{n} \int \frac{\mathrm{d}y_i}{2} = \frac{1}{n!} \prod_{i=1}^{n} \int \frac{\mathrm{d}y_i}{2} \,. \tag{3.2.5}$$

We now address the task of assigning momenta to these gluons. Each fixed-order jet must contain at least one parton, which means we have $n_g = n_{g_{\max}} - n_{\mathcal{J}}$ gluons to assign. If we select random partons and rename the integration variables we obtain:

$$\frac{1}{n!} \prod_{i=1}^{n} \int [\mathrm{d}p_i] = \frac{1}{n_g!} \prod_{i=1}^{n_g} \int [\mathrm{d}p_i] \prod_{i=n_g+1}^{n} \int [\mathrm{d}p_i]\ \theta(p_i \text{ inside jet } i) \,. \tag{3.2.6}$$

The remaining gluons can be categorised as either emissions within Jets or outside of Jets. We will begin with a discussion of the emissions within Jets.

3.2.3 Number of emissions

Initially, we assume a uniform distribution of gluons in the y-ϕ plane; thus, the probability of any gluon emission within a jet is simply the ratio of the jet-covered area to the total available phase-space area.

Assuming each jet covers an area πR^2, with R being the jet radius parameter defined in Eq.(1.4.1), we proceed as follows. The total phase-space area is given by $2\pi\Delta y_p$, where Δy_p is the rapidity separation between the extremal partons, which is not known due to the possibility of emissions in the extremal jets. However, we can make the assumption that for very large rapidity spans, that there will be very few emissions within the extremal jets and as such we can assume $\Delta y_p = \Delta y_{\mathcal{J}}$, where $\Delta y_{\mathcal{J}}$ is the rapidity span of the original fixed-order event. Note that resummation within `HEJ` does not alter this value; it remains fixed throughout the calculation. Therefore, the probability for a gluon to end up inside a Jet for an event with m Jets is given by:

$$p_{\mathcal{J}_{\text{large}}} = \frac{(m-1)R^2}{2\Delta y_{\mathcal{J}}}\,, \tag{3.2.7}$$

For small rapidity gaps, this approximation overestimates the probability, as emissions within jets are more frequent, positioning extremal partons closer to jet boundaries. Hence, the total available phase-space becomes $2\pi(\Delta y_{\mathcal{J}} + 2R)$, giving us the probability for a parton to end up in a Jet as:

$$p_{\mathcal{J},<} = \frac{mR^2}{2(\Delta y_{\mathcal{J}} + 2R)}\,. \tag{3.2.8}$$

For the limit $\Delta y_{\mathcal{J}} \to 0$, this gives us $p_{\mathcal{J},<} \to mR/4$. This is notably equally invalid in the case of large rapidity separation; however, we note that both Eqs. (3.2.7) and (3.2.8) agree for $\Delta y_{\mathcal{J}} = 2(m-1)R$. As such we combine these approximations and use a different prescription for small and large rapidity spans:

$$p_{\mathcal{J}} = \begin{cases} p_{\mathcal{J}_{\text{large}}} & \Delta y_{\mathcal{J}} < 2(m-1)R \\ p_{\mathcal{J}_{\text{small}}} & \Delta y_{\mathcal{J}} >= 2(m-1)R\,. \end{cases} \tag{3.2.9}$$

We now know the number of emissions inside and outside jets within our new phase-space point; however, we do not yet have enough information to be able to model the emission of gluons within Jets, since emissions outside of Jets will cause a shuffle of the transverse momenta of the Jets, as we will see in the Section 3.2.4. Therefore, first, we must discuss the emission of gluons outside of Jets.

3.2.4 Treatment of gluons outside jets

Now we handle the momentum generation for the $n_g - n_{g,\mathcal{J}}$ gluons that are emitted outside of jets. In `HEJ`, the azimuthal angle ϕ is sampled uniformly within the range $0 \leq 2\pi$. There is a complication concerning the rapidity span, as the complete allowed rapidity range is unknown until the gluon emissions inside jets are generated. Therefore, we initially only generate the transverse momenta of gluons outside jets. We parameterise the generation such as:

$$p_\perp = \lambda + \tilde{p}_\perp \tan(\tau r)\,, \qquad \tau = \arctan\left(\frac{p_{\perp\mathcal{J}_{\text{min}}} - \lambda}{\tilde{p}_\perp}\right)\,, \tag{3.2.10}$$

where $r \in [0, 1)$, and we require that $p_\perp$ is always less than the minimum momentum $p_{\perp\mathcal{J}_{\text{min}}}$ required for a jet. We note that $\tilde{p}_\perp$ is a free parameter, it has been found that a good empirical value is $\tilde{p}_\perp = [1.3 + 0.2(n_g - n_{g,\mathcal{J}})]$ GeV. We then calculate $\mathbf{q}_\perp$ as the sum of the non-jet momenta and solve the system of non-linear equations in Eq. (3.2.2) for $p_{\mathcal{J}_{l\perp}}$. Thus, we successfully reshuffle the Born-level jet momenta, obtaining the momenta of resummation jets and ensuring momentum conservation despite the introduction of additional particles.

3.2.5 Treatment of gluons inside jets

We know the momenta which the jets in the resummation phase-space point will have, and as such, we now have enough information to generate the momenta of their constituent partons. Each jet is required to have at least one particle. The phase-space integral we aim to evaluate via Monte Carlo sampling is given by:

$$\prod_{i \text{ in } \mathcal{J}} \left(\int \mathrm{d}\mathbf{p}_{i\perp} \int \mathrm{d}y_i \right) \delta^{(2)}\left(\sum_{i \text{ in } \mathcal{J}} \mathbf{p}_{i\perp} - \mathbf{j}_{\perp}^{B} \right) \delta(y_{\mathcal{J}} - y_{\mathcal{J}}^{B}) \,. \tag{3.2.11}$$

For the case of one particle inside the jet, this integral is trivial. For the case of multiple particles, we first generate momenta for the first $n-1$ partons, and then calculate the final one through a delta functional ensuring that the overall jet momenta is as found. We parameterize particle generation relative to jet parameters, ensuring generated particles remain within their respective jets. As such, we use:

$$\phi_i = \phi_{\mathcal{J}} + \Delta\phi_i \,, \qquad \Delta\phi_i = \Delta R_i \cos(\Theta_i) \,, \tag{3.2.12}$$

$$y_i = y_{\mathcal{J}} + \Delta y_i \,, \qquad \Delta y_i = \Delta R_i \sin(\Theta_i) \,. \tag{3.2.13}$$

We uniformly generate Θ_i and ΔR_i, ensuring $\Delta R_i \leq R_{\text{max}}$, with an empirically determined optimal value $R_{\text{max}} = \frac{5R}{3}$. We can then write the phase-space integral for a single parton as:

$$\int \mathrm{d}\mathbf{p}_{\perp} \int \mathrm{d}y \approx \int_{\Box} \mathrm{d}x_{\perp} \mathrm{d}x_R \mathrm{d}x_{\theta} \; 2\pi \, R_{\text{max}}^2 \, x_R \, p_{\perp} \, (p_{\perp,\text{max}} - p_{\perp,\text{min}}) \,, \tag{3.2.14}$$

with

$$\Delta\phi = R_{\text{max}} x_R \cos(2\pi x_{\theta}) \,, \tag{3.2.15}$$

$$\Delta y = R_{\text{max}} x_R \sin(2\pi x_{\theta}) \,, \tag{3.2.16}$$

$$p_{\perp} = (p_{\perp,\text{max}} - p_{\perp,\text{min}}) x_{\perp} + p_{\perp,\text{min}} \,, \tag{3.2.17}$$

where $p_{\perp,\text{max}}$ is determined by the notion that the transverse momenta of the first $n-1$ constituent partons in the jet will not exceed the total jet transverse momentum $p_{\perp}$. This requirement gives us:

$$p_{i\perp,\text{max}} = \frac{p_{\mathcal{J}\perp} - \sum_{j<i} p_{j\perp} \cos\Delta\phi_j}{\cos\Delta\phi_i} \,. \tag{3.2.18}$$

We then determine the transverse momentum components of the final parton using the first delta function in Eq. (3.2.11). Similarly, the rapidity is fixed using the second delta function, enforcing the resummation jet rapidity to match that of the corresponding Born-level jet. Thus, after reshuffling, we assign the rapidity of the final parton to ensure this condition is satisfied. Therefore:

$$y_{\mathcal{J}}^B = y_{\mathcal{J}} = \frac{1}{2} \ln \frac{\sum_{i=1}^n E_i + p_{iz}}{\sum_{i=1}^n E_i - p_{iz}} \,. \tag{3.2.19}$$

With $E_n \pm p_{nz} = p_{n\perp} \exp(\pm y_n)$ this can be rewritten as

$$\exp(2y_{\mathcal{J}}) = \frac{\sum_{i=1}^{n-1} E_i + p_{iz} + p_{n\perp} \exp(y_n)}{\sum_{i=1}^{n-1} E_i - p_{iz} + p_{n\perp} \exp(-y_n)} \,, \tag{3.2.20}$$

which is a quadratic equation in $\exp(y_n)$. The physical solution of this is

$$y_n = \log\Big(- b + \sqrt{b^2 + \exp(2y_{\mathcal{J}})} \Big) \,, \tag{3.2.21}$$

$$b = \left(\sum_{i=1}^{n-1} E_i + p_{iz} - \exp(2y_{\mathcal{J}}) \sum_{i=1}^{n-1} E_i - p_{iz} \right) / (2p_{n\perp}) \,. \tag{3.2.22}$$

We eliminate the final rapidity integral by expressing the δ-function linearly in terms of the last parton's rapidity. This transformation leads to the addition of the Jacobian:

$$\left| \frac{\partial y_{\mathcal{J}}}{\partial y_n} \right|^{-1} = 2 \left(\frac{E_n + p_{nz}}{E_{\mathcal{J}} + p_{\mathcal{J}z}} + \frac{E_n - p_{nz}}{E_{\mathcal{J}} - p_{\mathcal{J}z}} \right)^{-1} \,. \tag{3.2.23}$$

At this stage, we revisit the momentum generation for gluons emitted outside jets. With the allowed rapidity span now established, we can uniformly sample the rapidities of the emitted gluons within this range.

CHAPTER

FOUR

SUBLEADING CHANNELS

In this chapter, we introduce the subleading channels present in the `HEJ` formalism and describe their implementation within the calculation.

The Leading Logarithm (LL) terms can be substantially improved, as the Multi-Regge Kinematics (MRK) limit corresponds to only a small region of phase space. Although the FKL contributions dominate, they do not represent the entirety of relevant processes; in fact, few contributions strictly conform to this limit. One way to improve the predictions we are able to make with the addition of this method of resummation is to relax the extreme constraints put in place with the MRK limit. This is, of course, highly non-trivial in most cases, as many of the conveniences afforded by the formalism arise directly from the strict nature of the MRK limit. We will begin with some motivation.

4.1 Motivation

While it may be clear to the reader that including more contributions should lead to a better result, we have not yet discussed the expected impact of this work. We now present quantitative demonstrations of the importance of NLL contributions

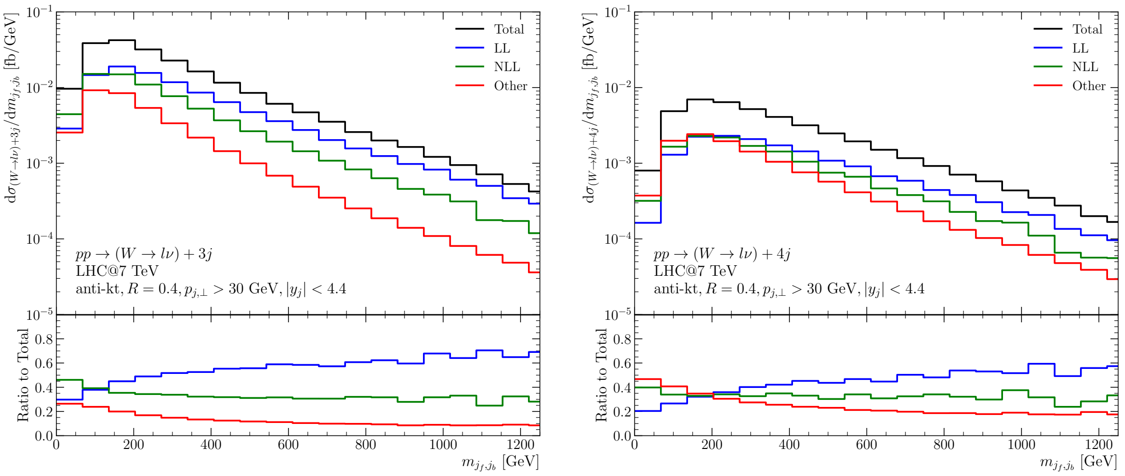

Figure 4.1: *The leading-order $W + 3 - jet$ [left plot] and $W + 4 - jet$ cross-sections [right plot] as a function of the invariant mass between the most forward and backward jets, m_{fb}. In addition to the total (black), we also show the split into the contributions from the LL configurations (blue), NLL configurations (green) and other configurations (red). As m_{fb} increases, the LL configurations increase in dominance but the NLL configurations remain significant*

in specific regions of phase space, serving as motivation for the subsequent sections. This discussion is more detailed in [9].

We can demonstrate the importance of the NLL contributions by looking into the breakdown of the LL and NLL contributions to Born-level processes for $2 \to 3$ and $2 \to 4$. Fig. 4.1 shows the different differential distributions for W + 3-jet and W + 4-jet production as a function of the invariant mass between the most forward and backward jets. In blue we see the LL contribution, in green we see the NLL component, and in red we see all other configurations.

This result was obtained using full SM scattering amplitudes and classifying the contributions according the states as summarised in Table 4.1. The plots were produced for 7TeV proton-proton collisions, and the jet cut off was set to $p_\perp > 30$ GeV and $|y_j| < 4.4$, though these parameter choices are not responsible for the observed behaviour [9].

What we see in Fig. 4.1, the LL components become increasingly dominant as m_{fb} rises, while the relative contributions from other components (including NLL)

	LL processes	NLL processes
$pp \to W + 3j$	$qg \to Wq'gg$, $qQ \to Wq'gQ$	$qg \to Wgq'g$, $qQ \to Wgq'Q$, $gg \to Wq\bar{q}'g$, $gQ \to Wq\bar{q}'Q$, $gQ \to Wq\bar{q}Q'$
$pp \to W + 4j$	$qg \to Wq'ggg$, $qQ \to Wq'ggQ$	$qg \to Wgq'gg$, $qQ \to Wgq'gQ$, $qQ \to Wq'gQg$, $gg \to Wq\bar{q}'gg$, $gQ \to Wq\bar{q}'gQ$, $gQ \to Wq\bar{q}gQ'$, $Qg \to WQ'q\bar{q}g$, $Qg \to WQq\bar{q}'g$, $gg \to Wgq\bar{q}'g$, $Q\tilde{Q} \to WQ'q\bar{q}\tilde{Q}$, $Q\tilde{Q} \to WQq\bar{q}'\tilde{Q}$

Table 4.1: *A summary of the particle configurations which enter the LL and NLL lines in Fig. 4.1 and Fig. 4.2. All particles except for the W are listed in rapidity order. q, Q etc. may refer to quarks or anti-quarks. Each process refers to itself and its symmetric counterpart, i.e. $qg \to Wq'gg$ is shorthand for $qg \to Wq'gg + gq \to Wggq'$. All other subprocesses not listed above are included in the line labelled 'Other'.*

diminish. However, even at $m_{\text{fb}} = 1$ TeV the sub-leading contributions contribute 30% in the $W+3$-jet case and 40% in the $W+4$-jet case.

The importance of NLL contributions is even greater for transverse momentum distributions such as those depicted in Fig. 4.2. These plots, that show $d\sigma/dp_{\perp,1}$, with $p_{\perp,1}$ the transverse momentum of the hardest jet, no correlation is expected between the MRK limit—where LL contributions dominate—and the transverse momentum. Therefore, there is no systematic suppression of sub-leading channels for this distribution – we actually see that the size of the sub-leading channels increase to 60% for $W+3$-jets and 70% for $W+4$-jet production.

Prior to the introduction of NLL components into the `HEJ` formalism, these subleading-channels were only included via fixed-order matching; meaning that these large components did not receive the all-order resummation that the LL channels did. In the following sections we present the calculations of the relevant NLL components in $W+$-jets so that these components can be included in `HEJ` without fixed-order matching, and instead receive the all-order treatment.

With the inclusion of NLL components in this manner, all-order resummation is applied to a substantially larger portion of the total cross-section, increasing from 40% to 80% in inclusive $W+3$-jet production, and from 30% to 70% in inclusive $W+4$-jet production.

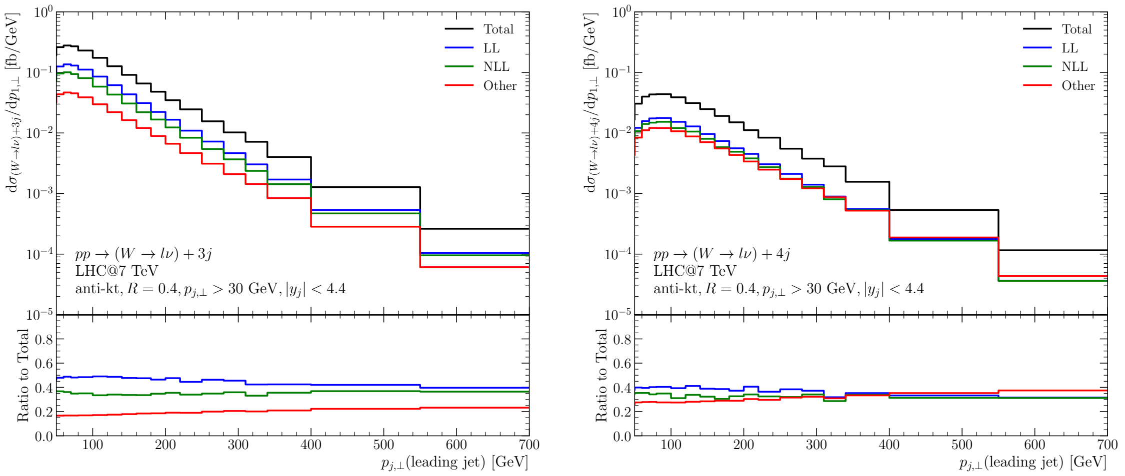

Figure 4.2: *The leading-order $W + 3 - jet$ [left plot] and $W + 4 - jet$ [right plot] cross-sections as a function of the transverse momentum of the hardest jet, $p_{\perp,1}$. In addition to the total (black), we also show the split into the contributions from the LL configurations (blue), NLL configurations (green) and other configurations (red). As $p_{\perp,1}$ increases, the LL configurations decrease in importance underlining the importance of also applying resummation to the NLL contributions.*

4.2 Next-To-Leading-Logs

By relaxing the constraints we will be able to include some sub-leading terms of Next-To-Leading-Log (NLL) accuracy which still contribute significantly. All the sub-leading channels that we will look at in this section are real emissions at NLL in HEJ formalism. The resummation that we perform continues to make use of the LL virtual corrections provided by the Lipatov ansatz (Eq. (2.3.26)). The extra IR divergences one might expect as a result of these real emissions being added to the calculation here don't apply for two reasons, for the most part, these NLL pieces come from a rearrangement of the final state in rapidity or the changing of parton flavors, and there is no new emission that one would expect in NLL descriptions in other formalisms - the poles in the diagrams remain unchanged, and thus the cancellation remains valid. Further, when we are defining our Matrix Element, there is an implicit statement that each leg of the diagram exists in a separate jet - and thus we have cut away any soft or collinear divergence one may expect to arise in the resolution of these legs.

Some sub-leading terms include the substitution of one t-channel gluon for a quark or a gluon emitted outside (in terms of rapidity) of the extremal partons (referred to as an unordered emission) [7]. The inclusion of these sub-leading processes goes a long way to stabilising the dependence on the scale choice [9]. Of course other processes besides ($qQ \to qg...gQ$) exist and although these will not be strictly FKL amplitudes, we can still perform some resummation. For example ($gQ \to gq\bar{q}g..gQ$) can be related to the unordered FKL results easily.

It has been shown [7] that the contribution of these sub leading terms is suppressed by one power of the invariant mass $\hat{s}_{ij}$. This will be covered in more detail in Sections 4.3, 4.4 and 4.5. This means that the diagram in Fig. 2.7 is a factor of $\hat{s}_{ij}$ larger than the Feynman Diagram given in Fig. 4.5. This suppression is also true for the unordered case as given in Fig. 4.4. The plots in Fig. 4.3 demonstrate this suppression of the subleading terms. It shows the behaviour of the matrix elements of the full FKL contribution, $|\mathcal{M}_1|$, and two different unordered contributions, $|\mathcal{M}_2|$ and $|\mathcal{M}_3|$ for $(2 \to 3)$ over different rapidity differences. Notably when plotting $|\mathcal{M}|^2/s^2$ the FKL contribution tends to a constant at large rapidity difference, whereas the non-FKL contributions are suppressed. In the right plot of Fig. 4.3 we see this has led to a suppression factor of $s_{j_1 j_2}$ for the non-FKL contributions. The difference in the unordered case is the quark exchange in the t-channel instead of a gluon exchange leading to this suppression.

If our approximations do not include a potential resummation point we simply use the fixed-order result for that particular kinematic arrangement. `HEJ` will not make good approximations to anything not included in this limit. As such we need to match our approximation to a fixed-order result to include dominant contributions to the cross-section and distributions in other areas of phase-space possible from the same Born-level diagram.

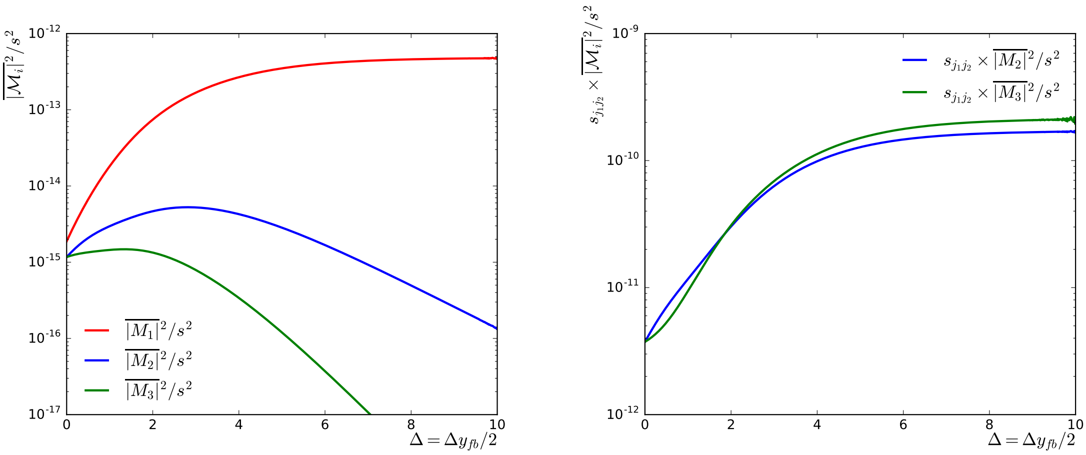

Figure 4.3: *These plots show that replacing one t-channel gluon in a FKL configuration introduces suppression by a factor of $s_{j_1j_2}$. $|\bar{M}_1|^2$ (red) corresponds to the Full FKL contribution, $qQ \to qgHQ$, whereas $|\bar{M}_2|^2$ (blue) and $|\bar{M}_3|^2$ (green) correspond to unordered emissions with a t-channel quark propagator, $qQ \to gqHQ$ and $qQ \to gHqQ$ respectively. The FKL contribution tends to a constant as the rapidity separation increases, while the non-FKL configurations are suppressed by a factor of $s_{j_1j_2}$ as demonstrated in the right plot.*
SOURCE: [7]

4.3 Unordered Contributions

As we alluded to in the previous section, any diagrams which have a quark line internally are regarded as subleading in the HEJ framework and the simplest available versions of these arrive in the form of unordered diagrams. This is where we take diagrams which simply drawn as Feynman diagrams would be equivalent to the leading FKL diagrams without any rapidity ordering stated in the final state. However, if any gluons which are emitted into the final state are more extremal than the quark leg in terms of rapidity, these are unordered in rapidity, and hence, in the `HEJ` framework, become unordered diagrams. An example of these can be found in Fig. 4.4.

These results were calculated prior to the work presented in this thesis [9]. There are two distinct classes here, namely, whether the W-boson is emitted from the same leg as the unordered gluon or from the opposite leg. In the case where the W is emitted from the opposite leg, we already have the relevant pieces from the pure jets

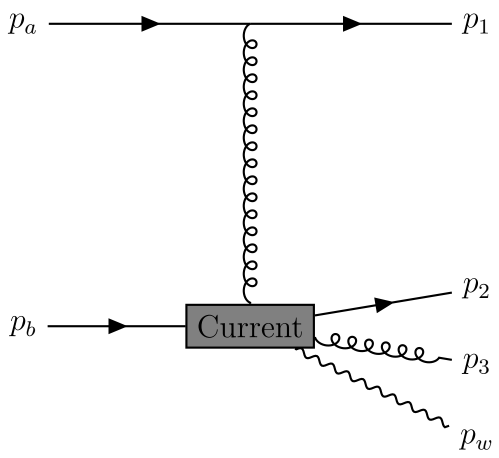

Figure 4.4: *A Depiction of the effective current or the unordered impact factor with a W emission in the effective vertex*

unordered case to be able to calculate the full HEJ matrix element approximation, where we simply contract the basic unordered piece with the basic FKL W boson current.

The more interesting[1] version of these subleading pieces requires a new piece, and that is an effective current in which the unordered gluon and the W-boson both reside. These were also calculated and presented in [9]. As such, we do not reproduce the derivation here and instead state the result directly. Which is, we find

$$\begin{aligned} j^{\mu}_{\text{Wuno}}(p_a,p_1,p_2,p_\ell,p_{\bar\ell}) = i\varepsilon_\nu(p_1)\ [\bar u_\ell \gamma_\rho v_{\bar\ell}]\Big(& T^1_{2i}T^d_{ia}(\tilde U_1^{\nu\mu\rho} - \tilde L^{\nu\mu\rho}) \\ & + T^d_{2i}T^1_{ia}(\tilde U_2^{\nu\mu\rho} + \tilde L^{\nu\mu\rho})\Big)\,, \end{aligned} \tag{4.3.1}$$

where the tensors $\tilde U_1^{\nu\mu\rho}$, $\tilde U_2^{\nu\mu\rho}$ and $\tilde L^{\nu\mu\rho}$ are the objects:

$$\begin{aligned} \tilde L^{\nu\mu\rho} = & \frac{1}{t_{aW2}}\left(\frac{[\bar u_2 \gamma_\sigma (\not p_a - \not p_W)\gamma^\rho u_a]}{t_{aW}} + \frac{[\bar u_2 \gamma^\rho (\not p_2 + \not p_W)\gamma_\sigma u_a]}{s_{2W}} \right) \\ & \times \left(\left(\frac{p_b^\nu}{s_{1b}} + \frac{p_3^\nu}{s_{13}} \right)(q_1 - p_1)^2 g^{\sigma\mu} + g^{\sigma\mu}(2q_1 - p_1)^\nu \right. \\ & \left. + g^{\mu\nu}(2p_1 - q_1)^\sigma - 2g^{\nu\sigma}p_1^\mu \right)\,. \end{aligned} \tag{4.3.2}$$

---

[1] read: painful

$$\begin{aligned}\tilde{U}_1^{\nu\mu\rho} =& \frac{[\bar{u}_2\gamma^\nu(\not{p}_2+\not{p}_1)\gamma^\mu(\not{p}_a-\not{p}_W)\gamma^\rho u_a]}{s_{12}t_{aW}} \\ &+ \frac{[\bar{u}_2\gamma^\nu(\not{p}_2+\not{p}_1)\gamma^\rho(\not{p}_2+\not{p}_1+\not{p}_W)\gamma^\mu u_a]}{s_{12}s_{12W}} \\ &+ \frac{[\bar{u}_2\gamma^\rho(\not{p}_2+\not{p}_W)\gamma^\nu(\not{p}_1+\not{p}_2+\not{p}_W)\gamma^\mu u_a]}{s_{2W}s_{12W}}.\end{aligned} \tag{4.3.3}$$

$$\begin{aligned}\tilde{U}_2^{\nu\mu\rho} =& \frac{[\bar{u}_2\gamma^\mu(\not{p}_a-\not{p}_W-\not{p}_1)\gamma^\nu(\not{p}_a-\not{p}_W)\gamma^\rho u_a]}{t_{aW1}t_{aW}} \\ &+ \frac{[\bar{u}_2\gamma^\mu(\not{p}_a-\not{p}_W-\not{p}_1)\gamma^\rho(\not{p}_a-\not{p}_1)\gamma^\nu u_a]}{t_{a1W}t_{a1}} \\ &+ \frac{[\bar{u}_2\gamma^\rho(\not{p}_2+\not{p}_W)\gamma^\mu(\not{p}_a-\not{p}_1)\gamma^\nu u_a]}{s_{2W}t_{a1}}.\end{aligned} \tag{4.3.4}$$

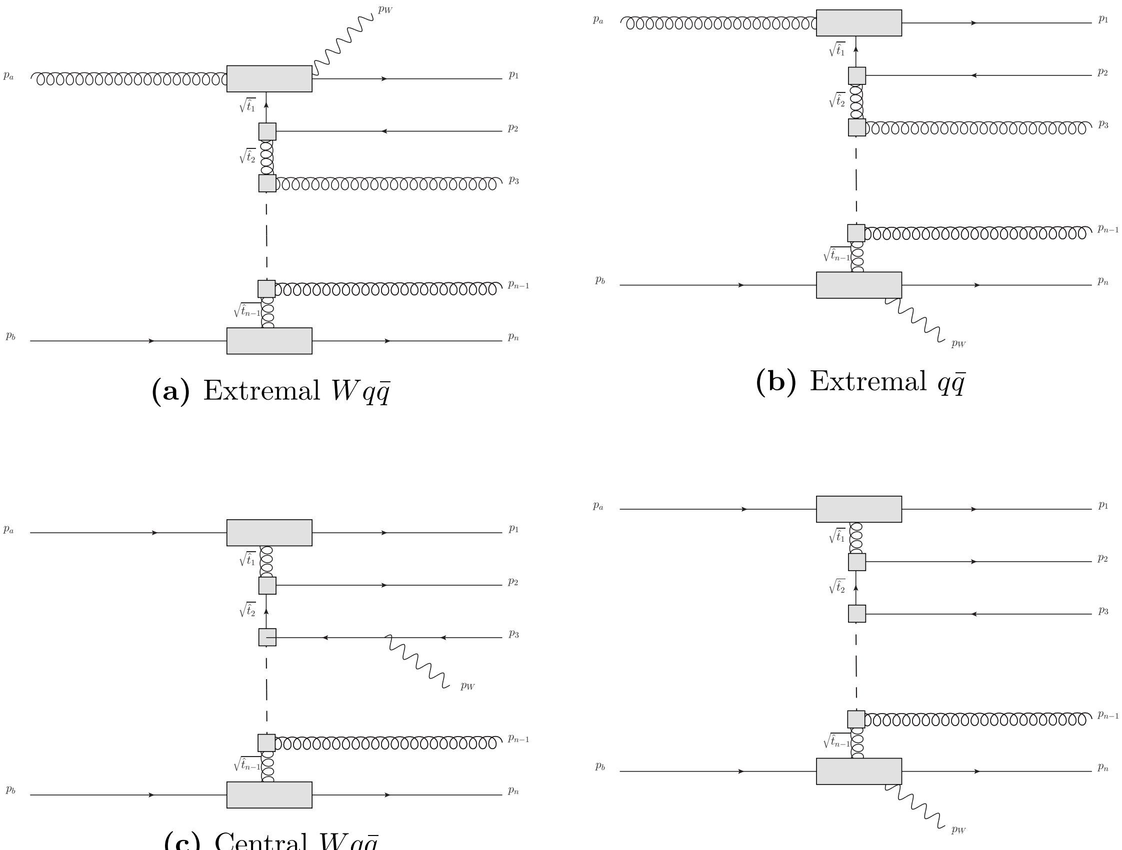

(a) Extremal $Wq\bar{q}$

(b) Extremal $q\bar{q}$

(c) Central $Wq\bar{q}$

(d) Central $q\bar{q}$

Figure 4.5: *These are the $q\bar{q}$ contributions to the NLL.*

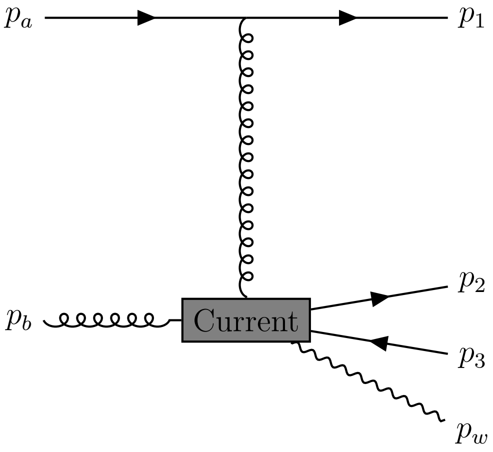

Figure 4.6: *A Depiction of the effective current or the $q\bar{q}$ impact factor with a W emission in the effective vertex*

4.4 Extremal $q\bar{q}$ Contributions

The extremal configurations are depicted in Figs. 4.5b and 4.5a. These configurations involve an incoming gluon state. Fortunately, this configuration is related by crossing symmetry to the unordered emission shown in Fig. 4.4 [9]. This symmetry remains valid even in the W+jets context.

As suggested by Fig. 4.5b, our objective is to factorise the effect of this $q\bar{q}$ emission into a new effective current at either end of the FKL chain. This is depicted in Fig. 4.6. This leads to the amplitude for the process $qg \to qQ\bar{Q}W$ being expressed as:

$$M_{qg\to qQ\bar{Q}W} \sim \frac{\langle 1|\mu|a\rangle\, Q^{\mu\nu\rho}\,(p_2,p_w,p_3,p_b)\,\varepsilon_\nu(p_b)\varepsilon^*_\rho(p_w)}{\hat{t}_1}\,, \tag{4.4.1}$$

where $Q^{\mu\nu}$ is this effective vertex which includes the emission of the quark/anti-quark pair. We also refer to this effective vertex as an *impact factor*. In the pure jets case there are 5 contributing diagrams for this type of process These are shown in Fig. 4.7. In the W+jets case, the number of contributing diagrams increases substantially, although the overall color structure remains unchanged.

Although there are significantly more diagrams than in the pure jets case, the number of diagrams is significantly limited since the W Boson, when emitted, changes the flavor of the particle it is emitted from. We begin by considering the addition of

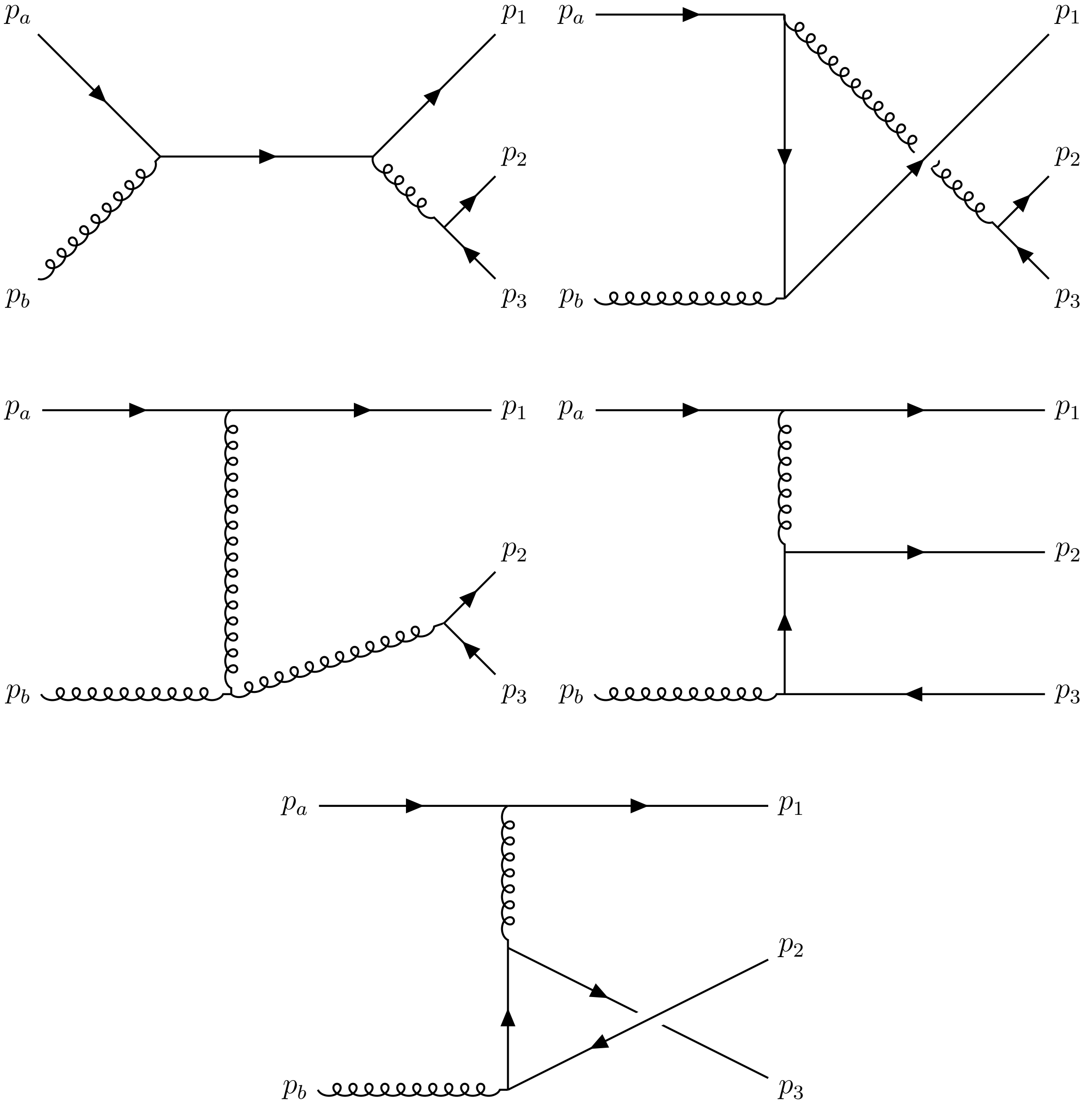

Figure 4.7: *These are the Pure Jet Extremal $q\bar{q}$ contributions. The trick we have to play here is to include all of the possible W-boson emissions to these diagrams to include the analogous W+Jets NLL processes to HEJ*

the W boson to the impact factor in Fig. 4.6. We will then consider the other cases where the W-boson can occur in the final state.

Let us consider the possible places for the emission of a W-boson in each of the cases in Fig. 4.7. The W-boson can be emitted from 12 places within these diagrams and contribute to the effective impact factor. All of these must be calculated separately. Fortunately, this complexity can be circumvented by noting a crossing symmetry with the W+jets unordered contribution [9]. Consequently, we obtain the following relation:

$$j^{d\,\mu}_{Wq\bar{q}'}(p_a, p_1, p_2, p_\ell, p_{\bar{\ell}}) = j^{d\,\mu}_{W\text{uno}}(p_1, p_a, p_2, p_\ell, p_{\bar{\ell}})\,. \tag{4.4.2}$$

4.5 Calculation of Central $q\bar{q}$ Contributions

This contribution arises only in processes involving four or more jets. Although its effect on the overall inclusive cross-section is limited, it constitutes an NLL contribution and must therefore be included, and as we will see in Chapter 5, the effect of this component on various distributions ends up being significant.

As with the extremal case, we aim to describe this process through an effective vertex representation, as depicted for one case in Fig. 4.11. In the pure jet case we have seven contributions to this effective vertex. These are depicted in Fig. 4.8. As in the extremal $q\bar{q}$ case, the number of contributing diagrams is significantly larger in the W+jets context. There are two cases which are distinct and can be recognised by the final state. Namely, the two distinct configurations where the W-boson is emitted from external quark legs or from the central $q\bar{q}$ quark line. We will first look at the emission from the external quark lines to assess whether this provides a reasonable approximation to the full matrix element. We will subsequently consider W-boson emission from the central $q\bar{q}$ quark line.

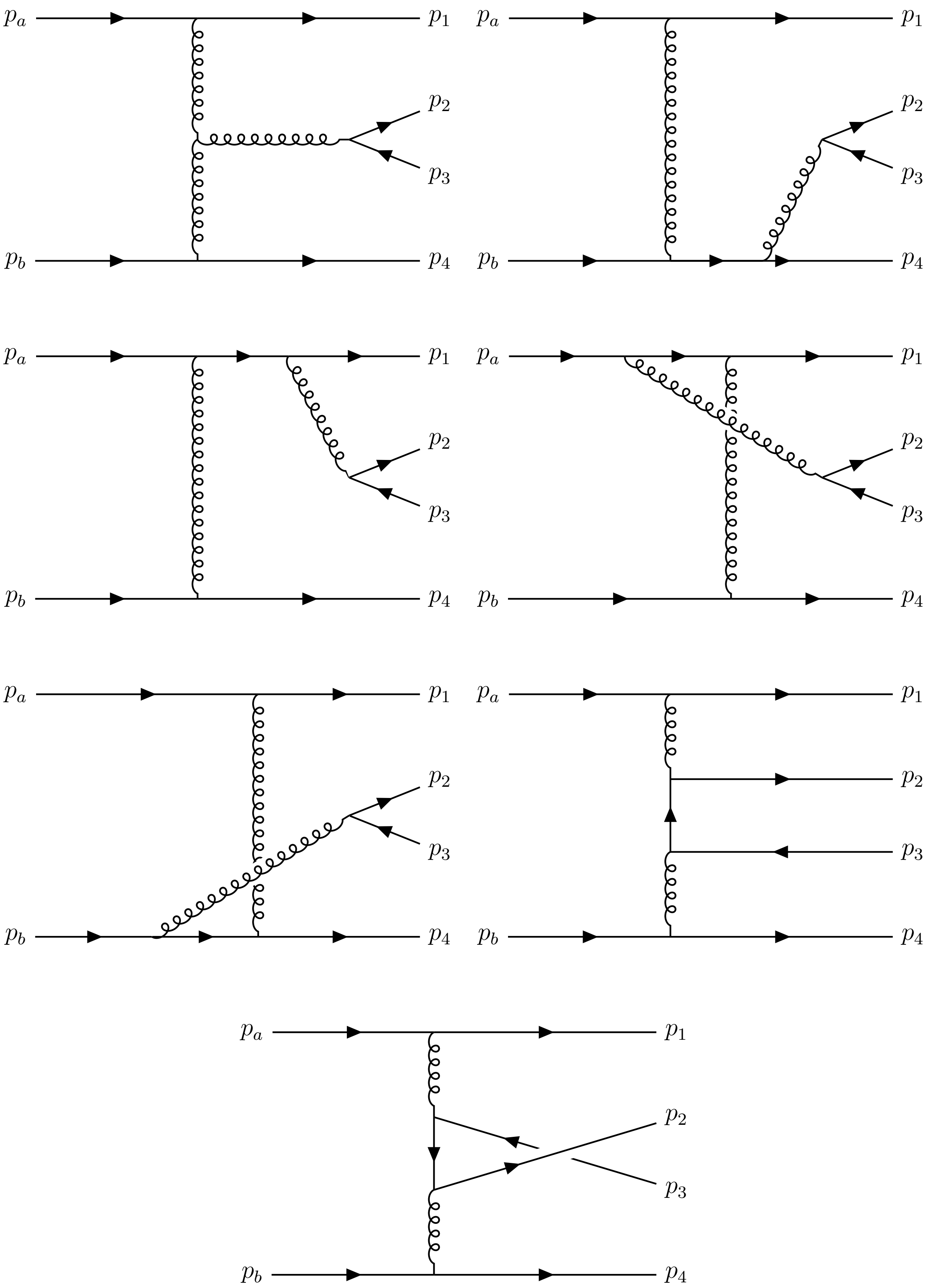

Figure 4.8: *These are the Pure Jet Central $q\bar{q}$ contributions. The trick we have to play here is to include all the possible W-boson emissions to these diagrams to include the analogous W+Jets NLL processes to HEJ*

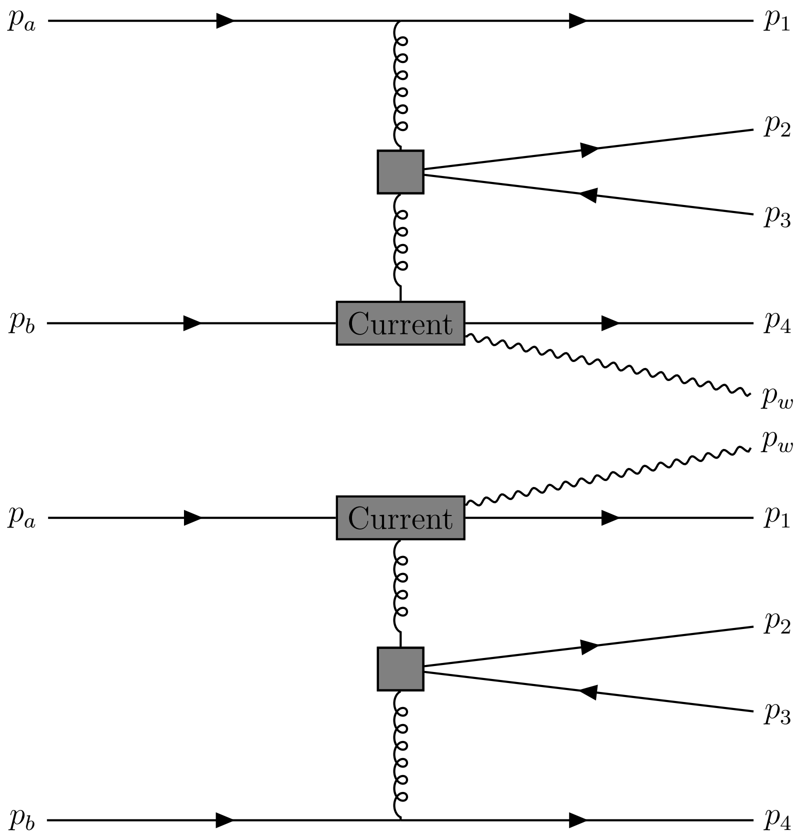

Figure 4.9: *The possible W-Emissions from the external lines with an effective vertex*

4.5.1 *W*-Boson Emission from the External Quark Lines

In this case, the number of possible contributions is limited, as the allowed structures are directly constrained by the final state. Indeed, due to the flavor changing nature of the W-boson interaction, the final-state flavor structure reveals whether the W-boson originated from an external leg. There will also be no interference here since the final state can only be reached by a particular interaction. This is not necessarily true in the central $q\bar{q}$ configuration

The effective diagram in this case is depicted in Fig. 4.9. This shows the two possible W-boson emissions from the external Quark Line. These are naturally related by exchanging the labels of the involved external particles. This symmetry offers potential simplification when implementing this process computationally. We want factorisation of the form:

$$M_{qq\to qQ\bar{Q}qW} \sim \frac{\langle 1|\mu\rho|a\rangle\, X^{de\,\mu\nu}_{\mathrm{cen}}\, \langle 4|\nu|b\rangle\, J_{\mathrm{Ex}\,\mu}}{\hat{t}_1\hat{t}_3}\,, \tag{4.5.1}$$

which would correspond to diagrams of the form depicted in Fig. 4.9. Let us first consider the effective external quark line currents in this case to obtain a building block for the amplitude, specifically the effective current $J_{\mathrm{Ex}\,\mu}$.

If we assume that the W-boson decays into two particles, A and B, we can derive the expression for this current directly using Feynman rules, this derivation can also be found in [9]:

$$\begin{aligned} J^{\mu}_{\mathrm{Ex}}(p_a, p_A, p_B, p_1) = \Bigg(& \frac{\bar{u}_1\gamma^{\nu}(\slashed{p}_1 + \slashed{p}_A + \slashed{p}_B)\gamma^{\mu}u_a}{t_{1AB}} \\ & + \frac{\bar{u}_1\gamma^{\mu}(\slashed{p}_a - \slashed{p}_A - \slashed{p}_B)\gamma^{\nu}u_a}{t_{aAB}}\Bigg)\,[\bar{u}_A\gamma_{\nu}u_B]\,. \end{aligned} \tag{4.5.2}$$

We can rewrite this in terms of manageable spinor-matrix-spinor pieces as:

$$\begin{aligned} J^{\mu}_{\mathrm{Ex}}(p_a, p_A, p_B, p_1) = \Big(& \tfrac{2p_1^{\nu}[\bar{u}_1\gamma^{\mu}P_a u_a] + [\bar{u}_1\gamma^{\nu}P_1 u_B][\bar{u}_B\gamma^{\mu}P_a u_a] + [\bar{u}_1\gamma^{\nu}P_1 u_A][\bar{u}_A\gamma^{\mu}P_a u_a]}{t_{1AB}} \\ & + \tfrac{2p_a^{\nu}[\bar{u}_1\gamma^{\mu}P_1 u_a] - [\bar{u}_1\gamma^{\mu}P_1 u_A][\bar{u}_A\gamma^{\nu}P_a u_a] - [\bar{u}_1\gamma^{\mu}P_1 u_B][\bar{u}_B\gamma^{\nu}P_a u_a]}{t_{aAB}}\Big) \\ & \times [\bar{u}_A\gamma_{\nu}P_A u_B]\,. \end{aligned} \tag{4.5.3}$$

This extremal current is then contracted with the known result for a central effective vertex that includes a $q\bar{q}$ pair. This was previously derived in [9], so we will just quote the result for the form that fits into Eq. (4.5.1) along with Eq. (4.5.2):

$$X^{de\,\mu\nu}_{\mathrm{cen}} = iC_2\left(X^{\mu\nu}_s + X^{\mu\nu}_6\right) - iC_3\left(X^{\mu\nu}_s + X^{\mu\nu}_7\right)\,, \tag{4.5.4}$$

where $C_2 = T^d_{2q}T^e_{q3}$ and $C_3 = T^e_{2q}T^d_{q3}$ are color factors, and the various tensors are defined by:

$$X_{6\,\mu\sigma} = \frac{\bar{u}_2\gamma_{\mu}(\slashed{q}_1 - \slashed{p}_2)\gamma_{\sigma}v_3}{(q_1 - p_2)^2}\,, \tag{4.5.5}$$

$$X_{7\,\mu\sigma} = \frac{\bar{u}_2\gamma_{\sigma}(\slashed{q}_1 - \slashed{p}_3)\gamma_{\mu}v_3}{(q_1 - p_3)^2}\,, \tag{4.5.6}$$

$$X^{\mu\nu}_s = \frac{1}{s_{23}}\left(g^{\mu\nu}X^{\sigma}_{sym} + X^{\mu\nu\sigma}_5\right)[\bar{u}_2\gamma_{\sigma}v_3]\,, \tag{4.5.7}$$

where

$$X_5^{\nu\lambda\sigma} = (q_1 + p_2 + p_3)^\lambda g^{\nu\sigma} + (q_3 - p_2 - p_3)^\nu g^{\lambda\sigma} - (q_1 + q_3)^\sigma g^{\nu\lambda}\,, \tag{4.5.8}$$

$$\begin{aligned} X_{sym}^\sigma =& p_a^\sigma \left(\frac{t_1}{s_{a2} + s_{a3}}\right) + p_1^\sigma \left(\frac{t_1}{s_{12} + s_{13}}\right) \\ &- p_b^\sigma \left(\frac{t_3}{s_{b2} + s_{b3}}\right) - p_4^\sigma \left(\frac{t_3}{s_{42} + s_{43}}\right)\,. \end{aligned} \tag{4.5.9}$$

While the results in Eqs. (4.5.2) and (4.5.4) existed within the HEJ formalism before the work in this thesis, implementing them both into a single `HEJ` ME of the form presented in Eq. (4.5.1) is novel, and as such, much work was carried out to validate the results when added into W+Jets predictions within HEJ. The validations are presented in Section 4.6.4.

4.5.2 *W*-boson Emission from the Central Quark Line

As in the extremal $q\bar{q}$ case, our goal is to factorise the currents and the W-boson emission. This will allow for the easy insertion into the HEJ formalism. We therefore search for an expression of the form:

$$M_{qq\to qQ\bar{Q}qW} \sim \frac{\langle 1|\mu|a\rangle\, X^{\mu\nu}\, \langle 4|\nu|b\rangle}{\hat{t}_1 \hat{t}_3}\,. \tag{4.5.10}$$

Let us consider the possible places for the emission of a W-boson in each of the cases in Fig. 4.8. The W-boson can be emitted from 16 places within these diagrams and contribute to the effective impact factor. All of these must be calculated separately. These contributions are relatively straightforward to compute, as the W-boson carries

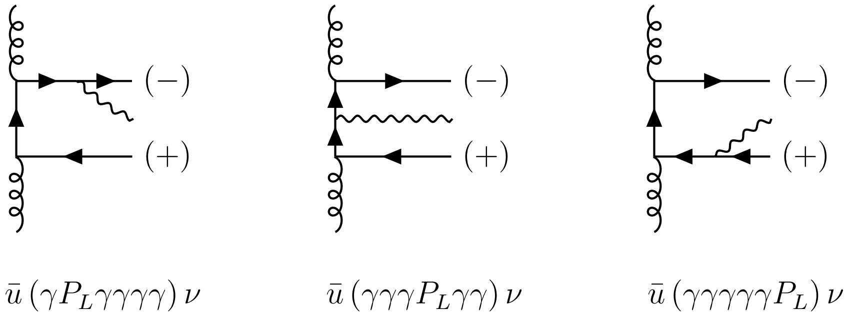

Figure 4.10: *The helicity of the central qqx line*

no color charge. There will also then be the case where we reuse the pure jet effective vertex for these contributions to the W+Jets NLL processes since the W-boson will be emitted separately.

There are 5 distinct diagrams where a gluon is emitted, splits into a $q\bar{q}$ pair which subsequently emits a W-boson. Since the W-boson can be emitted from either the quark or anti-quark line, this yields ten distinct contributions. Let us first have a look at the basic building block, J_V, which is a gluon splitting into a $q\bar{q}$ pair and the subsequent emission of a W. This building block takes into account both possible emission sites. The two possible contributing emission spots for the $q\bar{q}$ current are depicted in Fig. 4.12. When both of these contributions are realised the resulting current is:

$$\begin{aligned} J_V^\mu(p_2,p_A,p_B,p_3) = \frac{[\bar{u}_A\gamma_\nu u_B]}{8\left(p_W^2-m_W^2+im_W\Gamma_W\right)} \Bigg(& \frac{\bar{u}_2\gamma^\nu(\not{p}_2+\not{p}_A+\not{p}_B)\gamma^\mu u_3}{s_{2AB}} \\ & - \frac{\bar{u}_2\gamma^\mu(\not{p}_3+\not{p}_A+\not{p}_B)\gamma^\nu u_3}{s_{3AB}}\Bigg) \,. \end{aligned} \tag{4.5.11}$$

Note the inclusion of the W-boson propagator and the overall factor of 8, arising from two W-boson vertices contributing $2\sqrt{2}$ each. The relative minus sign between terms arises from the direction of momentum flow. We can rewrite this in terms of

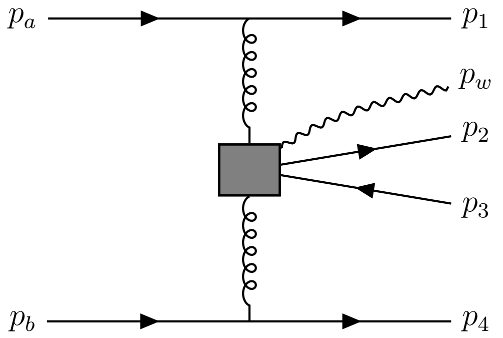

Figure 4.11: *This is the effective vertex in the central $q\bar{q}$ with a W-boson emission from the effective vertex.*

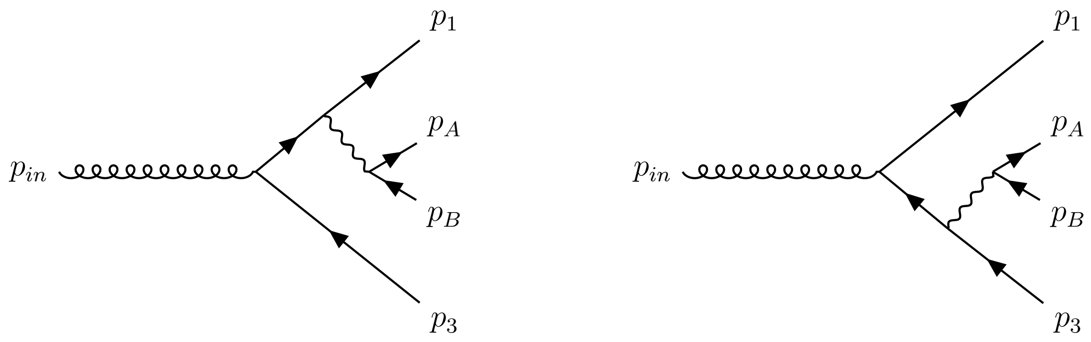

(a) W-boson Emission from Jet-2 **(b)** W-boson Emission from Jet-3

Figure 4.12: *The two possible $q\bar{q}$ current W-boson Emissions.*

manageable $\overline{\text{spinor}}$-matrix-spinor pieces as:

$$\begin{aligned} J_V^\mu(p_2,p_A,p_B,p_3) = \Big(& \tfrac{2p_2^\nu[\bar{u}_2\gamma^\mu P_3 v_3]+[\bar{u}_2\gamma^\nu P_2 u_B][\bar{u}_B\gamma^\mu P_3 v_3]+[\bar{u}_2\gamma^\nu P_2 u_A][\bar{u}_A\gamma^\mu P_3 v_3]}{s_{2AB}} \\ & -\tfrac{2p_3^\nu[\bar{u}_2\gamma^\mu P_2 v_3]+[\bar{u}_2\gamma^\mu P_2 u_A][\bar{u}_A\gamma^\nu P_3 v_3]+[\bar{u}_2\gamma^\mu P_2 u_B][\bar{u}_B\gamma^\nu P_3 v_3]}{s_{3AB}}\Big) \\ & \times \left[\bar{u}_A\gamma_\nu P_A u_B\right], \end{aligned} \tag{4.5.12}$$

where $s_{iAB} = (p_i + p_A + p_B)^2$ and P_x is the projection operator $P_\pm = (1 \pm \gamma_5)/2$ according to the helicity of particle x. The current is zero unless $P_2 = P_3$. Of course, we can contract this building block effective current with the analogous pure jet cases (and barring changing momenta in propagators) we have the more complicated Matrix element exactly already! So, explicitly, we have below calculated the corresponding diagrams:

For the first diagram, in Fig. 4.8 we can simply use the structure provided by the Pure Jets case and rather than contracting with a usual $\langle 2|\mu|3\rangle$ current, we instead contract with effective current above: J_V^σ. This construction assumes negligible interference between the two emission sites. Following Feynman rules, we arrive at the exact result for the amplitude as we have made no approximations:

$$\begin{aligned} iM_{3g} = & \frac{g_w^2 g_s^4\, T_{1a}^g T^{geg'} T_{4b}^{g'} T_{23}^e}{2\sqrt{2}\,\hat{t}_1 s_{23AB}\,\hat{t}_3}\Big[(q_1+p_2+p_3+p_A+p_B)^\lambda\, g^{\rho\mu} \\ & + (q_3-p_2-p_3-p_A-p_B)^\rho\, g^{\mu\lambda} - (q_1+q_3)^\mu\, g^{\rho\lambda}\Big] \\ & \times \Big[\bar{u}_1\gamma_\rho u_a\Big]\left[\bar{u}_4\gamma_\lambda u_b\right] J_{V\mu}(p_2,p_A,p_B,p_3)\,, \end{aligned} \tag{4.5.13}$$

where $q_1 = p_a - p_1 = q_3 + p_2 + p_3 + p_A + p_B$, $q_3 = p_4 - p_b = q_1 - p_2 - p_3 - p_A - p_B$ and $s_{i..j} = (p_i + .. + p_j)^2$. We have also assumed that the W is produced off shell and decays to two particles A and B. This accounts for all possible emissions of the W-boson from the three-gluon vertex in the diagram's t-channel. Next if we consider diagram 2 in Fig. 4.8, with our effective current building block we obtain:

$$\begin{aligned} iM_{\mathrm{l}_1} =& \frac{-ig_w^2 g_s^4\, T^e_{1q} T^g_{qa} T^e_{23} T^g_{4b}}{s_{23AB}\, \hat{t}_3} \left[\bar{u}_1 \gamma^\mu \frac{\left(\not{p}_a + \not{p}_b - \not{p}_4\right)}{(p_a + p_b - p_4)^2} \gamma^\rho u_a \right] \\ & \times J_{V\mu}(p_2, p_A, p_B, p_3) \left[\bar{u}_4 \gamma_\rho u_b\right] . \end{aligned} \tag{4.5.14}$$

As might be expected due to the lack of t-channel factorisation this is not in the form we desired as in Eq. (4.5.10). As such we need to make some approximations. We consider the quark current $[\bar{u}_1 \;...\; u_a]$. After expansion of the current with the use of the completeness relation:

$$\left[\bar{u}_1 \gamma^\mu \frac{\left(\not{p}_a + \not{p}_b - \not{p}_4\right)}{(p_a + p_b - p_4)^2} \gamma^\rho u_a \right] = \frac{\langle 1|\mu|1\rangle\langle 1|\rho|a\rangle + \langle 1|\mu|2\rangle\langle 2|\rho|a\rangle + \langle 1|\mu|A\rangle\langle A|\rho|a\rangle + \langle 1|\mu|B\rangle\langle B|\rho|a\rangle + \langle 1|\mu|3\rangle\langle 3|\rho|a\rangle}{s_{ab} - s_{a4} - s_{b4}} . \tag{4.5.15}$$

We now proceed to making some scaling arguments which shall show the dominant term in the process. Consider the two current expansions in Eq. (4.5.12) and the Eq. (4.5.15). These come about from the completeness relations. This is quite simple, the dominant term in Eq. (4.5.15) is the first term. This is apparent after the contraction with the current $\langle 4|\rho|b\rangle$. Under this scenario, we immediately observe the emergence of the contraction $\langle 1|\rho|a\rangle\langle 4|\rho|b\rangle$. This, in the approximation that $p_1 \sim p_a$ and $p_4 \sim p_b$ leads to the scaling of this term with a factor of $\sqrt{s_{14}}$. All remaining terms exhibit less favourable scaling behaviour. Taking this as the only relevant term, we can then get the approximation for the amplitude as:

$$iM_{\mathrm{l}_1} = \frac{-ig_w^2 g_s^4\, T^e_{1q} T^g_{qa} T^e_{23} T^g_{4b}}{s_{23AB}\, \hat{t}_3 (s_{123AB})} \langle 1|\rho|a\rangle \langle 4|\rho|b\rangle (2p_1^\mu) J_{V\mu} . \tag{4.5.16}$$

As we want to express this as in the form of Eq. (4.5.10) we need to rearrange (mostly uncontract the extremal currents):

$$X^{\mu\nu} = \frac{g^{\mu\nu}}{s_{23AB}(s_{123AB})} (p_1^\rho) J_{V\rho} , \tag{4.5.17}$$

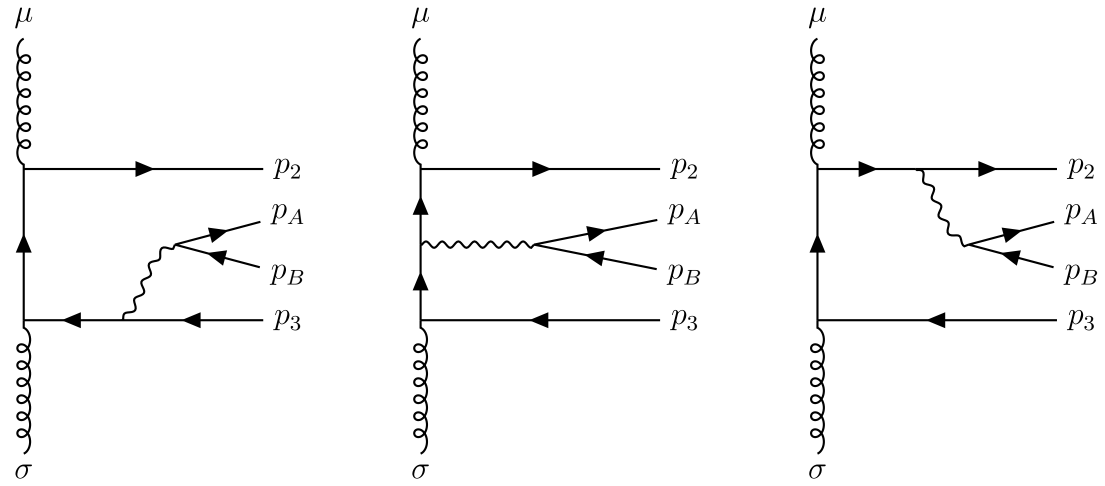

Figure 4.13: *These are the possible emission sites for the W-boson when emitted from this central $q\bar{q}$ arrangement.*

up to color factors. We now need to consider the next diagram in Fig. 4.8. This diagram is of a very similar structure to the last one. The key difference between these two cases is that the gluon initiating the $q\bar{q}$ pair originates from leg-4 rather than leg-1. As such without writing the derivation we simply state the result:

$$iM_{1_4} = \frac{-i g_w^2 g_s^4 \, T^g_{1a} T^e_{4q} T^g_{qb} T^e_{23}}{s_{23AB} \, \hat{t}_1(s_{234AB})} \langle 1|\rho|a\rangle \langle 4|\rho|b\rangle (2p_4^\mu) J_{V\mu} \,. \tag{4.5.18}$$

Notably the color factors have changed as the gluon now originates from a different leg, resulting in a structural analogue to Eq. (4.5.17) yielding an expression for $X^{\mu\nu}$ that now depends on p_4^μ rather than p_1^μ. There are another two diagrams with a similar form, which rather than derive we are simply going to state the result of the rearrangement:

$$iM_{1_a} = \frac{-i g_w^2 g_s^4 \, T^g_{1q} T^e_{qa} T^e_{23} T^g_{4b}}{s_{23AB} \, \hat{t}_3(s_{a23AB})} \langle 1|\rho|a\rangle \langle 4|\rho|b\rangle * 2p_a^\mu J_{V\mu} \,. \tag{4.5.19}$$

As in the previous case, changing the location of the gluon emission alters the color structure of the amplitude. There is one final diagram with this exact form in the Fig. 4.8. This corresponds to the emission of the Gluon which splits into a $q\bar{q}$ pair from leg-b.

$$iM_{1_b} = \frac{-i g_w^2 g_s^4 \, T^g_{1a} T^g_{4q} T^e_{qb} T^e_{23}}{s_{23AB} \, \hat{t}_1(s_{b23AB})} \langle 1|\rho|a\rangle \langle 4|\rho|b\rangle * 2p_b^\mu J_{V\mu} \,. \tag{4.5.20}$$

At this point, it is advantageous to invoke the high-energy limit, where $p_1 \sim p_a$ and $p_4 \sim p_b$. We will use these to combine the contributions from the diagrams where the gluon which splits into the $q\bar{q}$ pair is emitted from the same quark line. As such, we will combine the contributions in the manner: $i(M_{1_a} + M_{1_1})$ and $i(M_{1_b} + M_{1_4})$ which gives us the expressions:

$$i(M_{1a}) = i(M_{1_a} + M_{1_1}) = \frac{g_w^2 g_s^4 C_1}{s_{23AB}\,\hat{t}_3(s_{123AB})} \langle 1|\rho|a\rangle\langle 4|\rho|b\rangle * 2p_1^\mu J_{V\mu}\,, \tag{4.5.21}$$

where C_1 is given by:

$$\begin{aligned} C_1 &= T^e_{1q}T^g_{qa}T^e_{23}T^g_{4b} - T^g_{1q}T^e_{qa}T^e_{23}T^g_{4b} \\ &= f^{egc}T^c_{1a}T^e_{23}T^g_{4b}\,. \end{aligned} \tag{4.5.22}$$

We then proceed to do this with the other extremal leg:

$$i(M_{4b}) = i(M_{1_4} + M_{1_b}) = \frac{-ig_w^2 g_s^4 C_1}{s_{23AB}\,\hat{t}_1(s_{234AB})} \langle 1|\rho|a\rangle\langle 4|\rho|b\rangle * 2p_4^\mu J_{V\mu}\,. \tag{4.5.23}$$

These two contributions correspond to an effective vertex contribution as (again, up to color factors):

$$X^{\mu\nu}_{1a} = \frac{g^{\mu\nu} g_w^2 g_s^4}{s_{23AB}(s_{123AB})\hat{t_3}}(2p_1^\rho)J_{V\rho}\,, \tag{4.5.24}$$

$$X^{\mu\nu}_{4b} = \frac{-g^{\mu\nu} g_w^2 g_s^4}{s_{23AB}(s_{234AB})\hat{t1}}(2p_4^\rho)J_{V\rho}\,. \tag{4.5.25}$$

This accounts for five of the original seven diagrams in the pure jets case, and so we are left with the final two diagrams which both have central $q\bar{q}$ production. Both diagrams feature quark propagators that are t-channel factorised and can therefore be expressed explicitly using Feynman rules in the desired form. In both cases we have 3 possible emission sites. We will model this with the use of an effective vertex once again. The first of these diagrams in the pure jets case gives:

$$iM_{tq\bar{q}} = \frac{ig_s^4\, T^g_{1a}T^g_{2q}T^e_{q3}T^e_{4b}}{2\hat{t}_1(p_a - p_1 - p_2)^2\hat{t}_3} \langle 1|\mu|a\rangle\langle 4|\sigma|b\rangle[\bar{u}_2\gamma_\mu(\not{p}_a - \not{p}_1 - \not{p}_2)\gamma_\sigma v_3]\,. \tag{4.5.26}$$

We need to consider the possibility of the W-boson emission from anywhere within the central quark line. This gives us three possible emission sites. These are depicted in

Fig. 4.13. As these contributions are explicitly t-channel factorised, no approximation is required to cast them into the desired form. We need to use all three possibilities in our effective vertex, however. We will list these in order, starting with the W emitted from the quark (p2) leg:

$$X_1^{\mu\nu} = -\frac{\langle A|\sigma|B\rangle[\bar{u}_2\gamma^\sigma(\slashed{p}_2+\slashed{p}_A+\slashed{p}_B)\gamma^\mu(\slashed{q}_1-\slashed{p}_2-\slashed{p}_A-\slashed{p}_B)\gamma^\nu v_3]}{(p_2+p_A+p_B)^2(q_1-p_2-p_A-p_B)^2 8(p_W^2-m_W^2+im_W\Gamma_W)} \tag{4.5.27}$$

$$X_2^{\mu\nu} = \frac{\langle A|\sigma|B\rangle[\bar{u}_2\gamma^\mu(\slashed{q}_1-\slashed{p}_2)\gamma^\sigma(\slashed{q}_1-\slashed{p}_2-\slashed{p}_A-\slashed{p}_B)\gamma^\nu v_3]}{(q_1-p_2)^2(q_1-p_2-p_A-p_B)^2 8(p_W^2-m_W^2+im_W\Gamma_W)} \tag{4.5.28}$$

$$X_3^{\mu\nu} = \frac{\langle A|\sigma|B\rangle[\bar{u}_2\gamma^\mu(\slashed{q}_1-\slashed{p}_2)\gamma^\nu(\slashed{p}_3+\slashed{p}_A+\slashed{p}_B)\gamma^\sigma v_3]}{(q_1-p_2)^2(p_3+p_A+p_B)^2 8(p_W^2-m_W^2+im_W\Gamma_W)} . \tag{4.5.29}$$

The first term includes a minus sign, resulting from the propagator having momentum flow opposite to the fermion flow. Note that the index μ corresponds to the gluon with momenta q_1, the index ν corresponds to the gluon with momenta q_3 and the index σ corresponds to the emission of the W. A potential simplification exists: $q_1 - p_2 - p_A - p_B = q_3 + p_3$; however, if this was actually used within the code, this would invalidate the gauge invariance, since momentum would then only be conserved in the hard process, and resummation would no longer be valid.

These contributions can then be combined to construct the effective current. Notably, their structure is already factorised in the t-channel. So we simply add these together to get the effective vertex for the uncrossed contribution.

$$\begin{aligned} X_{\text{unc}}^{\mu\nu} = \frac{\langle A|\sigma|B\rangle}{8(p_W^2-m_W^2+im_W\Gamma_W)}\bar{u}_2 \Bigg[&-\frac{\gamma^\sigma(\slashed{p}_2+\slashed{p}_A+\slashed{p}_B)\gamma^\mu(\slashed{q}_3+\slashed{p}_3)\gamma^\nu}{(s_{2AB})(t_{unc_2})} \\ &+ \frac{\gamma^\mu(\slashed{q}_1-\slashed{p}_2)\gamma^\sigma(\slashed{q}_3+\slashed{p}_3)\gamma^\nu}{(t_{unc_1})(t_{unc_2})} \\ &+ \frac{\gamma^\mu(\slashed{q}_1-\slashed{p}_2)\gamma^\nu(\slashed{p}_3+\slashed{p}_A+\slashed{p}_B)\gamma^\sigma}{(t_{unc_1})(s_{3AB})}\Bigg] v_3 , \end{aligned} \tag{4.5.30}$$

where $t_{unc_1} = (q_1 - p_2)^2$ and $t_{unc_2} = (q_3 + p_3)^2$. We now turn to the remaining diagram of this class, which involves crossed quark lines. Again, there are three possible emission sites which are depicted in Fig. 4.14 and these give the results as below:

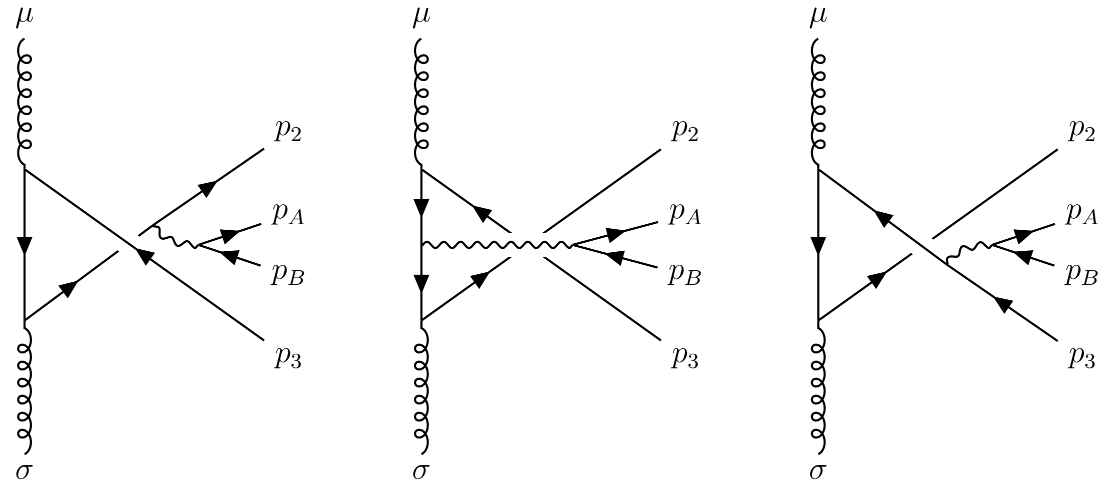

Figure 4.14: *These are the possible emission sites for the W-boson when emitted from this central $q\bar{q}$ arrangement.*

$$Z_1^{\mu\nu} = -\frac{\langle A|\sigma|B\rangle[\bar{u}_2\gamma^\nu(\not{q}_1 - \not{p}_3 - \not{p}_A - \not{p}_B)\gamma^\mu(\not{p}_3 + \not{p}_A + \not{p}_B)\gamma^\sigma v_3]}{(q_1 - p_3 - p_A - p_B)^2(p_3 + p_A + p_B)^2 8(p_W^2 - m_W^2 + im_W\Gamma_W)} \tag{4.5.31}$$

$$Z_2^{\mu\nu} = \frac{\langle A|\sigma|B\rangle[\bar{u}_2\gamma^\nu(\not{q}_1 - \not{p}_3 - \not{p}_A - \not{p}_B)\gamma^\sigma(\not{q}_1 - \not{p}_3)\gamma^\mu v_3]}{(q_1 - p_3 - p_A - p_B)^2(q_1 - p_3)^2 8(p_W^2 - m_W^2 + im_W\Gamma_W)} \tag{4.5.32}$$

$$Z_3^{\mu\nu} = \frac{\langle A|\sigma|B\rangle[\bar{u}_2\gamma^\sigma(\not{p}_2 + \not{p}_A + \not{p}_B)\gamma^\nu(\not{q}_1 - \not{p}_3)\gamma^\mu v_3]}{(p_2 + p_A + p_B)^2(q_1 - p_3)^2 8(p_W^2 - m_W^2 + im_W\Gamma_W)}\,. \tag{4.5.33}$$

Note the first term here has a minus sign due to the propagator with momentum flow against the fermion flow. Note that the index μ corresponds to the gluon with momenta q_1, the index ν corresponds to the gluon with momenta q_3 and the index σ corresponds to the emission of the W. We also note a possible simplification: $q_1 - p_3 - p_A - p_B = q_3 + p_2$.

All the above can then be added together to form the effective current itself. Their structure is inherently t-channel factorised. Thus, we simply sum them to construct the effective vertex corresponding to the crossed contribution.

$$\begin{aligned} Z_{cross}^{\mu\nu} = \frac{\langle A|\sigma|B\rangle}{8(p_W^2 - m_W^2 + im_W\Gamma_W)}\bar{u}_2 \Bigg[&-\frac{\gamma^\nu(\not{q}_3 + \not{p}_2)\gamma^\mu(\not{p}_3 + \not{p}_A + \not{p}_B)\gamma^\sigma}{(t_{cro_1})(s_{3AB})} \\ &+ \frac{\gamma^\nu(\not{q}_3 + \not{p}_2)\gamma^\sigma(\not{q}_1 - \not{p}_3)\gamma^\mu}{(t_{cro_1})(t_{cro_2})} \\ &+ \frac{\gamma^\sigma(\not{p}_2 + \not{p}_A + \not{p}_B)\gamma^\nu(\not{q}_1 - \not{p}_3)\gamma^\mu}{(s_{2AB})(t_{cro_2})} \Bigg] v_3\,, \end{aligned} \tag{4.5.34}$$

where $t_{cro_1} = (q_3 + p_2)^2$ and $t_{cro_2} = (q_1 - p_3)^2$. We now have everything we need necessarily to form an expression for $X^{\mu\nu}$ as depicted by Fig. 4.11. This can be done by combining all the contributions from above into one single effective vertex. We begin by revisiting the extremal leg gluon emissions to finalise this component:

$$\begin{aligned} X^{\mu\nu}_{1a} &= \frac{g^{\mu\nu}}{s_{23AB}(s_{123AB})\hat{t_3}}(2p_1^\sigma)J_{V\sigma}\,, && (4.5.35)\\ X^{\mu\nu}_{4b} &= \frac{-g^{\mu\nu}}{s_{23AB}(s_{234AB})\hat{t_1}}(2p_4^\sigma)J_{V\sigma}\,. && (4.5.36) \end{aligned}$$

Earlier we noted that if we looked into the high-energy limit with the approximations $p_1 \sim p_a$ and $p_4 \sim p_b$ we could simplify this arrangement. However, we now opt to symmetrise this contribution and explicitly reintroduce both p_a and p_b:

$$\begin{aligned} X^{\mu\nu\sigma}_{1a} &= \frac{g^{\mu\nu}}{s_{23AB}\hat{t_3}}\left(\frac{p_a^\sigma}{(s_{a23AB})} + \frac{p_1^\sigma}{(s_{123AB})}\right)\,, && (4.5.37)\\ X^{\mu\nu\sigma}_{4b} &= \frac{-g^{\mu\nu}}{s_{23AB}\hat{t_1}}\left(\frac{p_b^\sigma}{(s_{23bAB})} + \frac{p_4^\sigma}{(s_{234AB})}\right)\,. && (4.5.38) \end{aligned}$$

We first observe that an overall minus sign appears between the crossed and uncrossed $q\bar{q}$ contributions. We also note that we only have one $\hat{t}$ denominator in each of the two extremal leg cases. This will mean we need to multiply X_{1a} and X_{4b} by $\hat{t_1}$ and $\hat{t_3}$ respectively when factorising these denominators out of the overall effective vertex form. Now, we combine: Eqs. (4.5.37), (4.5.38), (4.5.30) and (4.5.34):

$$\begin{aligned} X^{\mu\nu}_{3g} = \frac{T^{geg'}T^e_{23}}{\hat{t}_1 s_{23AB}\,\hat{t}_3}\Bigg[& (q_1 + p_2 + p_3 + p_A + p_B)^\nu\, g^{\mu\sigma} \\ & + (q_3 - p_2 - p_3 - p_A - p_B)^\mu\, g^{\sigma\nu} \\ & - (q_1 + q_3)^\sigma\, g^{\mu\nu}\Bigg] J_{\mathrm{V}\sigma}(p_2, p_A, p_B, p_3)\,, \end{aligned} \qquad (4.5.39)$$

$$\begin{aligned} X^{\mu\nu}_{Unc} = \frac{\langle A|\sigma|B\rangle}{\hat{t}_1\hat{t}_3}\bar{u}_2\Bigg[& -\frac{\gamma^\sigma(\not{p}_2 + \not{p}_A + \not{p}_B)\gamma^\mu(\not{q}_3 + \not{p}_3)\gamma^\nu}{(s_{2AB})(t_{unc_2})} \\ & + \frac{\gamma^\mu(\not{q}_1 - \not{p}_2)\gamma^\sigma(\not{q}_3 + \not{p}_3)\gamma^\nu}{(t_{unc_1})(t_{unc_2})} \\ & + \frac{\gamma^\mu(\not{q}_1 - \not{p}_2)\gamma^\nu(\not{p}_3 + \not{p}_A + \not{p}_B)\gamma^\sigma}{(t_{unc_1})(s_{3AB})}\Bigg] v_3\,, \end{aligned} \qquad (4.5.40)$$

$$
\begin{aligned}
X^{\mu\nu}_{Cro} = \frac{\langle A|\sigma|B\rangle}{\hat{t_1}\hat{t_3}}\bar{u}_2 \Bigg[&-\frac{\gamma^\nu(\not{q}_3+\not{p}_2)\gamma^\mu(\not{p}_3+\not{p}_A+\not{p}_B)\gamma^\sigma}{(t_{cro_1})(s_{3AB})} \\
&+\frac{\gamma^\nu(\not{q}_3+\not{p}_2)\gamma^\sigma(\not{q}_1-\not{p}_3)\gamma^\mu}{(t_{cro_1})(t_{cro_2})} \\
&+\frac{\gamma^\sigma(\not{p}_2+\not{p}_A+\not{p}_B)\gamma^\nu(\not{q}_1-\not{p}_3)\gamma^\mu}{(s_{2AB})(t_{cro_2})}\Bigg] v_3\,.
\end{aligned}
\tag{4.5.41}
$$

We proceed by factoring out common terms, namely the couplings, the W-boson propagator, and the t-channel propagators: $\frac{g_w^2 g_s^4}{8(p_W^2-m_W^2-m_W\Gamma_W)\hat{t_1}\hat{t_3}}$. We then inspect the color factors to determine how these terms combine: In the end, we arrive at

$$
\begin{aligned}
V^{\mu\nu}_{\text{Eff}} =&\frac{C_1}{s_{23AB}}\left(X^{\mu\nu\sigma}_{1a}\hat{t_1} - X^{\mu\nu\sigma}_{4b}\hat{t_3} + V^{\mu\nu\sigma}_{3g}\right) J_{\text{V}\sigma}(p_2,p_A,p_B,p_3) \\
&+ iC_2 X^{\mu\nu}_{Unc} - iC_3 X^{\mu\nu}_{Cro}\,,
\end{aligned}
\tag{4.5.42}
$$

Note the relative minus sign between the uncrossed and crossed contributions, arising from the presence of crossed fermion lines, and the minus between the 1a and 4b extremal leg contributions due to momentum flow. There is also an extra factor of $\hat{t_1}$ multiplying the 1a leg term as this is not present in the denominator. Also, there is an extra factor $\hat{t_3}$ multiplying the 4b leg term for similar reasons. We have defined the following expressions:

$$
\begin{aligned}
C_1 =&T^e_{1q}T^g_{qa}T^e_{23}T^g_{4b} - T^g_{1q}T^e_{qa}T^e_{23}T^g_{4b} = f^{egc}T^c_{1a}T^e_{23}T^g_{4b}\,, \\
C_2 =&T^g_{1a}T^g_{2q}T^{g'}_{q3}T^{g'}_{4b}\,, \\
C_3 =&T^g_{1a}T^{g'}_{2q}T^g_{q3}T^{g'}_{4b}\,.
\end{aligned}
\tag{4.5.43}
$$

Now we have our desired form:

$$
iM = \frac{g_w^2 g_s^4}{8(p_W^2-m_W^2+im_W\Gamma_W)}\frac{\langle 1|\mu|a\rangle V^{\mu\nu}_{\text{Eff}}\langle 4|\nu|b\rangle}{\hat{t_1}\hat{t_3}}\,. \tag{4.5.44}
$$

4.5.3 Choosing the *W*-boson Emission Site

We now provide several additional remarks regarding W-boson emission. First, if both incoming legs are up-type quarks, any W^--boson emission must originate from the central $q\bar{q}$ effective vertex. Additionally, in the case of one up-type and one

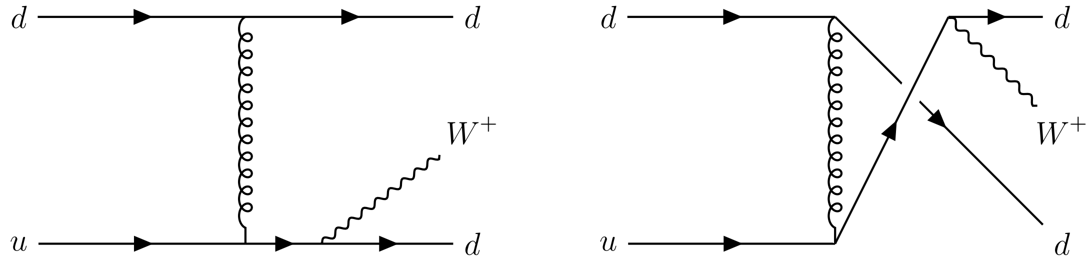

Figure 4.15: *In this case of W Emission we will have possible interference. This will (at least to begin) be assumed negligible.*

down-type incoming quark, the W-boson may be emitted either from the quark leg matching its charge (i.e., up emits W^+, down emits W^-), or from the central vertex.

We do not account for interference effects arising from W-boson emission that produces indistinguishable final states, such as the example illustrated in Fig. 4.15. Because of the above constraints we will consider the W-boson emission from the effective impact factor and vertex first.

Such interference has also been neglected in other implementations within `HEJ`. The Z+Jets case interference is slightly less trivial because the actual origin of the Z-boson emission is much less clear. The interference caused in that case must not be ignored.

We assign W-boson emission to the leg closest in rapidity to the W itself that is a valid emission site. Specifically, we emit the W-boson from the quark leg with minimal rapidity separation from it. This is due to the observed fact that the W-boson emissions appear to have a normal distribution of rapidity around the rapidity of the particle which first emits it (even if the width of said distribution is a couple units of rapidity).

4.6 Matrix Element Validation: HEJ_Explorer

All processes have always been validated very explicitly using multiple methodologies before their inclusion within `HEJ`. One basic verification we performed is to check our calculations against known solutions. For the case of `HEJ`, one such explicit check has always been through comparison explorer plots, such as shown in Fig. 2.3.

The basic premise in `HEJ` is to compute the matrix element with the t-channel pole explicitly isolated before applying the Lipatov ansatz and resumming real emissions. In lots of cases, this calculation requires no approximation, and the resulting matrix element is exact. In other cases, there are a few approximations made. Either way, we expect that the result of the approximation within `HEJ` will be correct in the high energy limit. Hence, we 'explore' a phase-space slice for the `HEJ` matrix element and compare it with a fixed-order (exact) LO calculation of the same object.

Within `HEJ1`, this comparison was exceptionally easy, since automatically generated standalone `Madgraph5` [74] matrix elements were a part of the `HEJ` code-base. Following the decision to move to using fixed-order event files as input, which doubles up as our matching methodology, we no longer require these fixed-order matrix elements to be a part of the code. This has several advantages, notably reducing the number of dependencies required by the `HEJ` code and there is far less bloat. The downside is that there was no obvious candidate for how to explicitly check these matrix elements in an automated way. As such, I developed a program using C++, taking advantage of the new ability of `HEJ` to be used as a library which allowed such comparisons to take place.

The end result was a robust program which allowed for an extra check which was not possible (or necessary before). Specifically, it was now possible to input a test event, and ensure that the output of `HEJ` just of the hard process approximation calculation was correct in comparison to predictions made by the same fixed-order generators which were used within `HEJ1`. This means that we can see that the input events are indeed correctly classified, and then also correctly calculated up to the stage that they can be verified through comparison to an external program.

This validation procedure has been retroactively applied across all processes in `HEJ` to ensure that the matrix elements produced by `HEJ2` are firstly, the same as those produced by `HEJ1`, but also that they still agree with other external predictions. This when combined with the other continuous integration checks on the code provides a fairly safe understanding that the predictions made within `HEJ2` are reliable.

4.6.1 Explorer Plot of Unordered Processes

Although the unordered subleading channel was derived in earlier work, it was never included in any published study. This is also true of the Extremal $q\bar{q}$ process type. As such, although we have not included their derivations here, it should be made clear that extensive verification steps have been undertaken to ensure the validity of these subleading pieces also. To avoid overcomplicating the current validation discussion, we simply include one channel of the explorer plots for both the unordered and extremal $q\bar{q}$ process types. The following phase-space point was used for both of these investigations:

$$\begin{aligned}
p_1 =& (p_T \cosh(\Delta), p_T \cos(\phi_1), p_T \sin(\phi_1), p_T \sinh(\Delta)) \\
p_2 =& (p_T, p_T, 0, 0) \\
p_{\bar{l}} =& p_e = (p_{eT} \cosh(y_e), p_{eT} \cos(\phi_e), p_{eT} \sin(\phi_e), p_{eT} \sinh(y_e)) \\
p_l =& p_{\nu_e} = (p_{\nu T} \cosh(y_\nu), p_{\nu T} \cos(\phi_\nu), p_{\nu T} \sin(\phi_\nu), p_{\nu T} \sinh(y_\nu)) \\
p_3 =& (|\vec{p}_{3T}| \cosh(-\Delta), |\vec{p}_{3T}| \cos(\phi_3), |\vec{p}_{3T}| \sin(\phi_3), |\vec{p}_{3T}| \sinh(-\Delta)) \\
p_a =& (\tfrac{x_a\sqrt{\hat{s}}}{2}, 0, 0, \tfrac{x_a\sqrt{\hat{s}}}{2}) \\
p_b =& (\tfrac{x_b\sqrt{\hat{s}}}{2}, 0, 0, \tfrac{-x_b\sqrt{\hat{s}}}{2})\,,
\end{aligned} \tag{4.6.1}$$

where $p_T = p_{eT} = 40GeV$, $p_{\nu T} = \frac{m_W^2}{2p_{eT}(\cosh(y_e - y_\nu) - \cos(\phi_e - \phi_\nu))}$, $y_e = y_\nu = \Delta$, $\phi_1 = \frac{2\pi}{3}$, $\phi_e = \frac{\pi}{2}$, $\phi_\nu = -\frac{\pi}{2}$ are parameters chosen to ensure our partons when exploring phase-space do not go too soft. And where our final momentum, $\vec{p}_{3T} =$

$(|\vec{p}_{3T}|\cos(\phi_3), \vec{p}_{3T}\sin(\phi_3))$ is set through transverse momentum conservation. Longitudinal momentum conservation is set thanks to:

$$x_a = \sum_i \tfrac{p_{iT}}{\sqrt{\hat{s}}} e^{y_i} \,,$$

$$x_b = \sum_i \tfrac{p_{iT}}{\sqrt{\hat{s}}} e^{-y_i} \,,$$

where the index i refers to the outgoing particles. Naturally, numerous additional checks must be performed to ensure that the matrix elements are correct for all differing phase-spaces, and these were performed. In particular, it must be verified that altering the emission site of the W-boson does not mean that the `HEJ` prediction is incorrect, as well as every different combination of various differing flavors of partons involved within the process. `HEJ` is for the most part unconcerned by the flavor of the involved partons; however, there can be phase factors introduced when interchanging a quark and anti-quark line within `HEJ` formalism. These have all been checked thoroughly both upon original calculation, and also at the point of their inclusion within `HEJ2`.

For the unordered process type we consider a process of the type illustrated by Fig. 2.10a. Specifically, we consider the phase-space in Eq. (4.6.1) with a flavor assignment of incoming states defined with p_a as a quark, p_b a quark, with and outgoing flavors: p_1 is a gluon,p_2 is a quark, and p_3 is a quark.

If one attempts to draw the unordered process in a Feynman Diagram-like style, except planar, as in Fig. 2.10a it becomes clear that if strict rapidity ordering is required of the final state particles, there will be a t-channel quark propagator. As per the scaling behaviour which was predicted in Section 2.2.1, we expect that the matrix element will be suppressed by a factor equal to the invariant mass of the unordered gluon and the quark, s_{12} in the phase-space point chosen. As such, we multiply the matrix element itself by a factor of s_{12} to demonstrate that the high energy limit scaling is indeed suppressed by the factor we suspect from Regge theory. This is exactly what we see in Fig. 4.16. The `HEJ` matrix element is not only in

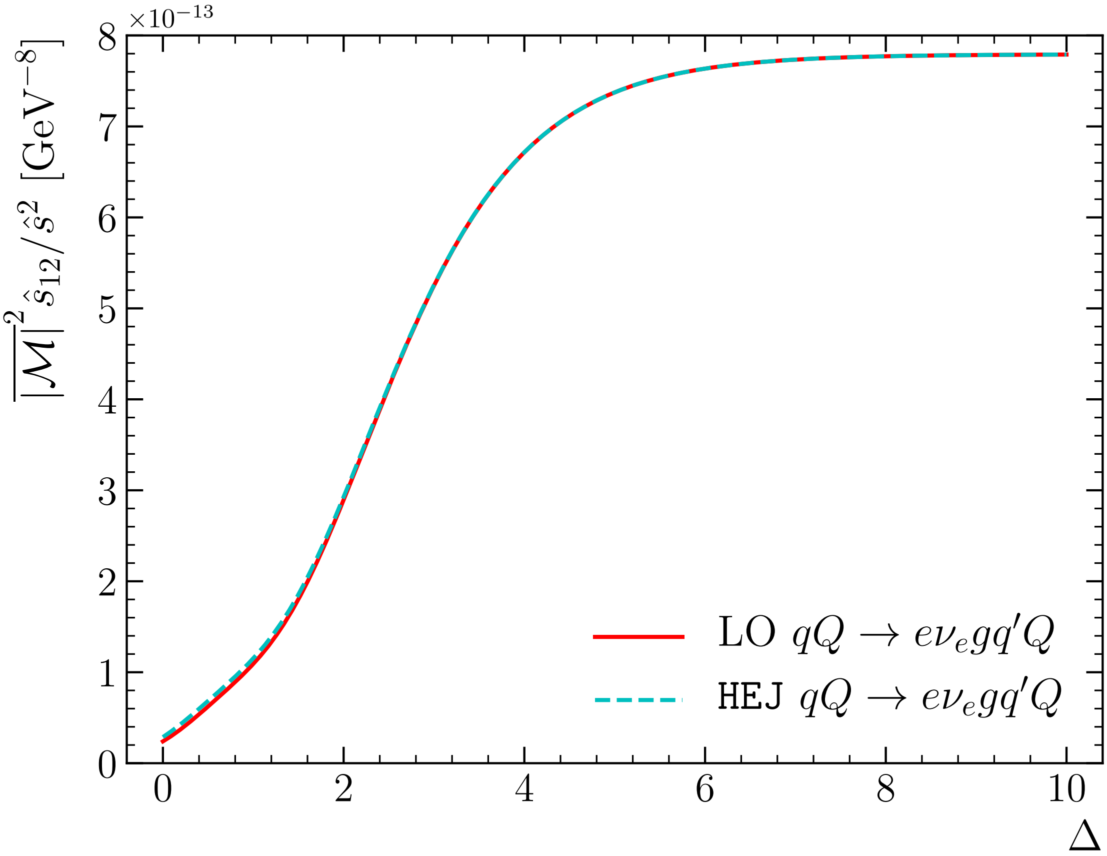

Figure 4.16: *A comparison of* **`HEJ`** *and the leading-order Matrix Elements produced by* **`MadGraph5`** *for an unordered gluon configuration as denoted by the phase-space slice described in Eq.* (4.6.1). *Specifically, the plot demonstrates that the matrix element demonstrates the expected scaling behaviour and also that the* **`HEJ`** *prediction is in good agreement across the whole range of rapidities plotted.*

perfect agreement with the `MadGraph5` matrix element, but it also demonstrates the scaling behaviour we expected.

4.6.2 Explorer Plot of Extremal $q\bar{q}$ Processes

One can complete a similar analysis of the equivalent Extremal $q\bar{q}$ process depicted in Fig. 2.10b, where we again see the necessity of the t-channel quark propagator. For our investigation into the validity of the HEJ matrix element, we consider a phase-space point, again in Eq. (4.6.1) but with the flavor assignment as depicted in the planar diagram such that p_a is a gluon which splits into a quark-anti-quark pair

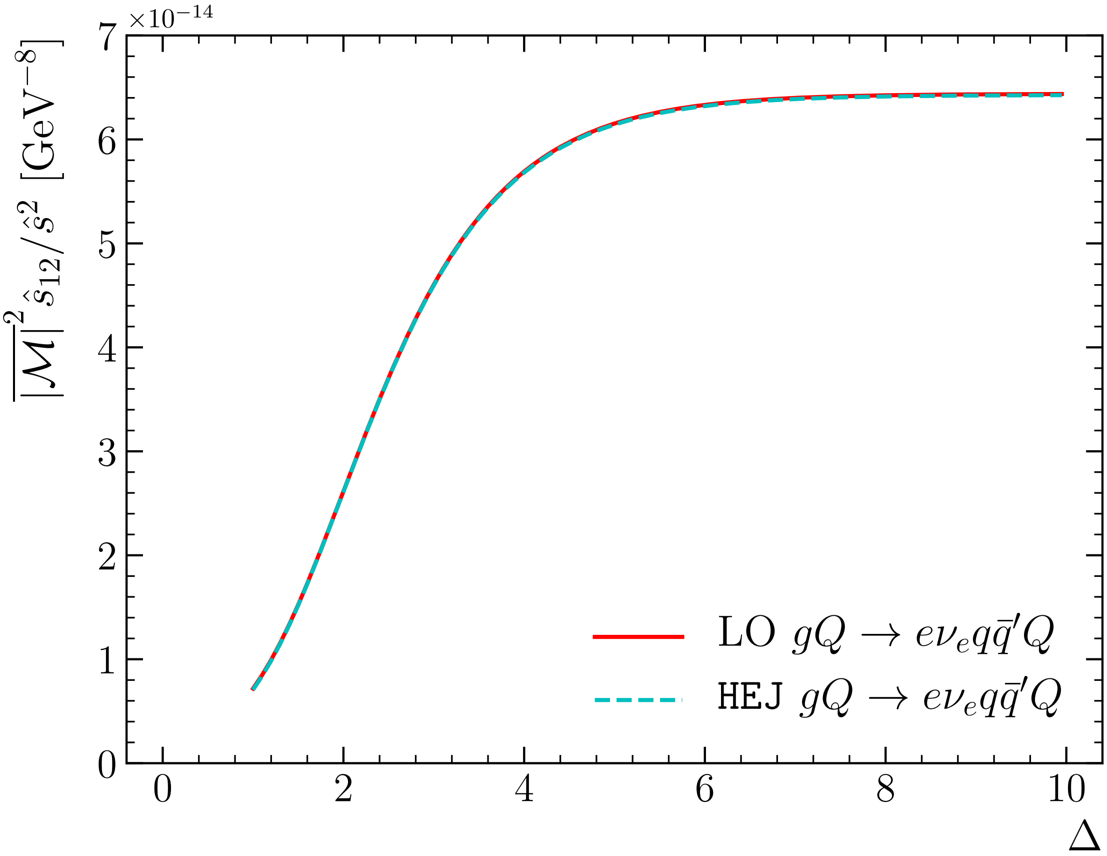

Figure 4.17: *A comparison of* `HEJ` *and the leading-order Matrix Elements produced by* `MadGraph5` *for an extremal* $q\bar{q}$ *configuration as denoted by the phase-space slice described in Eq.* (4.6.1)*. Specifically this plot shows that the matrix element demonstrates the expected scaling behaviour and also that the* `HEJ` *prediction is in good agreement across the whole range of rapidities plotted.*

(p_1 and p_2 in the final state), with the other incoming leg, p_b assigned as a quark and the final particle in the diagram, p_3 also a quark.

We again multiply the matrix elements by a factor s_{12}, which according to Regge theory should be the factor of suppression we expect. Looking at Fig. 4.17, we see that this is indeed the case. The HEJ matrix element is aligned with the leading order prediction for all values of rapidity separation, but also the exact scaling behaviour is exhibited.

It is evident that the matrix elements for both 3-jet NLL real-emission subleading processes, unordered and extremal $q\bar{q}$ exhibit the scaling behaviour that would be expected from them. A further, more stringent check of the formalism was possible at this stage. It has been noted that there is a correspondence between the unordered processes and the extremal $q\bar{q}$ processes. That is by simply applying a *crossing symmetry* to either explicit calculation, it is possible to calculate either process.

4.6.3 Crossing Correspondence

Crossing symmetries work because the only distinction between the incoming and outgoing states in the calculation is whether the spinors are associated with positive or negative frequencies. It is of note that this is how one can distinguish particles and their and anti-particle counterparts. This allows for an incoming particle with momentum p to be treated as an outgoing one with momentum $-p$ and the matrix element which results from Feynman rules applied to the new diagram will be unchanged.

This crossing correspondence is a strong test of both the actual result and also a demonstration of how minimal the approximations made within the `HEJ` calculation are, since this symmetry carries over to the factorised matrix element from the full calculation. We do not delve into the subtleties of this symmetry here, most notably the difficulties associated with defining negative energy spinors. Instead, we simply state that this was explicitly and extensively tested and exploited to ensure that the matrix element which was calculated within `HEJ` is correct.

The following discussion in this section stems from the output of this verification stage of the central $q\bar{q}$ process type which was completed using the program `HEJ_Explorer`. We consider two categories of central $q\bar{q}$ processes, each comprising multiple subprocesses. We will begin with the scenario with the W-boson emitted from an extremal leg, and then follow this up with an investigation into the case of the central $q\bar{q}$ with a W-boson emitted from that effective vertex. In both cases we will check that the scaling of the matrix elements is as expected from Regge theory as described in Section 2.2.1. That is, we expect a suppression of the matrix elements by a factor of $\sqrt{s_{q\bar{q}}}$ due to the necessary quark t-channel propagator in the process.

4.6.4 Central $q\bar{q}$ (Extremal W Emission) Explorer Plots

The matrix element which needs to be verified is the inclusion of the effective central $q\bar{q}$ vertex discussed in the previous section. This means we need to check various different incoming and outgoing parton flavors, and W-boson emission sites to be sure that the process has indeed been included correctly in all of its different manifest forms.

To begin, we first we define our phase-space slice:

$$\begin{aligned}
p_1 =& (p_T \cosh(\Delta), p_T \cos(\phi_1), p_T \sin(\phi_1), p_T \sinh(\Delta)) && (4.6.2)\\
p_2 =& (p_T \cosh(y_2), p_T \cos(\phi_2), p_T \sin(\phi_2), p_T \sinh(y_2)) && (4.6.3)\\
p_{\bar{l}} =& p_e = (p_{eT} \cosh(y_e), p_{eT} \cos(\phi_e), p_{eT} \sin(\phi_e), p_{eT} \sinh(y_e)) && (4.6.4)\\
p_l =& p_{\nu_e} = (p_{\nu T} \cosh(y_\nu), p_{\nu T} \cos(\phi_\nu), p_{\nu T} \sin(\phi_\nu), p_{\nu T} \sinh(y_\nu)) && (4.6.5)\\
p_3 =& (p_T \cosh(y_3), p_T \cos(\phi_3), p_T \sin(\phi_3), p_T \sinh(y_3)) && (4.6.6)\\
p_4 =& (|\vec{p}_{4T}| \cosh(-\Delta), |\vec{p}_{4T}| \cos(\phi_4), |\vec{p}_{4T}| \sin(\phi_4), |\vec{p}_{4T}| \sinh(-\Delta)) && (4.6.7)\\
p_a =& (\tfrac{x_a\sqrt{\hat{s}}}{2}, 0, 0, \tfrac{x_a\sqrt{\hat{s}}}{2}) && (4.6.8)\\
p_b =& (\tfrac{x_b\sqrt{\hat{s}}}{2}, 0, 0, \tfrac{-x_b\sqrt{\hat{s}}}{2})\,, && (4.6.9)
\end{aligned}$$

where the rapidities $y_2 = -y_3 = \frac{\Delta}{3}$, $p_T = p_{eT} = 40GeV$, $p_{\nu T} = \frac{m_W^2}{2p_{eT}(\cosh(y_e-y_\nu)-\cos(\phi_e-\phi_\nu))}$, $y_e = y_\nu = \Delta$, $\phi_1 = \frac{2\pi}{3}$, $\phi_e = \frac{\pi}{2}$, $\phi_\nu = -\frac{\pi}{2}$ are parameters chosen to ensure our partons when exploring phase-space do not go too soft. And where our final momentum, $\vec{p}_{4T} = (|\vec{p}_{4T}| \cos(\phi_4), \vec{p}_{4T} \sin(\phi_4))$ is set through transverse momentum conservation. Longitudinal momentum conservation is set thanks to:

$$x_a = \sum_i \tfrac{p_{iT}}{\sqrt{\hat{s}}} e^{y_i}\,,$$

$$x_b = \sum_i \tfrac{p_{iT}}{\sqrt{\hat{s}}} e^{-y_i}\,,$$

where the index i refers to the outgoing particles. Within this parameterisation we consider the momentum assignment:

$$Q(p_a)Q'(p_b) \to e(p_e)\nu(p_\nu)Q(p_1)q(p_2)\bar{q}(p_3)Q'(p_4)\,, \tag{4.6.10}$$

where Q and Q' are allowed to be any partonic flavors with the only constraint that at most one of them is a gluon, since what we are testing here is the Matrix Element for one of these partons emitting a W-boson and then a $q\bar{q}$ pair produced between them in a wide rapidity span. In all of our phase-space explorer validations our investigation will be checking that the matrix element produced by `HEJ` agrees with `MadGraph5` for variations in the parameter Δ. In this particular case, this leads to the matrix element approaching the strict MRK limit.

We further test this, by checking that the Matrix Element exhibits the scaling behaviour we expect from Regge Theory: that it will be suppressed by a factor $\frac{1}{\sqrt{s_{q\bar{q}}}}$.

We show the results of these exploratory plots for a W^+-boson emission from an extremal leg in Fig. 4.18 and Fig. 4.19, and for W^--boson emission in Fig. 4.20 and Fig. 4.21. In all plots, we show the squared matrix element produced by HEJ plotted against the squared Matrix element generated by the fixed-order Generator `MadGraph`. In the plots on the left we see the squared Matrix element itself, and the plots on the right show the squared matrix element multiplied by $\hat{s}_{q\bar{q}}$.

At large rapidity separations, the `HEJ` matrix element aligns with the Matrix element produced by `MadGraph`. This is demonstrated clearly by the ratio in the bottom pane of each plot Further, the plots on the right show that the Matrix element scales as we expect from Regge Theory, with a suppression by the factor $\frac{1}{\sqrt{s_{q\bar{q}}}}$.

We again that there is a larger discrepancy between the MG and `HEJ` result for lower rapidity spans in the events that include incoming gluons, which are displayed in Fig. 4.25 and Fig. 4.23. We don't expect a great agreement for low rapidity spans in general, but the decreased predictive power of `HEJ` here is due to the larger number of channels that are available between the incoming and outgoing states that are not

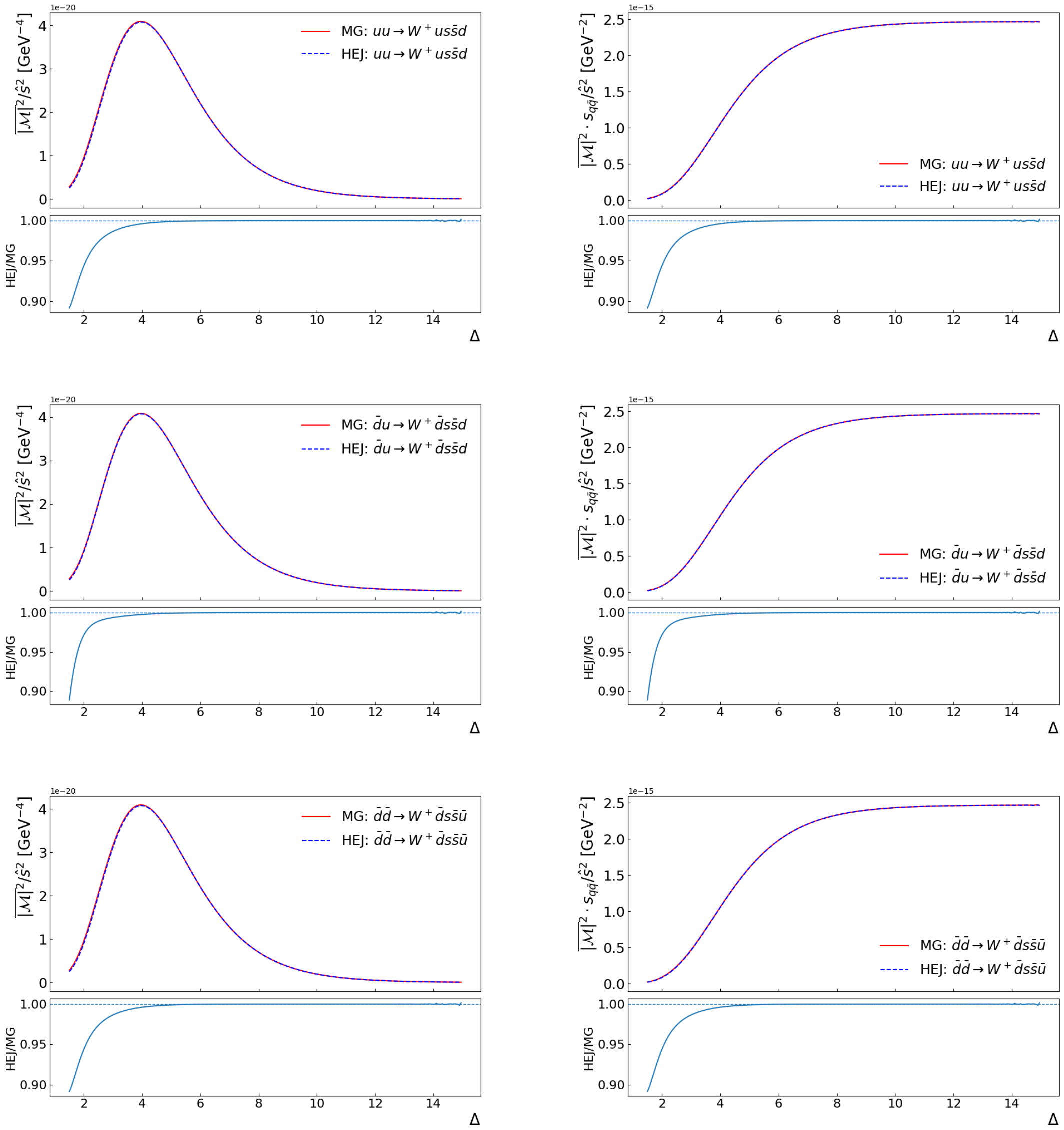

Figure 4.18: *Explorer plots for the Central $q\bar{q}$ process with the emission of a W^+-boson from an Extremal leg. Included in this figure are event types with incoming quarks and/or anti-quarks. On the left we have the* ***`HEJ`*** *and* ***`MadGraph`*** *squared Matrix elements plotted against increasing rapidity. On the right, we have the same plot by with the squared Matrix elements multiplied by the factor $\hat{s}_{q\bar{q}}$, demonstrating the expected scaling behaviour. In each plot, the bottom pane shows the ratio of the two predictions, which trends to unity for large rapidity spans.*

covered by the MRK limit in the case of incoming gluons. This in turn makes our prediction away from this limit worse, and is where our reweighting of this matrix element is important.

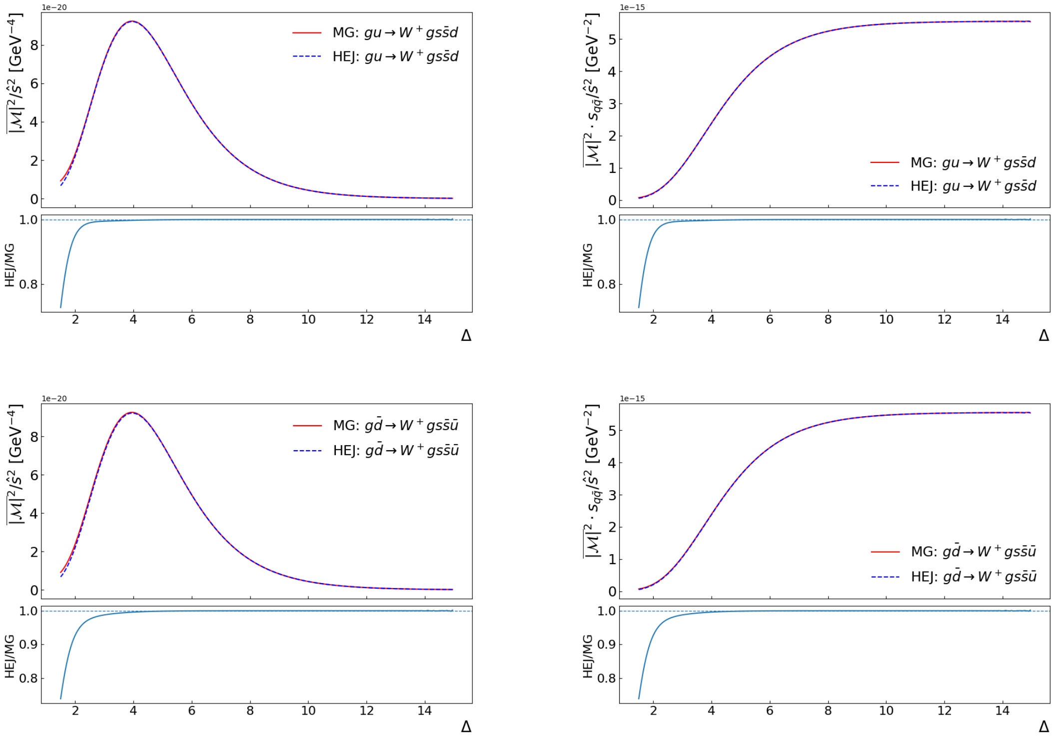

Figure 4.19: *Explorer plots for the Central $q\bar{q}$ process with the emission of a W^+-boson from an Extremal leg. Included in this figure are event types which include incoming gluons. On the left we have the* ***HEJ*** *and* ***MadGraph*** *squared Matrix elements plotted against increasing rapidity. On the right, we have the same plot by with the squared Matrix elements multiplied by the factor $\hat{s}_{q\bar{q}}$, demonstrating the expected scaling behaviour. In each plot, the bottom pane shows the ratio of the two predictions, which trends to unity for large rapidity spans.*

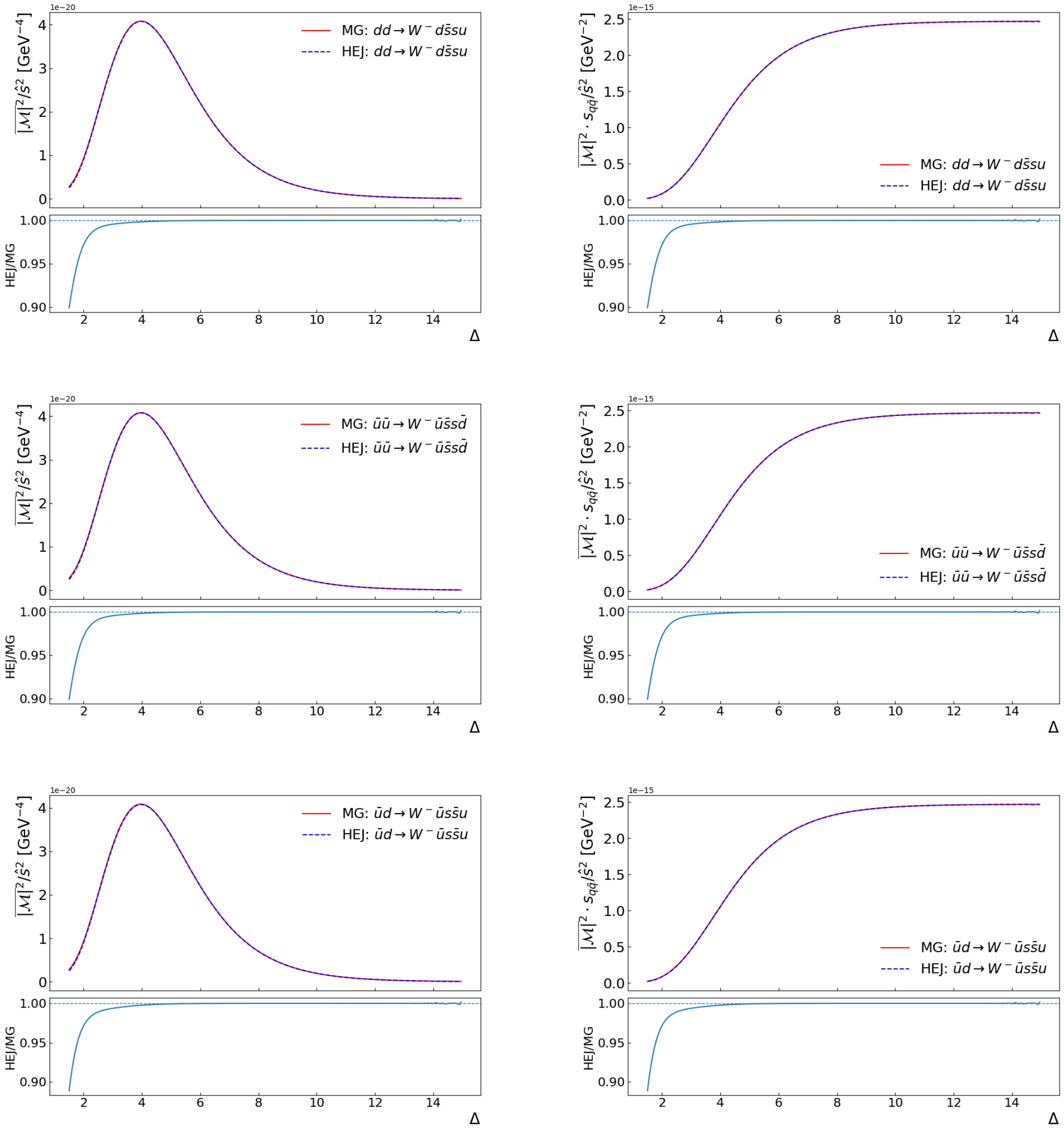

Figure 4.20: *Explorer plots for the Central $q\bar{q}$ process with the emission of a W^--boson from an Extremal leg. Included in this figure are event types with incoming quarks and/or anti-quarks. On the left we have the* ***`HEJ`*** *and* ***`MadGraph`*** *squared Matrix elements plotted against increasing rapidity. On the right, we have the same plot by with the squared Matrix elements multiplied by the factor $\hat{s}_{q\bar{q}}$, demonstrating the expected scaling behaviour. In each plot, the bottom pane shows the ratio of the two predictions, which trends to unity for large rapidity spans.*

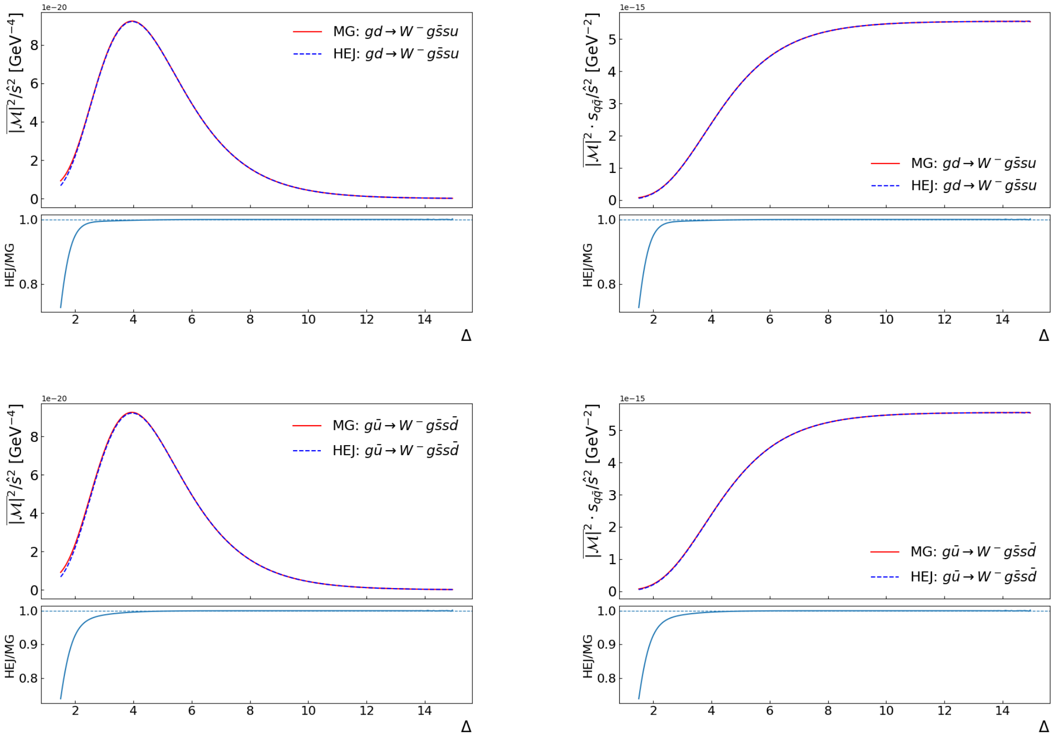

Figure 4.21: *Explorer plots for the Central $q\bar{q}$ process with the emission of a W^--boson from an Extremal leg. Included in this figure are event types which include incoming gluons. On the left we have the **`HEJ`** and **`MadGraph`** squared Matrix elements plotted against increasing rapidity. On the right, we have the same plot by with the squared Matrix elements multiplied by the factor $\hat{s}_{q\bar{q}}$, demonstrating the expected scaling behaviour. In each plot, the bottom pane shows the ratio of the two predictions, which trends to unity for large rapidity spans.*

4.6.5 Central $q\bar{q}$ (Central W Emission) Explorer Plots

In this section we will be looking at a very similar process, in which the W-boson is instead emitted from the central $q\bar{q}'$ pair itself, meaning we will relax the conditions in the previous section that one of the initial partons must be not be a gluon.

We will be using the same phase-space slice detailed in Eq. (4.6.2), where the only difference for these plots will be that $y_l = y_{\bar{l}} = \frac{\Delta}{3}$ as this will place these particles close in rapidity to the jet which emitted.

The processes selected for display are chosen to minimise ambiguity as to which partons emitted the W-bosons. By this, we mean that the outgoing extremal partons match the incoming partons in all processes, and also that the $q\bar{q}'$ pair that are produced in the particular process are of a different flavor than any of the other partons in the process.

We see the results of these exploratory plots for W^+-boson emission in Fig. 4.22 and Fig. 4.23, and the exploratory plots for W^--boson emission from this central $q\bar{q}'$ pair in Fig. 4.24 and Fig. 4.25. As before, in all plots we have the HEJ output and the MG output compared. Once again, we observe excellent agreement between the `HEJ` matrix element and the fixed-order prediction produced by `MadGraph` at large rapidity spans as demonstrated by the ratio plots that are the bottom pane of each plot.

The plots on the right of the figure are, similar to those produced in the previous section, designed to check that the matrix element scales as would be suggested by Regge Theory. We indeed see this, as the plots show in this separate process that there is again a suppression of the Matrix element by the factor $\frac{1}{\sqrt{s_{q\bar{q}}}}$.

We note again that there is a larger discrepancy between the MG and `HEJ` result for lower rapidity spans in the events that include incoming gluons, which are displayed in Fig. 4.25 and Fig. 4.23. As mentioned in the previous section, we don't expect a great agreement for low rapidity spans in general, but the decreased predictive power of `HEJ` here is due to the larger number of channels that are available between

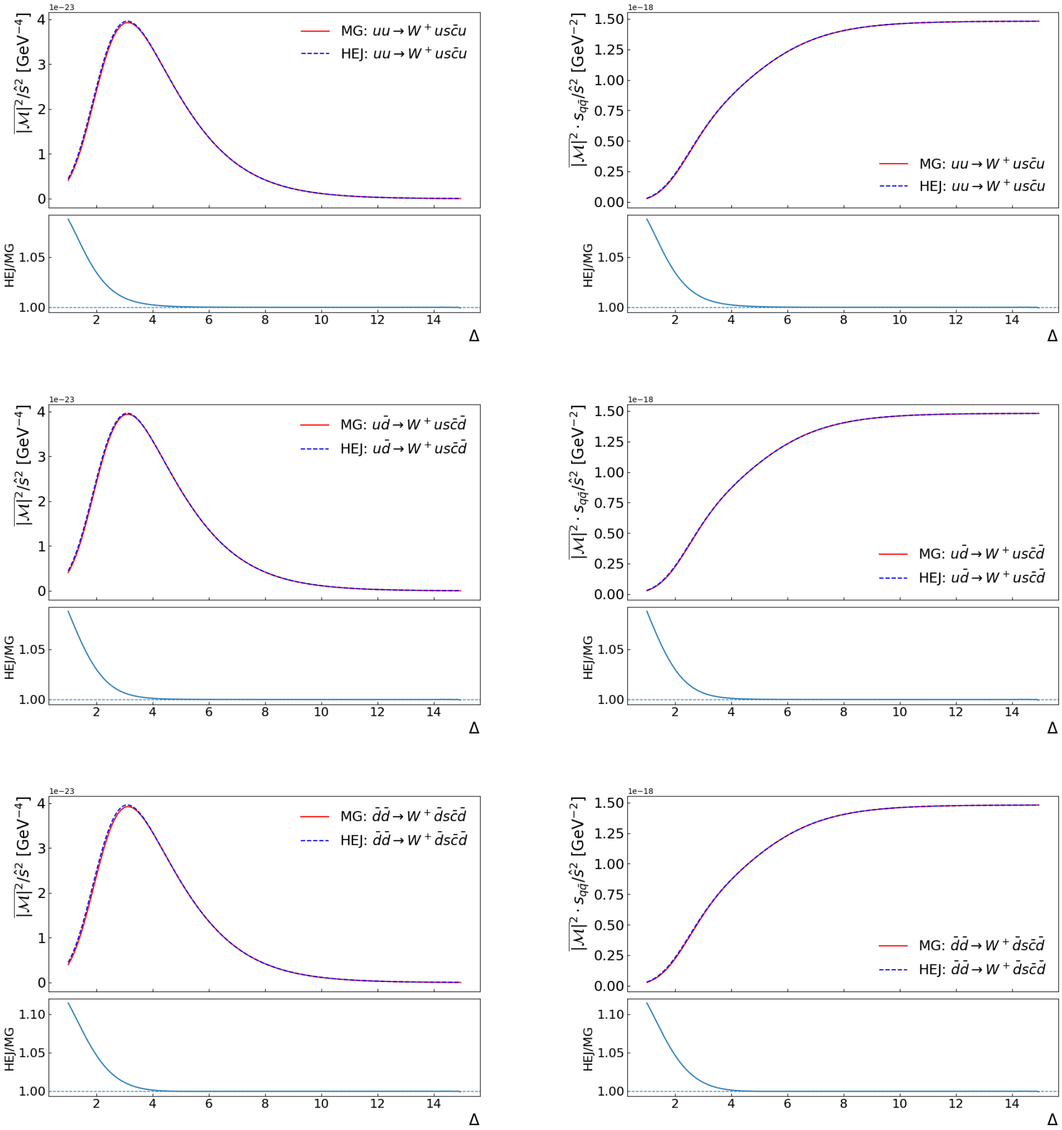

Figure 4.22: *Explorer plots for the Central $q\bar{q}$ process with the emission of a W^+-boson from the Central $q\bar{q}$ effective vertex. Included in this figure are processes with incoming quarks and/or anti-quarks. On the left we have the **`HEJ`** and **`MadGraph`** squared Matrix elements plotted against increasing rapidity. On the right, we have the same plot by with the squared Matrix elements multiplied by the factor $\hat{s}_{q\bar{q}}$, demonstrating the expected scaling behaviour. In each plot, the bottom pane shows the ratio of the two predictions, which trends to unity for large rapidity spans.*

the incoming and outgoing states that are not covered by the MRK limit in the case of incoming gluons. This in turn makes our prediction away from this limit worse, and is where our reweighting of this matrix element is important.

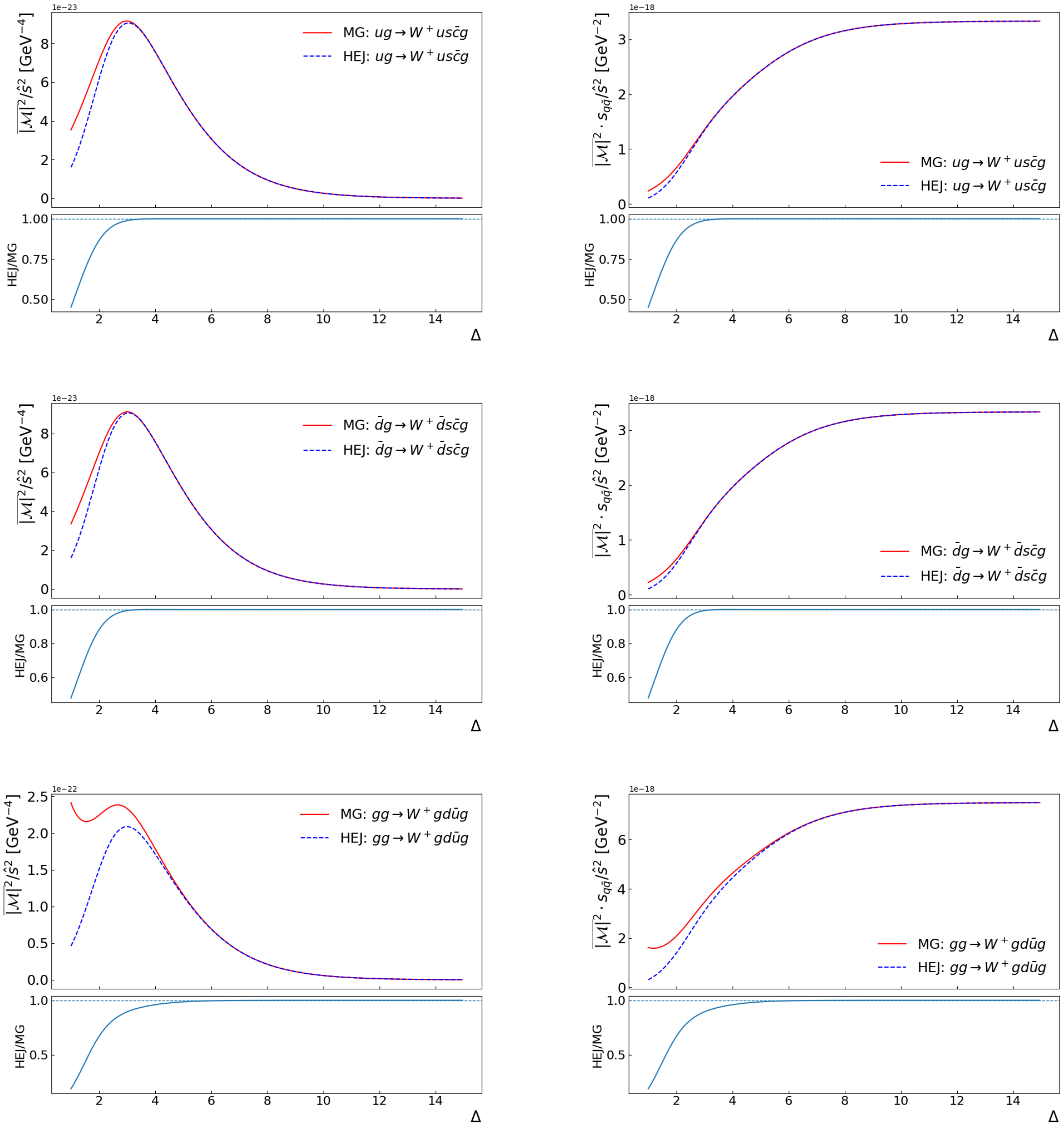

Figure 4.23: *Explorer plots for the Central $q\bar{q}$ process with the emission of a W^+-boson from the Central $q\bar{q}$ effective vertex. Included in this figure are processes with incoming gluons. On the left we have the* `HEJ` *and* `MadGraph` *squared Matrix elements plotted against increasing rapidity. On the right, we have the same plot by with the squared Matrix elements multiplied by the factor $\hat{s}_{q\bar{q}}$, demonstrating the expected scaling behaviour. In each plot, the bottom pane shows the ratio of the two predictions, which trends to unity for large rapidity spans.*

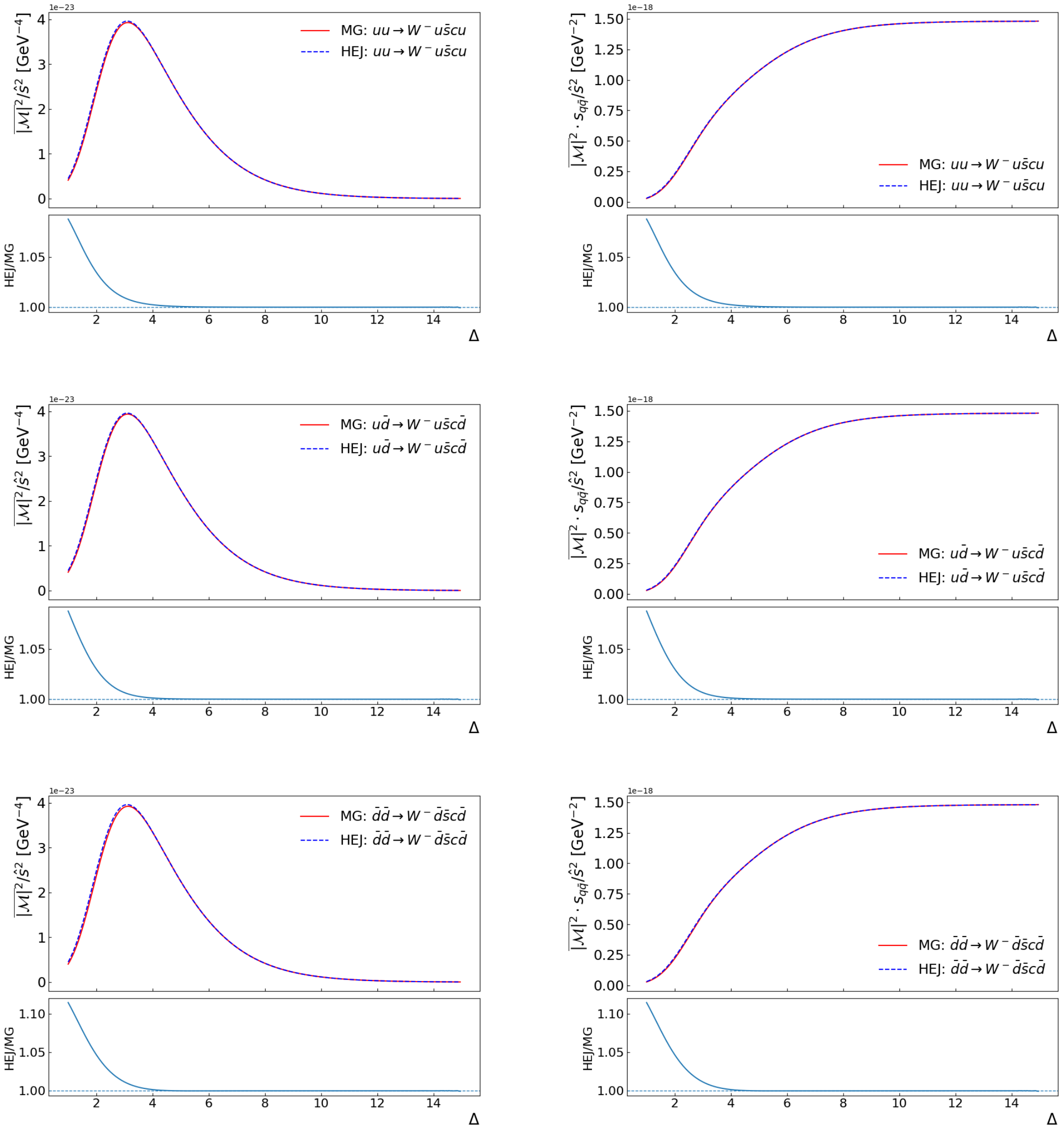

Figure 4.24: *Explorer plots for the Central $q\bar{q}$ process with the emission of a W^--boson from the Central $q\bar{q}$ effective vertex. Included in this figure are processes with incoming quarks and/or anti-quarks. On the left we have the* ***HEJ*** *and* ***MadGraph*** *squared Matrix elements plotted against increasing rapidity. On the right, we have the same plot by with the squared Matrix elements multiplied by the factor $\hat{s}_{q\bar{q}}$, demonstrating the expected scaling behaviour. In each plot, the bottom pane shows the ratio of the two predictions, which trends to unity for large rapidity spans.*

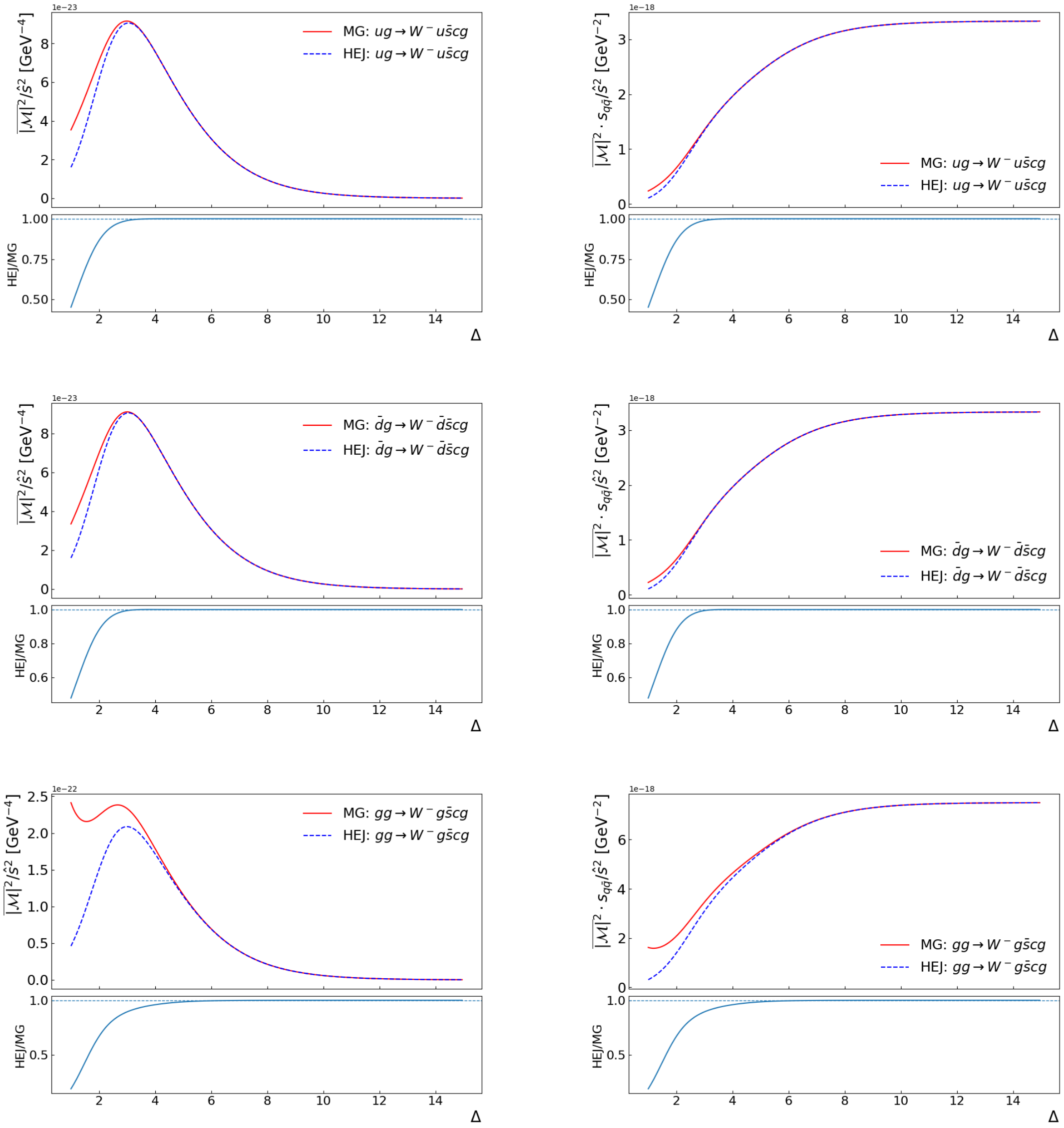

Figure 4.25: *Explorer plots for the Central $q\bar{q}$ process with the emission of a W^--boson from the Central $q\bar{q}$ effective vertex. Included in this figure are processes with incoming gluons. On the left we have the* ***HEJ*** *and* ***MadGraph*** *squared Matrix elements plotted against increasing rapidity. On the right, we have the same plot by with the squared Matrix elements multiplied by the factor $\hat{s}_{q\bar{q}}$, demonstrating the expected scaling behaviour. In each plot, the bottom pane shows the ratio of the two predictions, which trends to unity for large rapidity spans.*

4.6.6 Further verifications

Comparing matrix elements to fixed-order results was only one aspect of our verification strategy that we carried out to check the results of the calculation made within `HEJ`. Other, non-trivial checks that were made include ensuring that varying helicity combinations gave the same result for all diagrams in the MRK limit.

Further, we checked that HEJ produced the same output for a flip of the z-axis in the process. We further verified invariance under rotation about the z-axis for all momenta involved. As mentioned in a previous section, we also checked the crossing correspondence by checking the results of inverted momenta in these processes inputted into `HEJ`.

After all the verifications described, we are confident that the matrix element itself is correct, and can move onto the results which we obtained through the inclusion of these subleading corrections in the W+jets process within `HEJ`.

CHAPTER

FIVE

RESULTS

We now present the results arising from the implementation of these NLL contributions

5.1 Numerical Impact of NLL Components

All the predictions made with `HEJ` before 2020 [7, 66, 78–81] – that is – before the publishing of [9], were made with matching to leading-order fixed-order calculations. At the same time as the NLL updates were being made to improve the logarithmic accuracy of HEJ, it was also being updated to match to NLO fixed-order calculations.

The details of this are introduced in [9], and we do not discuss these in detail here, but it is necessary to mention this, as it formulates one aspect of the results that are to be presented in this Chapter. In Figures 4.1 and 4.2 in section 4.1, we presented a breakdown of the leading-order cross-section for $pp \to W+3j$ and $pp \to W+4j$. The individual contributions were separated into leading-log (LL) configurations, next-to-leading-log (NLL) configurations and other (i.e. further suppressed) configurations and in those figures we showed that NLL contributions account for up to 40% of the cross-section in key regions of phase-space. In Chapter 4 have introduced all the necessary components to construct `HEJ` amplitudes for these NLL configurations, so we can now perform an all-order resummation of the dominant high-energy effects across this extended region of phase-space. We will now illustrate the numerical impact of these new components.

In Figures 5.1–5.6, we illustrate the impact in various distributions by plotting the all-order and fixed-order components and analyse the contributions using separate subplots.

1. First, in each of these Figures, the plot at the top left shows the LO result plus all HEJ LL corrections. Resummation in this first subplot occurs in the processes listed in the middle column of Table 4.1. These processes form the 'all-order component' and are displayed by the red dashed line. All other subprocesses are displayed in the subplot as fixed-order only as the blue dashed line.
2. Second, in each of these Figures, the plot at the top right shows the LO result plus all HEJ NLL corrections. Resummation in this second subplot occurs in the processes listed in the middle and right columns of Table 4.1. These processes form the 'all-order component' and are displayed by the red dashed line. All other subprocesses are displayed in the subplot as fixed-order only as the blue dashed line.
3. Finally, there is a third subplot beneath the other two which shows the relative difference between the top left, and top right plots divided by the results of the top left plot.

Fig. 5.1 shows the inclusive jet rates for $pp \to (W \to l\nu)\pm \geq N_{jets}$. When resummation is only applied to LL states the all-order component decreases with each multiplicity. This makes sense when we consider the increase of the number of possible states with each extra jet. The NLL components presented in this thesis are introduced only for events containing three or more jets, so the relative change

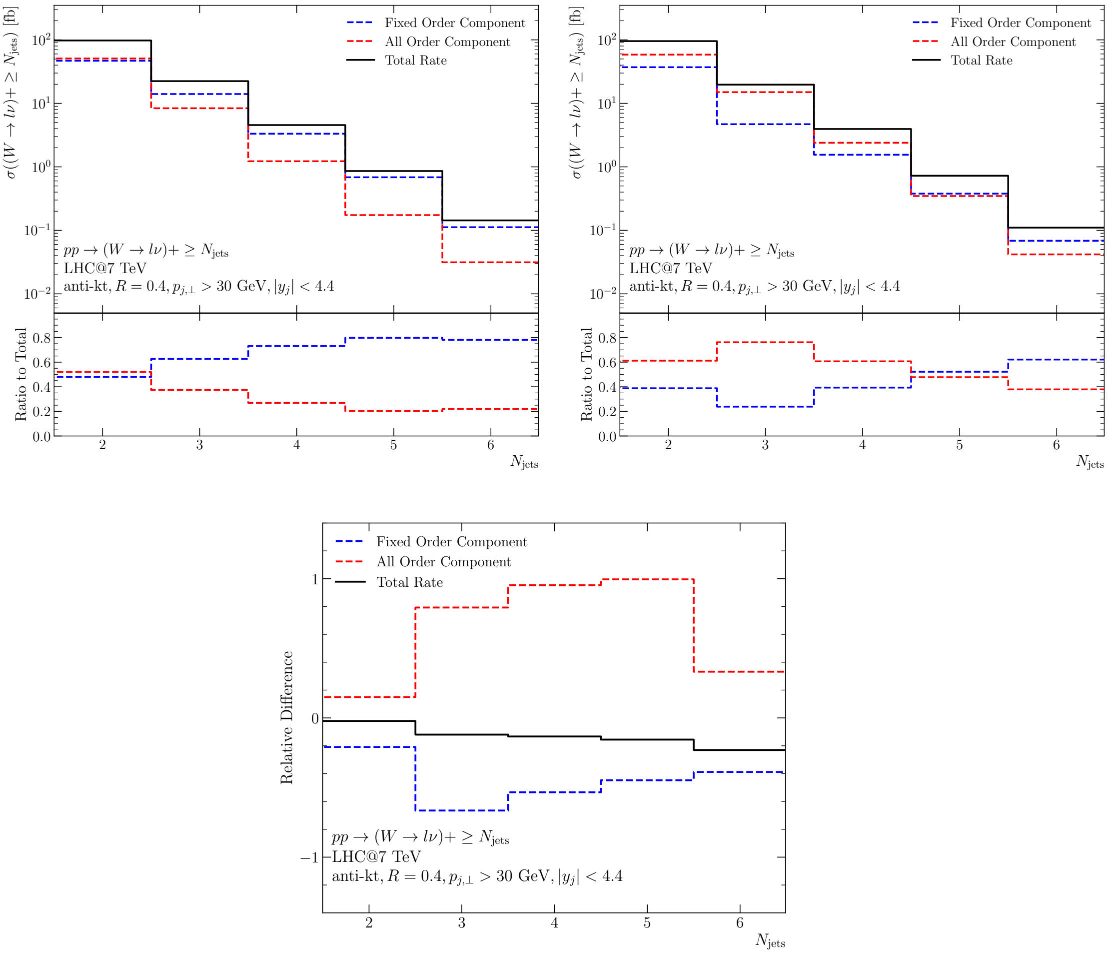

Figure 5.1: *Inclusive Njets cross-sections for* $pp \to (W \to l\nu)+ \geq N_{jets}$ *where , in the top left resummation is applied only to LL states. In the top-right resummation is applied to all LL and NLL states. Also shown in each case is the breakdown into the component where all-order resummation is applied (red, dashed) and the component which remains described at fixed- order only (blue, dashed). The final subplot, which shows the relative difference between these two scenarios.*

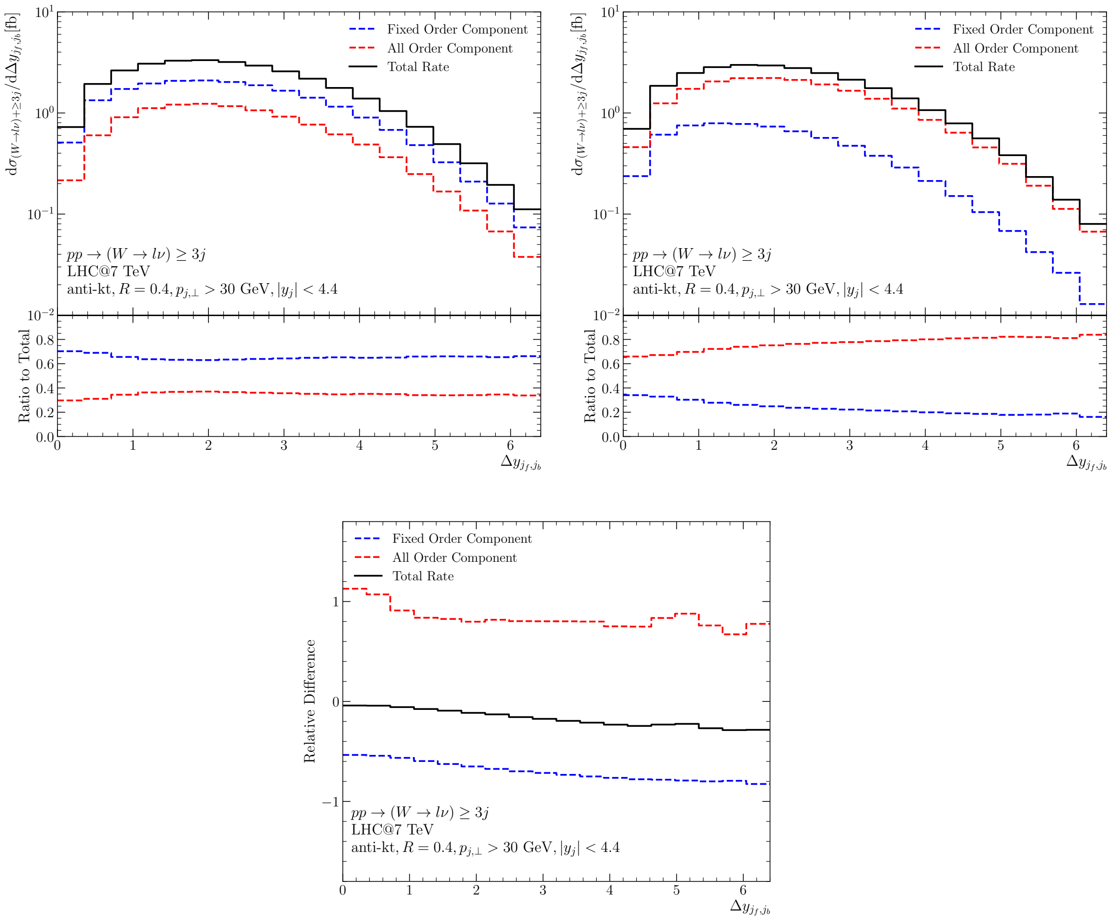

Figure 5.2: *The differential distribution (black, solid) in the rapidity difference between the most-forward and most-backward jets,* $\Delta y_{j_f,j_b}$*, in* $pp \to (W \to l\nu)+ \geq 3j$*, without and with resummation applied to NLL states. The panels and lines are as in Fig. 5.1*

in the 2 jet bin is small. In the bins representing a higher number of jets we see a significant increase in the fraction of the cross-section described by the all-order contributions.

This clearly illustrates that although the new NLL contributions are formally suppressed, they are numerically highly significant in realistic LHC analyses.

In Fig. 5.2 we show the rapidity difference between the most-forward and most-backward jets $\Delta_{y_{j_f,j_b}}$, for $pp \to (W \to l\nu)\pm \geq 3j$. We see that the all-order component (red dashed) illustrated in the first subplot is between $30 - 40\%$ across the entire range, with the remainder being the fixed-order component. The addition of the NLL components being resummed introduces a dramatic increase in the amount of the distribution described by the all-order components, ranging between

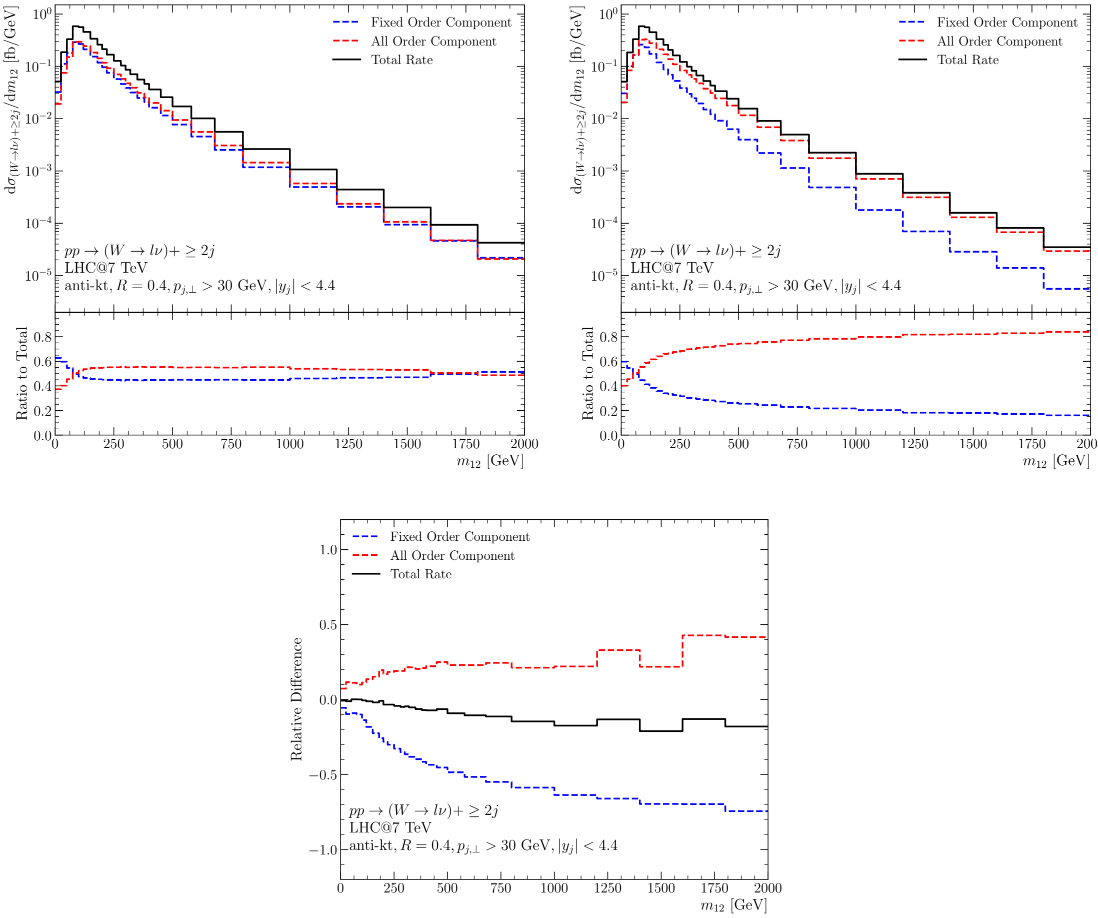

Figure 5.3: *The differential distribution (black, solid) in the invariant mass of the two leading jets in $pp \to (W \to l\nu) \geq 2j$, without and with resummation applied to NLL states. The panels and lines are as in Fig. 5.1*

65% at $\Delta_{y_{j_f,j_b}} = 0$ to 80% at $\Delta_{y_{j_f,j_b}} = 6.5$.

The final subplot, depicting the relative difference between these two cases shows that the total cross-section decreases linearly across the distribution to around -25% at large $\Delta_{y_{j_f,j_b}}$. The changes in the relative components are much larger. The relative stability of the total cross-section despite the inclusion of additional all-order components, indicates the perturbative stability of the `HEJ` framework [9].

In Fig. 5.3, we show the comparison between the LL and NLL predictions and the breakdown of the different components in the distribution of the invariant mass of the two leading jets in $pp \to (W \to l\nu) \geq 2j$. We see when all-order corrections are just applied to the LL contributions the all-order components begin at 37% rising to 55% at $m_{12} = 125$GeV, and remains stable up to $m_{12} = 2$ TeV. When we perform

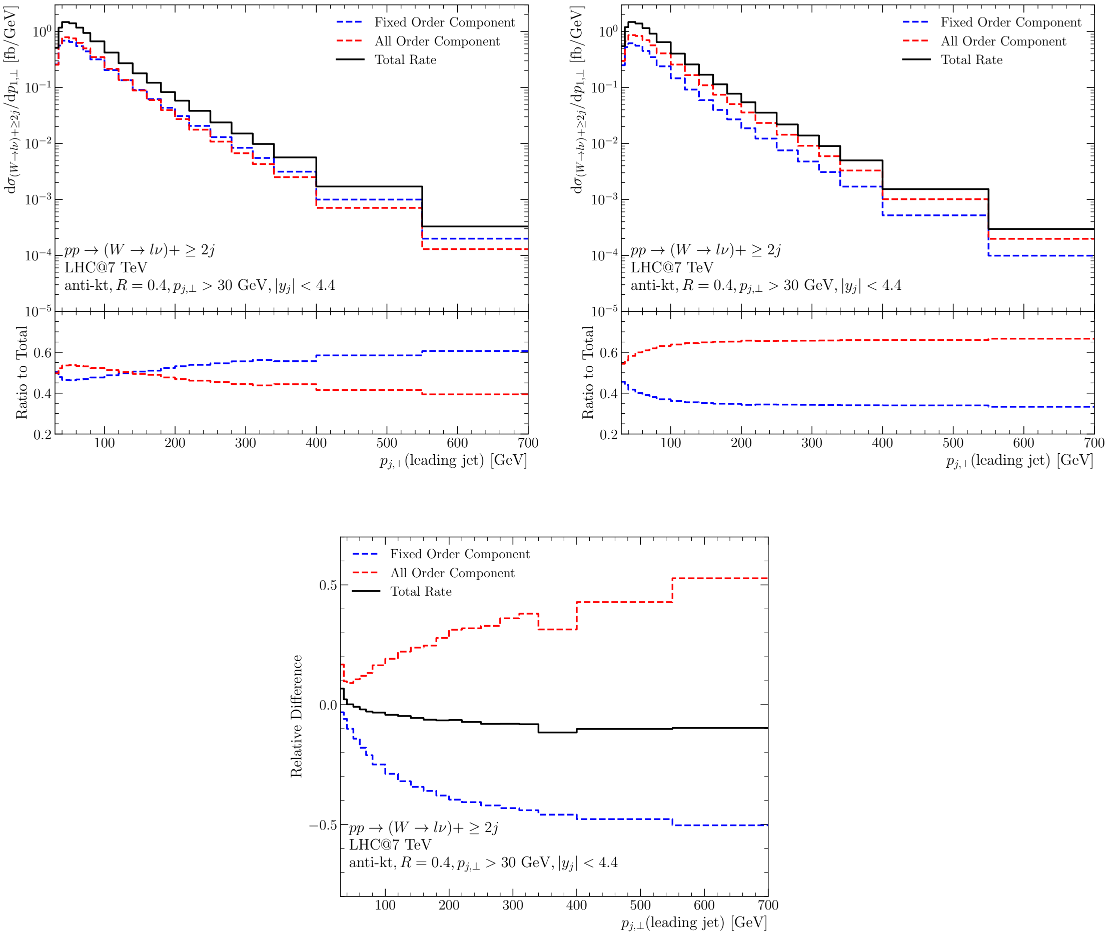

Figure 5.4: *The differential distribution (black, solid) in the transverse momentum of the leading jet in $pp \to (W \to l\nu) \geq 2j$, without and with resummation applied to NLL states. The panels and lines are as in Fig. 5.1*

resummation on the NLL processes we see this all-order component increase to 80% of the total cross-section at large m_{12}. This behaviour is expected, as larger values of m_{12} correspond more closely to the MRK limit, which requires a large invariant mass between all jets.

In Fig. 5.4 we show the transverse momentum distribution of the leading jet in $pp \to (W \to l\nu) \geq 2j$ events. As we saw in Fig. 5.1, the inclusive cross-section of the 2-jet events can see that the all-order component is larger than the fixed-order component for low $p_{j,\perp}$, even for the LL resummation only plot. This steadily falls to 40% for increasing $p_{j,\perp}$. After all-order corrections are applied to the NLL states the behaviour of the distribution changes and the all-order component instead rises as a

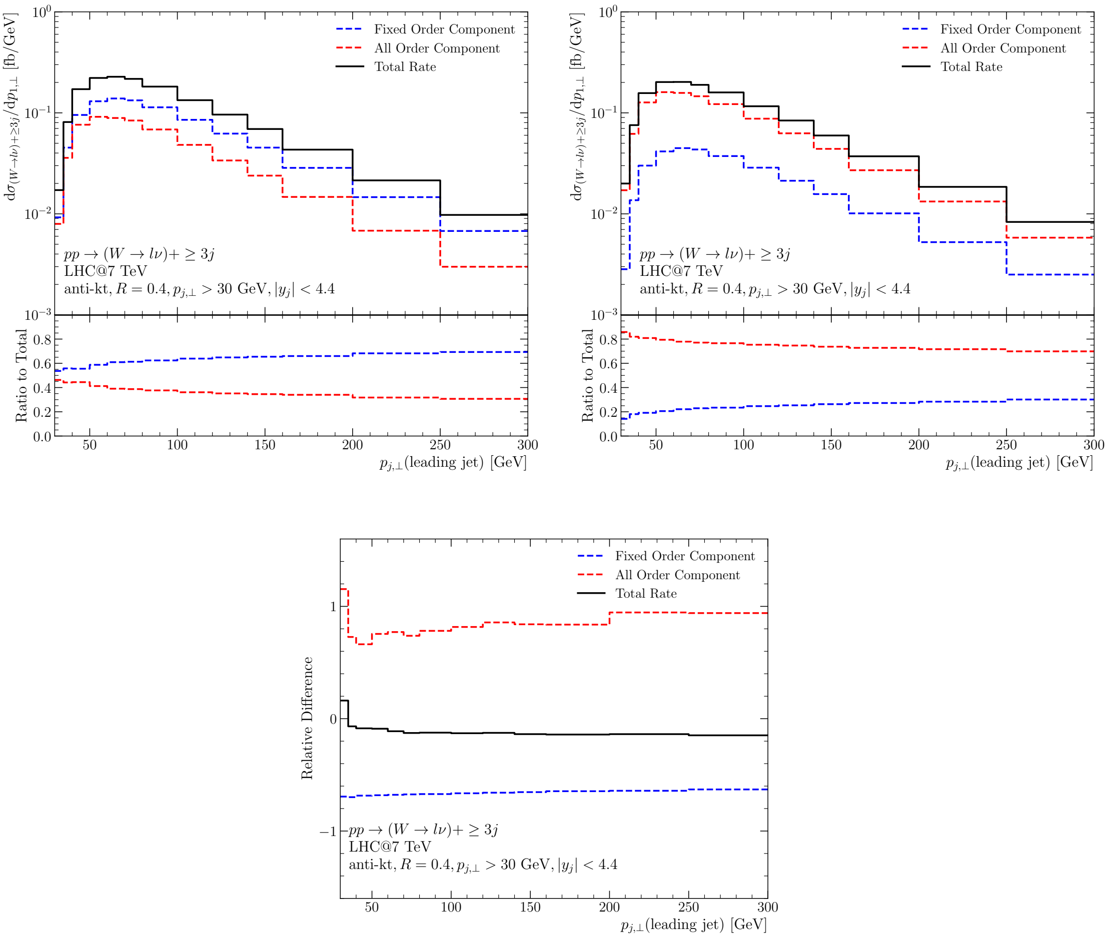

Figure 5.5: *The differential distribution (black, solid) in the transverse momentum of the leading jet in $pp \to (W \to l\nu)+ \geq 3j$, without and with resummation applied to NLL states. The panels and lines are as in Fig. 5.1*

fraction of the total, up to 67% at $p_{j,\perp} = 700$GeV. We see in the relative difference plot that the as $p_{j,\perp}$ increases, the size of the all-order component increases by 50% and the fixed-order component decreases by 50%.

Fig. 5.5 depicts the same analysis for the transverse momentum distribution of the leading jet in $pp \to (W \to l\nu)\pm \geq 3j$. Since the NLL components only come into play for $\geq 3j$, we expect a more dramatic change in the distribution than that depicted in Fig. 5.4. We again see a dramatic increase in the component of the cross-section controlled by the all-order resummation, from 40% for just LL component resummation to near 80% when the NLL components are included for low transverse momenta. The relative change in the total cross-section is again small at 8%, but the

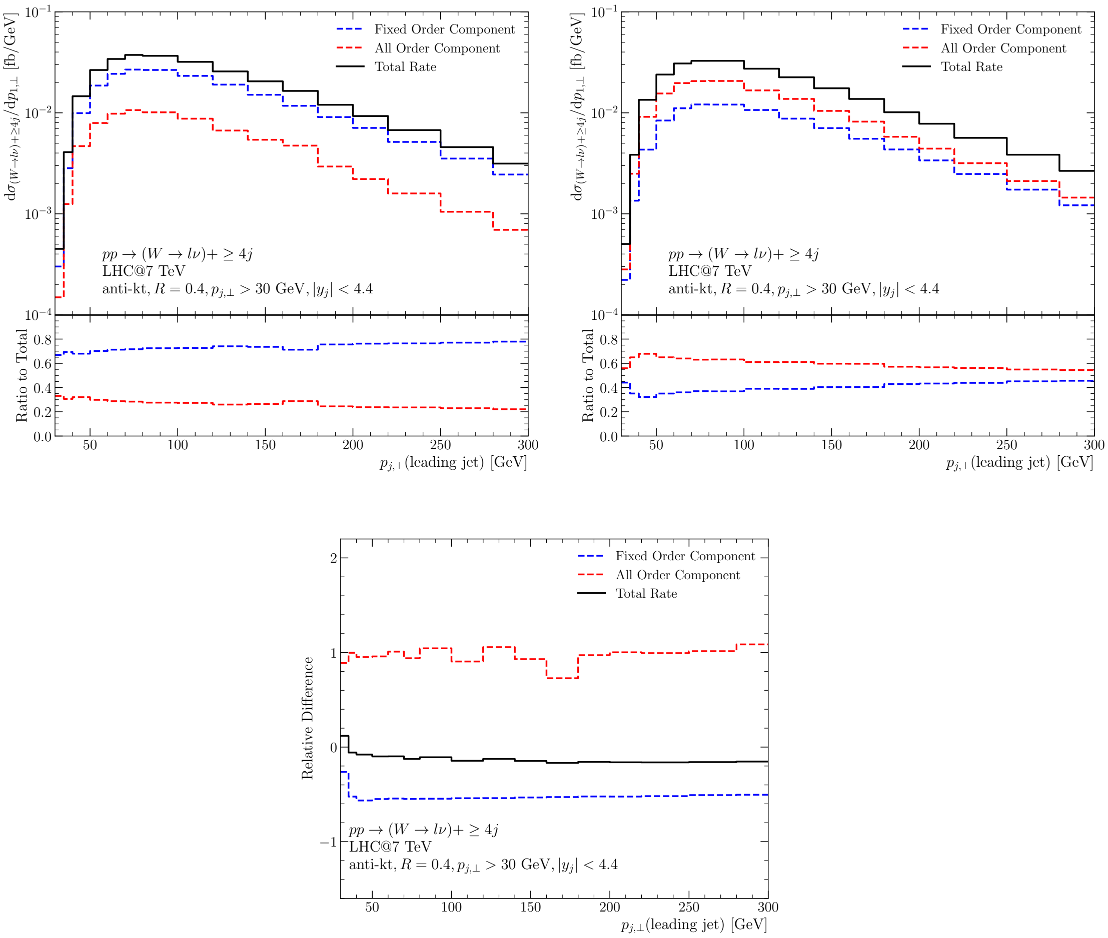

Figure 5.6: *The differential distribution (black, solid) in the transverse momentum of the leading jet in $pp \to (W \to l\nu)+ \geq 4j$, without and with resummation applied to NLL states. The panels and lines are as in Fig. 5.1*

fixed-order component is reduced by around 30% whereas the all-order component increases by around 100%.

In Fig. 5.6 we show the same analysis again for the transverse momentum distribution of the leading jet, but this time for $pp \to (W \to l\nu) \pm \geq 4j$. Since all the corrections derived in Chapter 4 require at least four hard jets, we expect again a large improvement, as we include more processes. Despite the inclusion of more processes into the all-order component, it makes up a smaller fraction of the total cross-section than in Fig. 5.5 since there are significantly more processes that contribute to a $4j$ process. We observe an increase from $20\% - 30\%$ to $55\% - 65\%$ between the top left and top right plots. We see the relative differences are very

Lepton p_T	p_T> 25 GeV
Lepton rapidity	$\|\eta\| < 2.5$
Missing transverse momentum	$E_\mathrm{T}^\mathrm{miss} > 25$ GeV
Reconstructed transverse mass of boson	$m_\mathrm{T} > 40$ GeV
Jet p_T	$p_\mathrm{T} > 30$ GeV
Jet rapidity	$\|y\| < 4.4$
Jet isolation	$\Delta R(l, \mathrm{jet}) > 0.5$ (7 TeV [8]), 0.4 (8 TeV [10]) jet is removed

Table 5.1: *Selection cuts for the data analyses*

similar to the three-jet case.

5.2 ATLAS Predictions

The predictions of `HEJ` including these subleading corrections have been included in multiple ATLAS studies. This section compares predictions made with [82] to analyses by ATLAS of Wjj at LHC energies of 7 TeV [8] and 8 TeV [10], and we will in particular focus on distributions where the new components lead to important improvements. The data was collected using slightly different cuts for the electron and muon channel, and then extrapolated to a 'combined' selection contrasted with predictions generated with the following cuts listed in Table 5.1. The rapidity selection criteria for jets, accepting jets of rapidities in the full detector, not just the central part, is particularly important for the study of high-energy logarithms: it matches the selection criteria used for the study of Higgs boson production in association with dijets, *and* it avoids the focus on jets of very large transverse momenta, which is a result of studying large m_{jj} for solely central jets. We will compare to data the fixed-order predictions for $Wjj@NLO$ obtained using Sherpa [83] and those of HEJ obtained using the improvements presented in this thesis and in [9] wherein further details can be found.

In particular we compare the predictions for the inclusive and exclusive jet counts, the transverse momenta of the leading and sub-leading jet and of the W-boson, and the azimuthal angle between the two leading jets. $\mu_f = \mu_r = H_T/2$ is the central chosen for all predictions, and the scale variation band is the envelope of an independent variation of both μ_f and μ_r by up to a factor up 2, except configurations with a ratio between them larger than 2 (or smaller than 1/2). All of this is by the convention, not to avoid artificially improving the correlation between prediction and data.

We discussed the impact on observables of including resummation of the next-to-leading logarithmic processes in Section 5.1, and illustrated it in Figs. 5.1–5.6.

Prior to these improvements, predictions based solely on the leading-logarithmic description as in [79] combined with matching to high-multiplicity Born-level matrix elements fails systematically in the regions of large (> 100GeV) transverse momenta of the jets. This is expected, as it is outside the multi-Regge kinematic conditions that the leading logarithmic approximation is based upon. This break down in prediction capability displays the shortcoming of matching the non-resummable part of the cross-section with a simple addition of Born-level events of increasing multiplicity. That is that the born level predictions should be considered inclusive in jet multiplicity, so simply adding the contributions leads to overestimated cross-sections. We don't solve this by the inclusion of sub-leading channels; however, we reduce our dependence on Born-level matching from 60% to 35%, which reduces the impact of this overestimation.

In the paper [9], we can also see the impact of the developed NLO matching which will be combined into the following ATLAS data comparisons.

Figs. 5.7a-5.7b show the predictions for the inclusive and exclusive jet rates respectively to the data from ATLAS. NLO matching of the inclusive two-jet rate, as described in [9], reduces the scale dependence relative to predictions made with `HEJ` 1 reported in [8]. For the predictions made with the NLL resummation and 2-jet inclusive NLO matching, the central predictions for both inclusive and exclusive jet rates are within the 1-σ band of the ATLAS data.

The next two subplots, Figs. 5.7c-5.7d show the differential cross-section for the

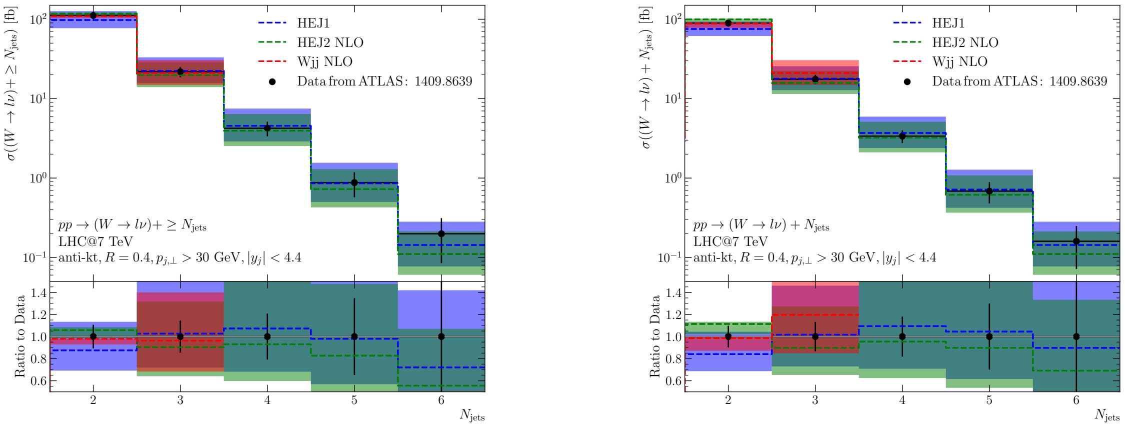

(a) Inclusive jet rates.

(b) Exclusive jet rates.

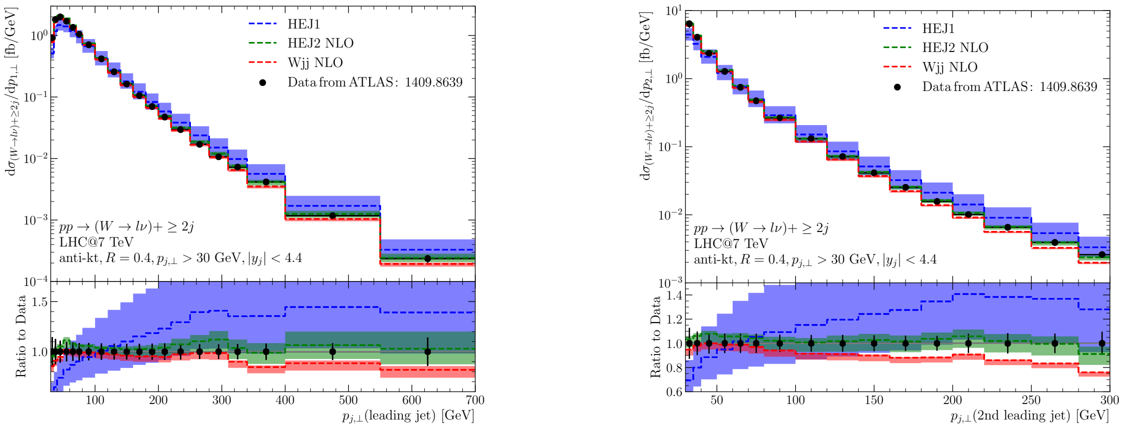

(c) Differential cross-section for the transverse momentum of the leading jet.

(d) Differential cross-section for the transverse momentum of the second leading jet.

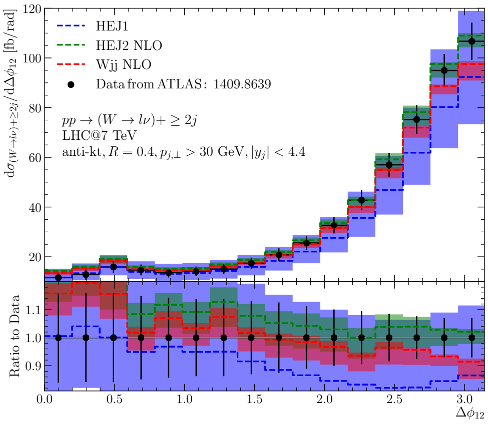

(e) Differential cross-section for the azimuthal angle between the two leading jets.

Figure 5.7: *Predictions for $pp \to (W \to l\nu)+ \geq 2j$ for LHC@7TeV, compared to ATLAS data from [8]. The original HEJ1 predictions are shown in blue, the pure NLO predictions are shown in red and the new HEJ2 predictions incorporating the methods of Chapter 4 and the NLO matching from [9] are shown in green.*

transverse momentum of the leading jet, and the second leading jet respectively. We observe that including subleading processes in the resummation significantly improves the description of scatterings at large transverse momenta. We see significant improvement over the predictions made by `HEJ` 1 in `HEJ` 2, with all previously identified discrepancies in these distributions being resolved. In fact, the central predictions of `HEJ` 2 are closer to the data than pure WjjNLO, albeit with larger scale variation.

The final subplot, Fig. 5.7e, shows the differential distribution for the azimuthal angle between the two hardest jets, ϕ_{12}. We again observe a significant reduction in scale variation and predictions that are much closer to the central value of the data from ATLAS. Overall, the prediction here is of similar accuracy to pure NLO.

Fig. 5.8 depicts the `HEJ` 1 and `HEJ` 2 predictions along with NLO predictions and ATLAS data for 8 TeV collisions. We see similar improvements across the board between `HEJ` 1 and `HEJ` 2 predictions as with the 7 TeV comparisons. To pull out specifics, The inclusive jet rates obtained with `HEJ` 2 show very good agreement with data across all matched multiplicities 2 to 6 inclusive. Similarly, we also see that predictions are excellent matches to data for the transverse momenta of the first and second hardest jet, and for the W-boson.

Clearly, the predictions show marked improvement between `HEJ` 1 and `HEJ` 2 for a wide range of distributions, fixing shortcomings of the previous approach to predictions based on Born-level matching and leading-logarithmic resummation. We have dramatically reduced scale variation to be more in line with pure WjjNLO predictions while substantially enhancing the description of distributions in subleading regions of phase-space such as large transverse momenta.

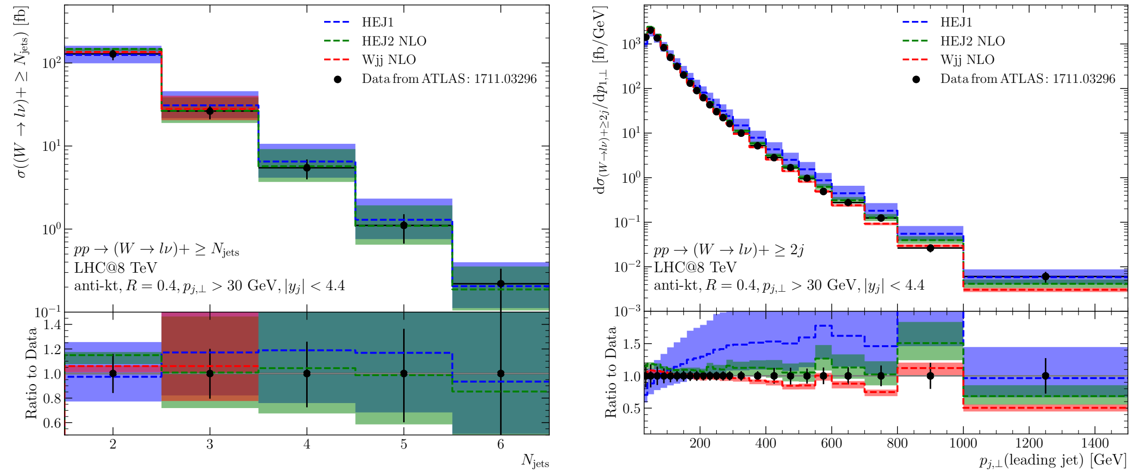

(a) Inclusive jet rates.

(b) Differential cross-section for the transverse momentum of the leading jet.

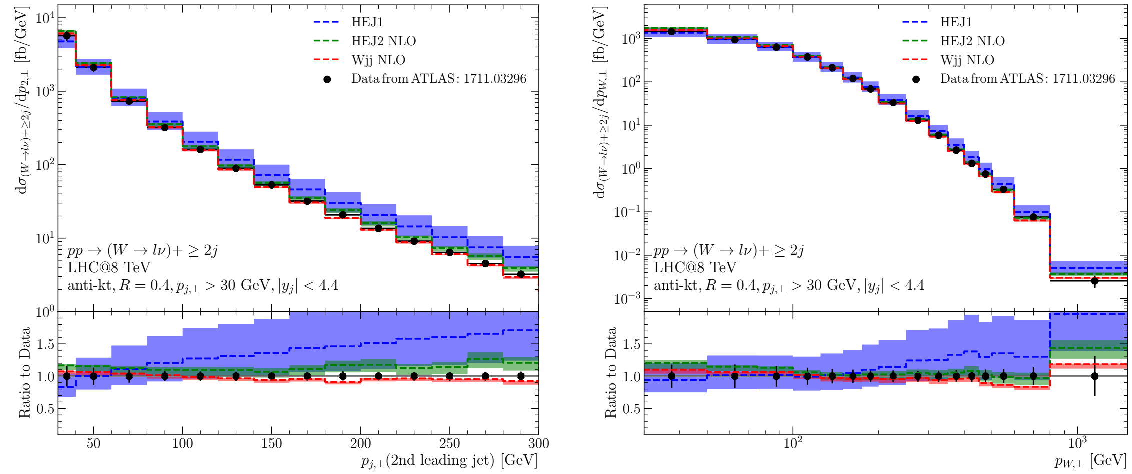

(c) Differential cross-section for the transverse momentum of the second leading jet.

(d) Differential cross-section for the transverse momentum of the boson.

Figure 5.8: *Predictions for $pp \to (W \to l\nu)+ \geq 2j$ for LHC@8TeV, compared to ATLAS data from [10]. The original HEJ1 predictions are shown in blue, the pure NLO predictions are shown in red and the new HEJ2 predictions incorporating the methods of Chapter 4 and the NLO matching from [9] are shown in green.*

CHAPTER

SIX

CONCLUSIONS

In Chapter 1, we stated that a key motivation for building the *Large Hadron Collider* was to directly observe all fundamental particles predicted by the highly successful *Standard Model* of particle physics. Back in 2012, the LHC achieved this aim, with the observation of a ‘Standard Model-like’ Higgs boson [84, 85], which was the start of a new age in particle physics. No longer was the focus on experiment to discover remaining elements of the theory, but rather to find places which the results from colliding these hadrons together deviates from our theoretical understanding enough to provide a glimpse into where the theoretical understanding may be lacking.

To this end, the game has changed to one of high precision. This applies to both experimental and theoretical communities. Most notably, there is a large body of work being performed to work out whether the Higgs boson which was observed at the LHC was indeed as the Standard Model predicts, or whether it more closely resembles that predicted by other models, such as the Higgs doublet model. Regardless this requires more data from experimental observations, which is why it is prudent for the continual (planned) upgrades to the LHC which can provide more precise measurements to be compared to.

As experimental results become more precise, theoretical predictions must improve in parallel. We explained in section 1.3 how one goes from a basic Lagrangian through to a basic prediction using fixed-order QCD, and how one can naively improve upon this easily[1] with one traditional method which is used; however, we also followed this with a set of sound reasoning as to why this is potentially not enough for a full description in Section 1.4. Specifically this was a discussion of how large logarithms can destroy a good fixed-order description in certain areas of phase-space.

Using parton shower resummation on top of fixed-order predictions is a common approach, but it has been shown to be inadequate in certain regions. Specifically, these methods tend to underestimate the number of hard jets which are produced in the resulting final state particles from very high energy collisions.

The HEJ formalism described in Chapter 2 resums the high-energy logarithms that appear in regions with large rapidity separations. These logs spoil fixed-order convergence and are not cured by standard parton showers; resumming them enables accurate predictions in the high-energy limit.

We discussed in Section 2.3.1 various high profile cases in which this approach has been necessary already. For example, if one attempts to investigate the VBF Higgs production channel, it is necessary to produce an accurate prediction for all the Higgs production channels which contribute. Even in the highly exclusive areas of phase-space in which the VBF channel is the dominant contribution such as with a large jet veto in a central rapidity span with multiple jet production in association with a Higgs boson, the gluon fusion Higgs production background is still large, and understanding this QCD process is important. The high energy logarithms which are summed and included by the `HEJ` calculation lead to a better understanding of the background, and thus a more precise overall theoretical prediction for comparison to experimental data to investigate the properties of the Higgs boson's interaction with vector bosons.

---

[1] Easily understood at least, as an increase in the number of terms considered in the power expansion of α_S, not necessarily easily performed

In the same section, we further discussed how `HEJ` allows for the integration of these logarithms across the full phase-space available within each channel since there are minimal approximations made when exposing the high energy factorisation, due to the use of the spinor-helicity formalism. We built a picture of how a basic `HEJ` amplitude is constructed in Section 2.3.2 and then in Section 2.3.4, we discussed how `HEJ` has traditionally built upon fixed-order calculations through matching which allows for a correct normalisation of the cross-section prediction for regions in which the approximations made within `HEJ` are expected to be poor (that is, away from the high energy limit discussed in Section 2.2.1).

In Section 2.4 we included the final piece of background physics which was needed before the new material within this thesis could be considered: the discussion of how W+Jets is included with `HEJ`. The inclusion of this last piece of the puzzle allowed us to move onto the implementation of this background knowledge.

This began with a discussion of what Monte Carlo integration is within Chapter 3. This essentially covered the methods used and the implementation of the physics contained within this thesis. We noted that since the work within this thesis began there has been a dramatic shift in how the calculations are performed within `HEJ`, and the implications of this shift lie largely within the method of matching. This change was discussed at length in Section 3.2.1.

At this point we were able to move on to the improvements which are added to the basic `HEJ` prediction for W+Jets contained within this thesis. Namely, in Section 4 we discussed the inclusion of subleading channels within the `HEJ` formalism, such as those presented in pure jet production in the past. We then discussed the real contributions required for `HEJ` to achieve formal NLL accuracy. The derivation of all these pieces was included as well as various methods of validation which these newly calculated pieces were put through in Section 4.6.4. Next we showed the impact due to the inclusion of these channels on the reliance on fixed-order input within the `HEJ` prediction, which was shown to be greatly reduced in Section 5.1.

Finally, after all of this we presented how the predictions of `HEJ` have improved over the jump between `HEJ1` and `HEJ2` by comparison with ATLAS data for production of W-bosons in association with at least two jets for 7TeV and 8TeV collisions as shown in the plots in Section 5.

It was found that the inclusion of these subleading channels along with the matching to $Wjj@NLO$ has improved predictions when compared to the previous approach which included only born level matching and the leading-logarithmic resummation. This result aligns with the findings in Section 4.1, where we saw that all-order resummation now covers a significantly larger fraction of phase-space.

In this thesis we have attempted to describe what is a somewhat novel method of improving theoretical predictions within the high energy limit by the inclusion of subleading logarithms. The improvements contained within this thesis improve the precision of the predictions made for multiple jet production in association with a W-boson. We hope that, combined with ongoing improvements in the `HEJ` formalism, this work will provide an additional tool for theorists to better constrain viable BSM physics while deepening our understanding of the Standard Model.

BIBLIOGRAPHY

[1] J. H. et al., *New cteq global analysis of quantum chromodynamics with high-precision data from the lhc*, 2019.

[2] M. Hoppe, *Recent developments in monte-carlo event generators*, p. 312, 12, 2024, DOI.

[3] J. R. Andersen and J. M. Smillie, *Constructing All-Order Corrections to Multi-Jet Rates*, *JHEP* **1001** (2010) 039, [`0908.2786`].

[4] D. Collaboration, *Studies of w boson plus jets production in $p\bar{p}$ collisions at $\sqrt{s}$=1.96 tev*, `arXiv:1302.6508`.

[5] M. Campanelli, *Forward jets and large rapidity gaps*, 2015.

[6] A. Collaboration, *Measurements of the w production cross sections in association with jets with the atlas detector*, `arXiv:1409.8639`.

[7] J. R. Andersen, T. Hapola, A. Maier and J. M. Smillie, *Higgs Boson Plus Dijets: Higher Order Corrections*, *JHEP* **09** (2017) 065, [`1706.01002`].

[8] ATLAS collaboration, G. Aad et al., *Measurements of the W production cross sections in association with jets with the ATLAS detector*, *Eur. Phys. J.* **C75** (2015) 82, [`1409.8639`].

[9] J. R. Andersen, J. A. Black, H. M. Brooks, E. P. Byrne, A. Maier and J. M. Smillie, *Combined subleading high-energy logarithms and NLO accuracy for w production in association with multiple jets*, *Journal of High Energy Physics* **2021** (2021) , [`2012.10310`].

[10] ATLAS collaboration, M. Aaboud et al., *Measurement of differential cross sections and W^+/W^- cross-section ratios for W boson production in association with jets at $\sqrt{s} = 8$ TeV with the ATLAS detector*, *JHEP* **05** (2018) 077, [`1711.03296`].

[11] M. Peskin, *An Introduction To Quantum Field Theory.* Westview Press, New York, 1995.

[12] Y. Nagashima, *Elementary Particle Physics.* Wiley-VCH Verlag GmbH & Co. KGaA, feb, 2013, 10.1002/9783527648887.

[13] T. A. et al., *Tenth-order QED contribution to the electron g-2 and an improved value of the fine structure constant*, *Physical Review Letters* **109** (sep, 2012) .

[14] N. J. et al., *Seven-year wilkinson microwave anisotropy probe (wmap) observations: Sky maps, systematic errors, and basic results*, *The Astrophysical Journal Supplement Series* **192** (jan, 2011) 14.

[15] D. C. et al., *A direct empirical proof of the existence of dark matter*, *The Astrophysical Journal* **648** (aug, 2006) L109–L113.

[16] J. J. Thomson, *Xl. cathode rays*, *The London, Edinburgh, and Dublin Philosophical Magazine and Journal of Science* **44** (oct, 1897) 293–316.

[17] S. C. et al., *Observation of a new boson at a mass of 125 GeV with the CMS experiment at the LHC*, *Physics Letters B* **716** (sep, 2012) 30–61.

[18] G. A. et al., *Observation of a new particle in the search for the standard model higgs boson with the ATLAS detector at the LHC*, *Physics Letters B* **716** (sep, 2012) 1–29.

[19] P. W. Higgs, *Broken symmetries and the masses of gauge bosons*, *Physical Review Letters* **13** (oct, 1964) 508–509.

[20] F. Englert and R. Brout, *Broken symmetry and the mass of gauge vector mesons*, *Physical Review Letters* **13** (aug, 1964) 321–323.

[21] C. D. Anderson, *The apparent existence of easily deflectable positives*, *Science* **76** (sep, 1932) 238–239.

[22] P. A. M. Dirac, *The quantum theory of the electron*, *Proceedings of the Royal Society of London. Series A, Containing Papers of a Mathematical and Physical Character* **117** (feb, 1928) 610–624.

[23] M. C. et al., *On the disintegration of negative mesons*, *Physical Review* **71** (feb, 1947) 209–210.

[24] F. R. et al., *The neutrino*, *Nature* **178** (sep, 1956) 446–449.

[25] L. M. Brown, *The idea of the neutrino*, *Physics Today* **31** (sep, 1978) 23–28.

[26] L. M. L. et al., *Observation of high-energy neutrino reactions and the existence of two kinds of neutrinos*, *Physical Review Letters* **9** (jul, 1962) 36–44.

[27] J. I. F. et al., *High-energy inelastic e-p scattering at 6° and 10°*, *Physical Review Letters* **23** (oct, 1969) 930–934.

[28] M. Gell-Mann, *A schematic model of baryons and mesons*, *Physics Letters* **8** (feb, 1964) 214–215.

[29] B. R. et al., *Experimental observation of a heavy particle j*, *Physical Review Letters* **33** (dec, 1974) 1404–1406.

[30] B. Bjørken and S. Glashow, *Elementary particles and SU(4)*, *Physics Letters* **11** (aug, 1964) 255–257.

[31] M. L. P. et al., *Evidence for anomalous lepton production in e+ e- annihilation*, *Physical Review Letters* **35** (dec, 1975) 1489–1492.

[32] L. M. L. et al., *Observation of a dimuon resonance at 9.5 GeV in 400-GeV proton-nucleus collisions*, *Physical Review Letters* **39** (aug, 1977) 252–255.

[33] M. Kobayashi and T. Maskawa, *CP-violation in the renormalizable theory of weak interaction*, *Progress of Theoretical Physics* **49** (feb, 1973) 652–657.

[34] D. P. Barber, *Discovery of three-jet events and a test of quantum chromodynamics at PETRA*, *Physical Review Letters* **43** (sep, 1979) 830–833.

[35] C. R. et al., *Experimental observation of lepton pairs of invariant mass around 95 GeV/c2 at the CERN SPS collider*, *Physics Letters B* **126** (jul, 1983) 398–410.

[36] J. F. et al., *Observation of top quark production in p¯ p collisions with the collider detector at fermilab*, *Physical Review Letters* **74** (apr, 1995) 2626–2631.

[37] K. K. et al., *Observation of tau neutrino interactions*, *Physics Letters B* **504** (apr, 2001) 218–224.

[38] G. Zweig, *An su(3) model for strong interaction symmetry and its breaking. version 2*, .

[39] O. W. Greenberg, *Spin and unitary-spin independence in a paraquark model of baryons and mesons*, *Physical Review Letters* **13** (nov, 1964) 598–602.

[40] H. D. Politzer, *Reliable perturbative results for strong interactions?*, *Physical Review Letters* **30** (jun, 1973) 1346–1349.

[41] D. J. Gross and F. Wilczek, *Ultraviolet behavior of non-abelian gauge theories*, *Physical Review Letters* **30** (jun, 1973) 1343–1346.

[42] M. D. Schwartz, *Quantum Field Theory and the Standard Model.* 05, 2021.

[43] J. Campbell, J. Huston and F. Krauss, *The Black Book of Quantum Chromodynamics.* 05, 2018.

[44] R. D. Peccei and H. R. Quinn, *Constraints imposed by cp conservation in the presence of instantons*, *Physical Review D* **16** (1977) 1791–1797.

[45] P. Baikov, K. Chetyrkin and J. Kühn, *Five-loop running of the QCD coupling constant*, *Physical Review Letters* **118** (feb, 2017) .

[46] F. Herzog, B. Ruijl, T. Ueda, J. A. M. Vermaseren and A. Vogt, *The five-loop beta function of yang-mills theory with fermions*, *Journal of High Energy Physics* **2017** (feb, 2017) .

[47] T. Kinoshita, *Mass singularities of feynman amplitudes*, *Journal of Mathematical Physics* **3** (jul, 1962) 650–677.

[48] T. D. Lee and M. Nauenberg, *Degenerate systems and mass singularities*, *Phys. Rev.* **133** (Mar, 1964) B1549–B1562.

[49] S. Catani and M. Seymour, *A general algorithm for calculating jet cross sections in NLO QCD*, *Nuclear Physics B* **485** (1996) 291–419.

[50] F. P. R. Boughezal, K. Melnikov, *A subtraction scheme for next-to-next-to-leading order computations*, *Phys. Rev. D 85* **2012** (2007) 035.

[51] J. C. Collins, *Foundations of Perturbative QCD.* Cambridge University Press, 1 ed., 1998.

[52] A. Martin, W. Stirling, R. Thorne and G. Watt, *Parton distributions for the LHC*, *Journal of High Energy Physics* **2009** (2009) 63.

[53] A. Buckley, J. Ferrando, S. Lloyd, K. Nordström, B. Page, M. Rüfenacht et al., *LHAPDF6: parton density access in the LHC precision era*, *Eur. Phys. J. C* **75** (2015) 132, [`1412.7420`].

[54] ATLAS collaboration, M. Aaboud et al., *Measurement of the cross-section for electroweak production of dijets in association with a Z boson in pp collisions at* $\sqrt{s}$ *= 13 TeV with the ATLAS detector*, *Phys. Lett.* **B775** (2017) 206–228, [`1709.10264`].

[55] G. P. S. et al., *The anti-kt jet clustering algorithm*, `arXiv:0802.1189`.

[56] G. P. Salam, *Towards jetography*, `arXiv:0906.1833`.

[57] D0 collaboration, V. M. Abazov et al., *Studies of W boson plus jets production in* $p\bar{p}$ *collisions at* $\sqrt{s} = 1.96$ *TeV*, *Phys.Rev.* **D88** (2013) 092001, [`1302.6508`].

[58] ATLAS Collaboration collaboration, G. Aad et al., *Measurement of dijet production with a veto on additional central jet activity in pp collisions at* $\sqrt{s} = 7$ *TeV using the ATLAS detector*, *JHEP* **1109** (2011) 053, [`1107.1641`].

[59] ATLAS collaboration, G. Aad et al., *Measurements of jet vetoes and azimuthal decorrelations in dijet events produced in pp collisions at* $\sqrt{s} = 7\,\text{TeV}$ *using the ATLAS detector*, *Eur. Phys. J.* **C74** (2014) 3117, [`1407.5756`].

[60] J. R. Andersen and J. M. Smillie, *The Factorisation of the t-channel Pole in Quark-Gluon Scattering*, *Phys.Rev.* **D81** (2010) 114021, [`0910.5113`].

[61] V. S. Fadin, E. Kuraev and L. Lipatov, *On the Pomeranchuk Singularity in Asymptotically Free Theories*, *Phys. Lett. B* **60** (1975) 50–52.

[62] E. A. Kuraev, L. N. Lipatov and V. S. Fadin, *Multi - Reggeon processes in the Yang-Mills theory*, *Sov. Phys. JETP* **44** (1976) 443–450.

[63] E. A. Kuraev, L. N. Lipatov and V. S. Fadin, *The Pomeranchuk singularity in nonabelian gauge theories*, *Sov. Phys. JETP* **45** (1977) 199–204.

[64] I. I. Balitsky and L. N. Lipatov, *The Pomeranchuk singularity in quantum chromodynamics*, *Sov. J. Nucl. Phys.* **28** (1978) 822–829.

[65] P. D. B. Collins, *An Introduction to Regge Theory and High Energy Physics*. Cambridge University Press, 1977.

[66] J. R. Andersen and J. M. Smillie, *Multiple Jets at the LHC with High Energy Jets*, *JHEP* **1106** (2011) 010, [`1101.5394`].

[67] T. C. Collaboration, *Cms physics technical design report, volume II: Physics performance*, *Journal of Physics G: Nuclear and Particle Physics* **34** (apr, 2007) 995–1579.

[68] T. A. Collaboration, *The ATLAS experiment at the CERN large hadron collider*, *Journal of Instrumentation* **3** (aug, 2008) S08003–S08003.

[69] V. Del Duca, W. Kilgore, C. Oleari, C. Schmidt and D. Zeppenfeld, *Gluon fusion contributions to H + 2 jet production*, *Nucl.Phys.* **B616** (2001) 367–399, [`hep-ph/0108030`].

[70] D. Collaboration and V. Abazov, *Measurement of the ratios of the z/g* + >= n jet production cross sections to the total inclusive z/g* cross section in ppbar collisions at sqrt(s) = 1.96 tev*, `arXiv:hep-ex/0608052`.

[71] L. N. Lipatov, *Reggeization of the vector meson and the vacuum singularity in non-abelian gauge theories*, *Sov. J. Nucl. Phys.* **23** (1976) 338.

[72] E. A. Kuraev, L. N. Lipatov and V. S. Fadin, *Multi-reggeon processes in the yang-mills theory*, *Sov. Phys. JETP* **45** (1977) 199.

[73] J. R. Andersen, T. Hapola, M. Heil, A. Maier and J. Smillie, *HEJ 2: High Energy Resummation for Hadron Colliders*, *Comput.Phys.Commun.* **245** (2019) , [`1902.08430`].

[74] J. Alwall, M. Herquet, F. Maltoni, O. Mattelaer and T. Stelzer, *Madgraph 5 : Going beyond*, `arXiv:1106.0522`.

[75] C. DeWitt-Morette, P. Cartier and A. Folacci, eds., *Functional Integration.* Springer US, 1997, 10.1007/978-1-4899-0319-8.

[76] D. E. Knuth, *The Art of Computer Programming, Volume 2: Seminumerical Algorithms.* Addison-Wesley, Reading, Massachusetts, 3rd ed., 1997.

[77] G. P. Lepage, *A new algorithm for adaptive multidimensional integration*, *Journal of Computational Physics* **27** (1978) 192–203.

[78] J. R. Andersen, J. D. Cockburn, M. Heil, A. Maier and J. M. Smillie, *Finite Quark-Mass Effects in Higgs Boson Production with Dijets at Large Energies*, *JHEP* **04** (2019) 127, [`1812.08072`].

[79] J. R. Andersen, T. Hapola and J. M. Smillie, *W Plus Multiple Jets at the LHC with High Energy Jets*, *JHEP* **1209** (2012) 047, [`1206.6763`].

[80] J. R. Andersen, J. J. Medley and J. M. Smillie, *Z/γ^* plus multiple hard jets in high energy collisions*, *JHEP* **05** (2016) 136, [`1603.05460`].

[81] J. R. Andersen, T. Hapola, M. Heil, A. Maier and J. M. Smillie, *Higgs-boson plus Dijets: Higher-Order Matching for High-Energy Predictions*, *JHEP* **08** (2018) 090, [`1805.04446`].

[82] J. Andersen, J. A. Black, H. Brooks, B. Ducloué, M. Heil, A. Maier et al., *Hej 2.1: High-energy resummation with vector bosons and next-to-leading logarithms*, *Computer Physics Communications* **278** (September, 2022) 108404, [`https://arxiv.org/abs/2110.15692`].

[83] Sherpa collaboration, E. Bothmann et al., *Event Generation with Sherpa 2.2*, *SciPost Phys.* **7** (2019) 034, [`1905.09127`].

[84] G. Aad and others (ATLAS Collaboration), *Observation of a new particle in the search for the standard model higgs boson with the atlas detector at the lhc*, *Physics Letters B* **716** (2012) 1–29.

[85] S. Chatrchyan and others (CMS Collaboration), *Observation of a new boson at a mass of 125 gev with the cms experiment at the lhc*, *Physics Letters B* **716** (2012) 30–61.

[86] M. Dohse, *Tikz-feynhand: Basic user guide*, 2018.

[87] M. T. et al., *Review of particle physics*, *Physical Review D* **98** (aug, 2018) .

[88] J. R. Andersen, T. Binoth, G. Heinrich and J. M. Smillie, *Loop induced interference effects in Higgs Boson plus two jet production at the LHC*, *JHEP* **0802** (2008) 057, [`0709.3513`].

[89] J. R. Andersen, V. Del Duca and C. D. White, *Higgs Boson Production in Association with Multiple Hard Jets*, *JHEP* **02** (2009) 015, [`0808.3696`].

[90] J. R. Andersen and C. D. White, *A New Framework for Multijet Predictions and its application to Higgs Boson production at the LHC*, *Phys. Rev.* **D78** (2008) 051501, [`0802.2858`].

[91] J. R. Andersen, K. Arnold and D. Zeppenfeld, *Azimuthal Angle Correlations for Higgs Boson plus Multi-Jet Events*, *JHEP* **1006** (2010) 091, [`1001.3822`].

[92] J. R. Andersen, L. Lönnblad and J. M. Smillie, *A Parton Shower for High Energy Jets*, *JHEP* **1107** (2011) 110, [`1104.1316`].

[93] F. Halzen and A. Martin, *Quarks and Leptons: An Introductory Course in Modern Particle Physics.* Wiley, 1984.

[94] M. Gell-Mann, *A schematic model of baryons and mesons*, *Physics Letters* **8** (1964) 214–215.

[95] G. Zweig, *An su(3) model for strong interaction symmetry and its breaking. version 1*, .

[96] G. Zweig, *An su(3) model for strong interaction symmetry and its breaking. version 2*, in *Developments in the Quark Theory of Hadrons, Volume 1* (D. Lichtenberg and S. P. Rosen, eds.), pp. 22–101. Hadronic Press, 1964.

[97] V. Del Duca, W. Kilgore, C. Oleari, C. Schmidt and D. Zeppenfeld, *Higgs + 2 jets via gluon fusion*, *Phys.Rev.Lett.* **87** (2001) 122001, [`hep-ph/0105129`].

[98] ATLAS collaboration, M. Aaboud et al., *Measurements of electroweak Wjj production and constraints on anomalous gauge couplings with the ATLAS detector*, *Eur. Phys. J.* **C77** (2017) 474, [`1703.04362`].

[99] ATLAS collaboration, M. Aaboud et al., *Measurements of the production cross section of a Z boson in association with jets in pp collisions at $\sqrt{s} = 13$ TeV with the ATLAS detector*, *Eur. Phys. J.* **C77** (2017) 361, [`1702.05725`].

[100] ATLAS Collaboration collaboration, G. Aad et al., *Measurements of Higgs boson production and couplings in diboson final states with the ATLAS detector at the LHC*, *Phys.Lett.* **B726** (2013) 88–119, [`1307.1427`].

[101] ATLAS Collaboration collaboration, G. Aad et al., *Evidence for the spin-0 nature of the Higgs boson using ATLAS data*, *Phys.Lett.* **B726** (2013) 120–144, [`1307.1432`].

[102] ATLAS Collaboration collaboration, G. Aad et al., *Measurement of the Higgs boson mass from the $H \to \gamma\gamma$ and $H \to ZZ^* \to 4\ell$ channels with the ATLAS detector using 25 fb^{-1} of pp collision data*, *Phys.Rev.* **D90** (2014) 052004, [`1406.3827`].

[103] ATLAS collaboration, G. Aad et al., *Measurement of the electroweak production of dijets in association with a Z-boson and distributions sensitive*

to vector boson fusion in proton-proton collisions at $\sqrt{s} = 8$ TeV using the ATLAS detector, *JHEP* **04** (2014) 031, [`1401.7610`].

[104] ATLAS Collaboration collaboration, G. Aad et al., *Measurement of Higgs boson production in the diphoton decay channel in pp collisions at center-of-mass energies of 7 and 8 TeV with the ATLAS detector*, `1408.7084`.

[105] ATLAS Collaboration collaboration, G. Aad et al., *Measurements of Higgs boson production and couplings in the four-lepton channel in pp collisions at center-of-mass energies of 7 and 8 TeV with the ATLAS detector*, `1408.5191`.

[106] ATLAS Collaboration collaboration, G. Aad et al., *Measurements of fiducial and differential cross sections for Higgs boson production in the diphoton decay channel at $\sqrt{s} = 8$ TeV with ATLAS*, `1407.4222`.

[107] ATLAS Collaboration collaboration, G. Aad et al., *Fiducial and differential cross sections of Higgs boson production measured in the four-lepton decay channel in pp collisions at $\sqrt{s}$=8 TeV with the ATLAS detector*, `1408.3226`.

[108] ATLAS collaboration, G. Aad et al., *Measurement of four-jet differential cross sections in $\sqrt{s} = 8$ TeV proton-proton collisions using the ATLAS detector*, *JHEP* **12** (2015) 105, [`1509.07335`].

[109] J. Alwall, R. Frederix, S. Frixione, V. Hirschi, F. Maltoni, O. Mattelaer et al., *The automated computation of tree-level and next-to-leading order differential cross sections, and their matching to parton shower simulations*, *JHEP* **07** (2014) 079, [`1405.0301`].

[110] NNPDF collaboration, R. D. Ball et al., *Parton distributions from high-precision collider data*, *Eur. Phys. J. C* **77** (2017) 663, [`1706.00428`].

[111] A. Banfi, P. F. Monni, G. P. Salam and G. Zanderighi, *Higgs and Z-boson production with a jet veto*, *Phys.Rev.Lett.* **109** (2012) 202001, [`1206.4998`].

[112] A. Banfi, G. P. Salam and G. Zanderighi, *NLL+NNLO predictions for jet-veto efficiencies in Higgs-boson and Drell-Yan production*, *JHEP* **1206** (2012) 159, [`1203.5773`].

[113] C. F. Berger, C. Marcantonini, I. W. Stewart, F. J. Tackmann and W. J. Waalewijn, *Higgs Production with a Central Jet Veto at NNLL+NNLO*, *JHEP* **1104** (2011) 092, [`1012.4480`].

[114] A. Bogdan, V. Del Duca, V. S. Fadin and E. N. Glover, *The Quark Regge trajectory at two loops*, *JHEP* **0203** (2002) 032, [`hep-ph/0201240`].

[115] A. V. Bogdan and V. S. Fadin, *A proof of the reggeized form of amplitudes with quark exchanges*, *Nucl. Phys.* **B740** (2006) 36–57, [`hep-ph/0601117`].

[116] A. Bredenstein, K. Hagiwara and B. Jager, *Mixed QCD-electroweak contributions to Higgs-plus-dijet production at the LHC*, *Phys.Rev.* **D77** (2008) 073004, [`0801.4231`].

[117] R. Brower, C. E. DeTar and J. Weis, *Regge Theory for Multiparticle Amplitudes*, *Phys.Rept.* **14** (1974) 257.

[118] J. M. Campbell, R. K. Ellis and G. Zanderighi, *Next-to-Leading order Higgs + 2 jet production via gluon fusion*, *JHEP* **0610** (2006) 028, [`hep-ph/0608194`].

[119] J. M. Campbell, R. K. Ellis and C. Williams, *Hadronic production of a Higgs boson and two jets at next-to-leading order*, *Phys.Rev.* **D81** (2010) 074023, [`1001.4495`].

[120] T. Kinoshita, T. D. Lee and M. Nauenberg, *Infrared divergences in quantum electrodynamics*, *Phys. Rev.* **133** (1964) B1549–B1562.

[121] S. Catani, F. Krauss, R. Kuhn and B. Webber, *QCD matrix elements + parton showers*, *JHEP* **0111** (2001) 063, [`hep-ph/0109231`].

[122] CMS COLLABORATION collaboration, S. Chatrchyan et al., *Measurement of the inclusive production cross sections for forward jets and for dijet events with one forward and one central jet in pp collisions at $\sqrt{s} = 7$ TeV*, *JHEP* **1206** (2012) 036, [`1202.0704`].

[123] CMS COLLABORATION collaboration, S. Chatrchyan et al., *Study of the Mass and Spin-Parity of the Higgs Boson Candidate Via Its Decays to Z Boson Pairs*, *Phys.Rev.Lett.* **110** (2013) 081803, [`1212.6639`].

[124] CMS collaboration, S. Chatrchyan et al., *Observation of a new boson at a mass of 125 GeV with the CMS experiment at the LHC*, *Phys.Lett.* **B716** (2012) 30–61, [`1207.7235`].

[125] CMS COLLABORATION collaboration, S. Chatrchyan et al., *Measurement of the properties of a Higgs boson in the four-lepton final state*, *Phys.Rev.* **D89** (2014) 092007, [`1312.5353`].

[126] V. Del Duca, *Parke-Taylor amplitudes in the multi - Regge kinematics*, *Phys. Rev.* **D48** (1993) 5133–5139, [`hep-ph/9304259`].

[127] V. Del Duca, *An introduction to the perturbative QCD pomeron and to jet physics at large rapidities*, `hep-ph/9503226`.

[128] V. Del Duca, *Equivalence of the Parke-Taylor and the Fadin-Kuraev-Lipatov amplitudes in the high-energy limit*, *Phys.Rev.* **D52** (1995) 1527–1534, [`hep-ph/9503340`].

[129] V. Del Duca, A. Frizzo and F. Maltoni, *Factorization of tree QCD amplitudes in the high-energy limit and in the collinear limit*, *Nucl.Phys.* **B568** (2000) 211–262, [`hep-ph/9909464`].

[130] V. Del Duca and E. Glover, *The High-energy limit of QCD at two loops*, *JHEP* **10** (2001) 035, [`hep-ph/0109028`].

[131] V. Del Duca, W. Kilgore, C. Oleari, C. Schmidt and D. Zeppenfeld, *Kinematical limits on Higgs boson production via gluon fusion in association with jets*, *Phys.Rev.* **D67** (2003) 073003, [`hep-ph/0301013`].

[132] Y. L. Dokshitzer, V. A. Khoze and T. Sjostrand, *Rapidity gaps in Higgs production*, *Phys.Lett.* **B274** (1992) 116–121.

[133] M. J. Dolan, P. Harris, M. Jankowiak and M. Spannowsky, *Constraining CP-violating Higgs Sectors at the LHC using gluon fusion*, *Phys. Rev.* **D90** (2014) 073008, [`1406.3322`].

[134] V. S. Fadin, M. G. Kozlov and A. V. Reznichenko, *Radiative corrections to QCD amplitudes in quasi-multi-Regge kinematics*, *Phys. Atom. Nucl.* **67** (2004) 359–375, [`hep-ph/0302224`].

[135] V. S. Fadin, *The gluon Reggeization in perturbative QCD at NLO*, `hep-ph/0511121`.

[136] V. S. Fadin, R. Fiore, M. G. Kozlov and A. V. Reznichenko, *Proof of the multi-Regge form of QCD amplitudes with gluon exchanges in the NLA*, *Phys. Lett.* **B639** (2006) 74–81, [`hep-ph/0602006`].

[137] S. Gangal and F. J. Tackmann, *Next-to-leading-order uncertainties in Higgs+2 jets from gluon fusion*, *Phys.Rev.* **D87** (2013) 093008, [`1302.5437`].

[138] J. F. Gunion and Z. Kunszt, *Improved Analytic Techniques for Tree Graph Calculations and the G g q anti-q Lepton anti-Lepton Subprocess*, *Phys. Lett.* **161B** (1985) 333.

[139] LHC Higgs Cross Section Working Group collaboration, S. Heinemeyer et al., *Handbook of LHC Higgs Cross Sections: 3. Higgs Properties*, `1307.1347`.

[140] R. P. Kauffman, S. V. Desai and D. Risal, *Production of a Higgs boson plus two jets in hadronic collisions*, *Phys.Rev.* **D55** (1997) 4005–4015, [`hep-ph/9610541`].

[141] CMS Collaboration collaboration, V. Khachatryan et al., *Constraints on the Higgs boson width from off-shell production and decay to Z-boson pairs*, *Phys.Lett.* **B736** (2014) 64, [`1405.3455`].

[142] CMS Collaboration collaboration, V. Khachatryan et al., *Observation of the diphoton decay of the Higgs boson and measurement of its properties*, `1407.0558`.

[143] G. Klamke and D. Zeppenfeld, *Higgs plus two jet production via gluon fusion as a signal at the CERN LHC*, *JHEP* **0704** (2007) 052, [`hep-ph/0703202`].

[144] L. Lonnblad, *ARIADNE version 4: A Program for simulation of QCD cascades implementing the color dipole model*, *Comput.Phys.Commun.* **71** (1992) 15–31.

[145] S. J. Parke and T. Taylor, *An Amplitude for n Gluon Scattering*, *Phys.Rev.Lett.* **56** (1986) 2459.

[146] I. W. Stewart, F. J. Tackmann, J. R. Walsh and S. Zuberi, *Jet p_T Resummation in Higgs Production at $NNLL' + NNLO$*, `1307.1808`.

[147] F. J. Tackmann, J. R. Walsh and S. Zuberi, *Resummation Properties of Jet Vetoes at the LHC*, *Phys.Rev.* **D86** (2012) 053011, [`1206.4312`].

[148] R. K. Ellis, W. J. Stirling and B. R. Webber, *QCD and Collider Physics.* 10, 1996.

[149] P. D. Group, *Review of Particle Physics*, *Progress of Theoretical and Experimental Physics* **2022** (2022) 083C01.